Imperial College London
Department of Mechanical Engineering
Exhibition Road, London, SW7 2AZ

Applications of a Numerical Method in Study of Combustion Instabilities

Yu Gong

Submitted in part fulfilment of the requirements for the degree of
Doctor of Philosophy in Mechanical Engineering of Imperial College London
and the Diploma of Imperial College London, May 2022

Declaration

Copyright declaration

Declaration of originality

I certify that the work presented here is original, except as acknowledged, and has not been submitted, either in whole or part, for a degree at any other university than Imperial College London. This thesis is produced under the supervision of Professor Jones. Contents taken from other sources are cited as such.

Yu Gong

May 2022

For Ying and Shihong.

Acknowledgements

I would like to express my gratitude to my supervisor Professor Bill Jones, who has been extremely supportive and encouraging throughout my entire research without whom I would never have started this journey. I am grateful to my co-supervisor Dr. Fred Marquis for his professional advice and positive spirit and humour which are truly invaluable to me. I consider myself very lucky to have worked under their supervision and be part of the big thermal fluid community. Special thanks to Dr. Daniel Fredrich for his invaluable support and patience, who has kindly shared many thoughts and offered much help when I just need them. Sincere thanks to Department of Mechanical Engineering at Imperial College and the CSC scholarship for the project funding and UKCTRF for providing computational time on the ARCHER, ARHCER2, Cirrus and Isambard UK National Supercomputing Service.

Moreover, I wish to thank my friends and colleagues Hanxun, Zhengyuan, Ganlin, Min, Xue, Dan, Steven, Dongwon, Simon and everyone else from the offices 675 for all the laughs and good memories. I am very grateful for their friendship and accompany, making my past few years at Imperial so memorable. Thanks also to my big sister Dudu and her family for making my life in London blessedly warm.

Last but not least, I am most grateful to my parents who have provided me with unconditional love and supports throughout my life. I dedicate the thesis to my dad, in loving memory, who encouraged me to start this adventure but never saw I would reach this far.

Related Work

Journal papers

Gong, Y., Jones, W. P. & Marquis, A. J. (2021b), 'Study of a Premixed Turbulent Counter-Flow Flame with a Large Eddy Simulation Method', *Flow Turbulence Combust* pp. 1–20.

Gong, Y., Jones, W. P. & Marquis, A. J. (2021a), 'Numerical analysis of indirect noise generated by compositional inhomogeneities using large eddy simulation', *AIP Advances* **11**, 115103.

Gong, Y., Fredrich, D., Jones, W. P. & Marquis, A. J. (2022), 'Interaction of helical vortices with Hydrogen-enriched swirling flames undergoing thermoacoustic instabilities', *Physics of Fluids*, **submitted**.

Conference paper

Gong Y, Fredrich D, Jones W P, Marquis A J. Large Eddy Simulation of Hydrogen Enriched Flames in a lean premixed swirling combustor. *12th International ERCOFTAC Symposium on Engineering Turbulence Modelling and Measurements*, 2021, online, virtual.

Gong Y, Fredrich D, Jones W P, Marquis A J, Boxx I. Thermoacoustic Instabilities of Hydrogen-enriched Partially Premixed Flames in a Swirl Combustor. *Turbomachinery Technical Conference and Exposition (GT2021)*. Publisher: The American Society of Mechanical Engineering.

Gong Y, Jones W P, Marquis A J. Study of an Opposed Jet Turbulent Flame Using the Sub-grid PDF Method. *9th European Combustion Meeting*, 2019, Lisbon. Publisher: Combustion Institute.

Gong Y, Jones W P, Marquis A J. Large Eddy Simulation of a Premixed Turbulent Counter-flow Flame. *12th International ERCOFTAC Symposium on Engineering Turbulence Modelling and Measurements*, 2018, Montpellier. Publisher: European Research Community on Flow, Turbulence and Combustion.

Abstract

This thesis explores the capabilities of an large Eddy Simulation (LES) method in study of flame dynamics with three test cases. The method, BOFFIN-LES, comprises a fully compressible formulation to account for acoustic wave propagation. A transported probability density function (*pdf*)/ Eulerian stochastic fields method is employed for turbulence-chemistry interaction, which has the merit that chemical source terms appear in a closed form so that no additional modelling for the chemical reaction is required. This approach is shown to be independent of flame burning regime and therefore highly applicable in the study of partially premixed flames with multiple regimes.

Combustion instabilities remain a central issue in designing and constructing successful lean combustion systems, which are driven and controlled by complex physical mechanisms including small-scale stochastic turbulent fluctuations and large-scale coherent structures. In order to address the capability of the employed LES method in study of combustion instabilities from different perspectives, three test cases are investigated: a highly strained turbulent flame with local-extinction and re-ignitions, noise generation in a resonator with a non-isentropic nozzle and finally a series of lab-scale swirling flames undergoing thermo-acoustic and hydrodynamic instabilities.

The findings of this work strongly suggest that the employed LES method is an effective and reliable tool to describe combustion dynamics related problems in elementary studies as well as complex flame configurations. The LES study has been shown to be capable of well predicting the unsteady flame local-extinction and re-ignition with a relatively small number of stochastic fields, and the influence of flame stoichiometry were also successfully reproduced. The methodology with proper acoustic boundary treatments predicts the direct and indirect noise generating process to a good level of accuracy in the context of low Mach number flows. In the application to swirling flames, the LES successfully reproduces thermo-acoustic and hydrodynamic instabilities, with the driving mechanism clearly identified. The LES well captures the iso-thermal flow dynamics and the flame topology under various operating conditions, with a good prediction of the thermo-acoustic frequencies in all the cases. The effect of Hydrogen enrichment on modifying the flame topology and changing the thermo-acoustic instability features are well predicted by the simulations. Different mode of precessing vortex cores (PVC) are detected, and their periodic excitement, evolution and effect on the flame stabilisation are discussed with great details. To conclude, the LES study provides many

useful insights into the investigated unsteady swirling flames, which involves complex interactions of unsteady combustion, acoustic fluctuations, flow dynamics and solid boundaries.

All the test cases are performed with virtually the same set of model parameters, which potentially eliminates the requirement of tuning or adjusting the model parameters according to a certain setup.

Contents

List of Tables

List of Figures

List of Symbols

Roman letters, upper case

C	binary progress variable
C_d	*sgs* mixing constant
C_{id}	the ratio of indirect noise to direct noise k
C_{P0}	pressure loss coefficient
C_s	Smagorinsky parameter
D	molecular diffusion coefficient
D_α	molecular diffusion coefficient of α
G	filter function width
Gy	axial flux of the azimuthal momentum
Gz	axial flux of the axial momentum
$J_{h,i}$	heat diffusion fluxes in i-direction
$J_{\alpha,i}$	diffusion fluxes of α in i-direction
K	strain rate
L	length

Le	Lewis number
N_s	number of species
N_{sc}	number of species plus one
N_{sf}	number of stochastic fields
P	pressure wave
P_α	*pdf* of ϕ_α
Pr	Prandtl number
P_{sgs}	joint *sgs-pdf* (or filter *pdf*)
P_{th}	thermal power
R	specific gas constant
Re	Reynolds number
Re_t	turbulent Reynolds number
R_n	burner nozzle equivalent radius
R_u	universal gas constant
S	swirl number
Sc	Schmidt number
Sc_α	Schmidt number of α
T	temperature
T_0	reference temperature
W	mean molar mass of the mixture

W_α molar mass of α

X_α mole fraction of α

Y_α mass fraction of α

Z mixture fraction

Roman letters, lower case

a_n n-th JANAF coefficients

c speed of sound

c_p heat capacity

d distance

$\mathrm{d}W_i^n$ Wiener process for the n-th stochastic field in i-direction

e isentropic expansion factor

e_{ij} strain tensor

f an instantaneous flow variable

f frequency

g gravitational acceleration

g_i gravitational acceleration in i-direction

h static enthalpy

h_α static enthalpy of α

k thermal conductivity

$\dot{m}$ mass flow rate

m_α	mass of α
n	molar number
n_α	specific molar number of α
p	pressure
r	radius
s	entropy
t	time
u	velocity
u_i	velocity in i-direction
$\mathbf{x}$	spatial location
x_i	spatial coordinate in i-direction

Greek letters, upper case

Δ	filter width
Δ_c	local axial coordinate attached to the GMLI
Δh_α^0	formation enthalpy of α at the reference temperature
Γ	total diffusion coefficient
Ω	flow domain
Ψ	chemical potential function

Greek letters, lower case

α	pressure relaxation coefficient

β_l	pressure loss coefficient
β_t	transverse damping parameter
δ	Dirac delta function
δ_{ij}	Kronecker delta
η_i^n	dichotomic random vector
η_p	pressure relaxation factor
γ	heat capacity ratio
κ	entropic fluctuations
λ	wave length
μ	dynamic viscosity
μ_{sgs}	*sgs* stress
ω	vorticity wave
$\dot{\omega}_\alpha$	chemical source term
$\dot{\omega}_h$	external heating source
ϕ	equivalence ratio
ϕ_α	reactive scalar
ψ_α	sample space of the random ϕ_α
ρ	density
σ	Uniform diffusion coefficient
τ	specific time

τ_{ij}^{sgs}	*sgs* stress
θ	phase angle
ξ	compositional fluctuations
ζ_{α}^{n}	the $n-$th stochastic field of α
0	reference status

Sub- and superscripts

α	scalar
i, j, k	*i,j,k*-direction
∞	far field
n	JANAF coefficients
t	transverse index

Acronyms / Abbreviations

ARM	augmented Reduced mechanisms
BOFFIN	BOundary-Fitted Flow INtegrator
CDS	Central Differences Scheme
CFD	Computational Fluid Dynamics
CFL	Courant–Friedrichs–Lewy
C-S	Crank-Nicholson
CVC	central vortex core
DLR	German Aerospace Centre

DNS	Direct Numerical Simulation
E-M	Euler-Maruyama
EWG	Entropy Wave Generator
FDF	flame describing functions
FFT	fast Fourier transformation
FTF	flame transfer functions
GMLI	gas mixing layer interface
HRR	heat release rate
IRZ	inner recirculation zone
ISL	inner shear layer
JANAF	Joint-Army-Navy-Air-Force
LES	Large-Eddy Simulations
lhs	left-hand-side
NSCBC	Navier Stokes characteristic boundary conditions
OH-PLIF	OH Planar Laser Induced Fluorescence
OH-CL	OH chemiluminescene
onr	oxygen to nitrogen ratio
ORZ	outer recirculation zone
OSL	outer shear layer
pdf	probability density function

PIV	partial image velocimetry
POD	Proper Orthogonal Decomposition
PP	perfectly premixed
PSD	power spectral density
PVC	Precessing Vortex Core
QSS	quasi steady state
RANS	Reynolds-averaged Navier-Stokes
rhs	right-hand-side
rms	root mean square
sgs	sub-grid scale
SP	stagnation point
TCF	Turbulent Counter-flow Flame
TGP	Turbulence Generating Plate
TP	technically premixed
TVD	Total Variation Diminishing
VR	vortex ring

Chapter 1

Introduction

1.1 Backgrounds

One of the greatest challenges to date is to meet the increasing worldwide demand for energy with reliable and environmentally friendly energy supplies. Although alternative energy sources (solar power, wind power and nuclear power etc.) are under active development and use in recent years, the concerns regarding efficiency, safety, cost and seasonal intermittency are limiting their development. Power generation and energy supply by means of combustion with heavy reliance on fossil fuels are expected to remain dominant in the foreseeable future, especially for high-power density applications [1]. In 2021, as the world entered the second year of the Covid-19 pandemic, the accelerating roll-outs of vaccinations and fiscal responses to the economic crisis boosted the economic rebound from the impact of the pandemic leading to an increase in global energy demand by about 4.6% compared to that of 2020. Among all the energy resources, demand for all fossil fuels was set to grow significantly in 2021 (e.g. Coal demand alone is projected to increase by 60% more than all renewable energy combined) [2]. To cope with this and future generations' needs and achieve targets such as the reduction of emissions and the efficiency increase, the physical processes of combustion need to be understood to a better extent.

[1] https://www.iea.org/reports/global-energy-review-2019
[2] https://www.iea.org/reports/global-energy-review-2021?mode=overview

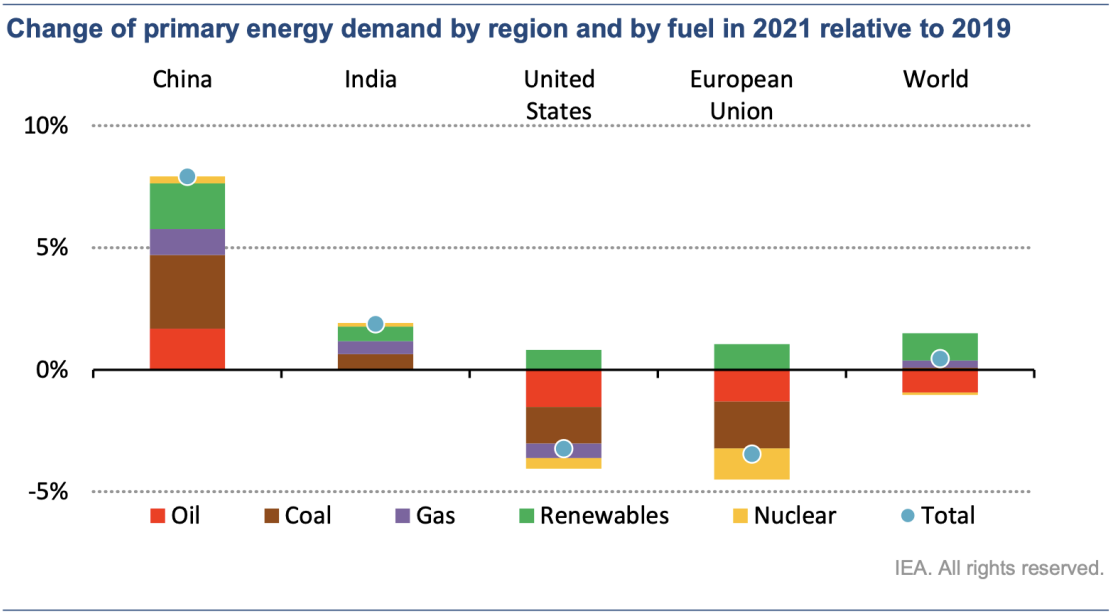

Figure 1.1: Energy demand by fuel in 2021 compared to 2019 in primary energy demand by regions. Images adapted from [2].

Fuel-lean premixed combustion, in which the fuel–air mixture contains a controlled excess of air, has the potential to fulfil both requirements of emission control and efficiency boost (Swaminathan & Bray 2011), and hence is often employed in modern combustor design. Although most combustion devices are designed to operate in stable regimes, combustors under lean premixed operations are sensitive to flow perturbations and can exhibit unexpected self-excited combustion instabilities which are typically only detected during late-stage prototype testing (Poinsot 2017). These combustion instabilities give rise to additional noise and vibration which can lead to serious problems including transient combustor issues such as local-extinction and ignition, flame blow-off, flashback, increased thermal load to the burner and even engine failure (Correa 1998).

In general, combustion instabilities (often referred to as thermo-acoustic instabilities) are driven and controlled by a variety of complex, highly non-linear physical mechanisms (Lieuwen & Yang 2006). When the unsteady heat release excites natural acoustic modes of the combustion chamber, a feedback loop between the combustion chamber acoustics and the unsteady reactive flow field is established, which generally couples the downstream flow to the upstream region. Candel et al. (2012) summarised some of the elementary processes involved in combustion instabilities as shown in Fig. 1.2.

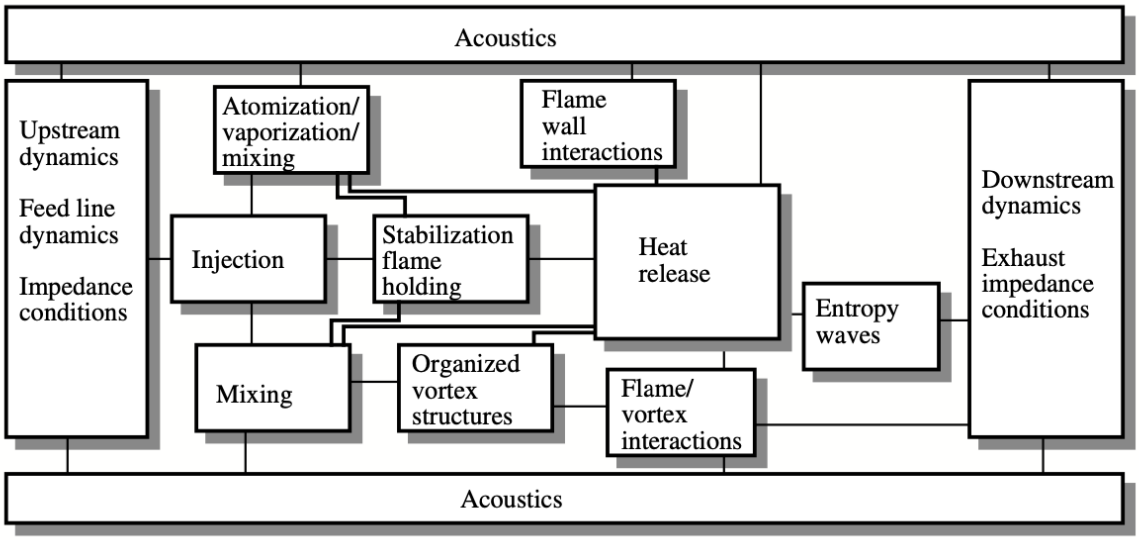

Figure 1.2: Basic elementary mechanisms triggering combustion instabilities. Images adapted from Candel et al. (2012).

Actually combustion instabilities involve almost all usual sciences in reacting flows (kinetics, transport, fluid mechanics, thermodynamics) but also requires the introduction of acoustics, hydrodynamic stability, dynamical systems and control theory. A widely used approach to determine whether the coupling between the acoustic field and the unsteady reaction rate leads to instability is the global Rayleigh criterion (Rayleigh 1878) which states the time and volume integral of the pressure and heat release rate (HRR) must be greater than zero for a system submitted to thermo-acoustic instabilities. Hence, these types of instabilities are often characterised by in-phases high-amplitude oscillations of the pressure and HRR. The most likely dynamics resulting from thermo-acoustic instability are 'limit cycle oscillations': the fluctuation amplitudes of flow variables (pressure, velocity and HRR) grow exponentially when the instabilities start before the growth rate drops and the system reaches a saturated state with zero growth rate due to non-linearity in flame response. Operating in such limit-cycle conditions may lead to major problems including higher pollutant emissions and noises, damage of the combustor components, or in severe cases even the failure of the entire device.

Initial works on laminar premixed flames by Fleifil et al. (1996), Dowling (1999) investigated the mechanism of combustion-driven instabilities in fundamental test cases: unsteady combustion generated acoustic waves which can reflect inside a given geometry, propagate back upstream and exert

kinematic effects on the flame 'surface area', thereby modulating its HRR. However, turbulent flames are encountered in most combustion systems, which adds great complexity to the combustion instabilities problem. Turbulence is a complex state of fluid motion, which are intrinsically unsteady involving stochastic fluctuations (Pope 2000). Usually turbulence is described in terms of pseudo-random coherent motions on a wide range of spatial and temporal scales superimposed on some 'mean' flow (Tabor & Baba-Ahmadi 2010). The scale of motions ranges from large scales determined by the geometry of the problem to small scales determined by the viscosity of the fluid. Hence, turbulent combustion involves complex mutual interactions between unsteady flows and chemical reactions over a variety of temporal and spatial scales, leading to broadband fluctuations in heat release. Small-scale wrinkling of the reaction layers introduced by small-scale turbulence is an additional factor weighing into potential perturbations of the flame's 'surface area'. Random turbulent events can also act as an initial trigger mechanism for self-excited combustion instabilities.

Other physical phenomena contributing to the generation of unsteady heat release are hydrodynamic instabilities. Even in non-reacting flows, the time-averaged flow field can be altered by intrinsically hydrodynamic flow stability dominated by quasi-periodic, large-scale vortical structures. In combustion applications, swirling flows are widely used to aerodynamically enhance the stabilisation of the flame. A comprehensive overview of these phenomena can be found in the reviews by Huang & Yang (2009) and Candel et al. (2014). For a sufficiently high level of swirl, the flow undergoes vortex breakdown, leading to the formation of a central recirculation zone and, under certain conditions, helical flow modes around the centreline of the flow (Lucca-Negro & O'Doherty 2001, Syred 2006). Swirling flames are dominated by complex hydrodynamic flow instabilities and unsteady large-scale structures which, in turn, are also profoundly influenced by combustion-induced heat release. These can lead to different types of periodic mechanisms including perturbations of the turbulent burning velocity via flame angle oscillations (Kim et al. 2010, Palies et al. 2010) and the modulation of flame 'surface area' via the interaction with large-scale coherent structures (Moeck et al. 2012, Caux-Brisebois et al. 2014, Stöhr et al. 2018).

To summarise, the combustion instabilities remain a central issue in designing and constructing successful lean combustion systems, which requires a close and thorough understanding of the relevant

physical processes and their interactions.

1.2 Numerical approaches

A comprehensive understanding of the above-mentioned phenomena involved in combustion dynamics is a key to designing efficient and safe combustion devices. To date, experimental measurement techniques in laboratories are most commonly used to investigate combustion dynamics in turbulent flames. However, the complexity and accuracy of the laboratory flames on combustion instabilities study are restricted by many factors including but not limited to significant expenses, limited optical access, high operating temperatures and pressures inside the test rig, simplified burner geometry and improper acoustic boundary conditions which differ from thoese found in real engines etc.

Computational Fluid Dynamics (CFD) has emerged as an increasingly sophisticated and essential technique. Complementing experimental techniques and theories, CFD is a useful tool to understand the complex processes involved in combustion dynamics as it has the ability to overcome some of the difficulties associated with measurement techniques. Moreover, CFD has gained growing interest as a design tool by industrial users when it comes to reducing the development time and costs of industrial applications. In concept, a CFD calculation represents a 'numerical experiment' (Anderson 1995) providing complete data set from which any quantity of physical significance can be derived. However, these advantages are conditional on the 'accuracy' of the CFD method and there are still a number of remaining uncertainties in terms of the modelling and numerical accuracy of CFD in reacting flows. Further validation and close cooperation with experimentalists to extract the relevant information are both still required for the development of accurate and reliable numerical methods in the application of research on complex physical problems such as combustion instabilities.

Direct Numerical Simulation (DNS) is conceptually the simplest numerical approach and provides the greatest level of detail in the flow: in DNS the unsteady, 3D governing equations are solved numerically; no turbulence model is employed and all scales of motion are resolved. This requires a very fine grid in highly turbulent flow, leading to immense computational requirements especially in study of turbulent reacting flows (Poinsot et al. 1995). Hence the use of DNS to date is mostly limited

to academic or low Reynolds number flow problems. This difficulty is overcome by some form of averaging into the governing equations. Averaging leads to a loss of information, and an appropriate number of model expressions must be devised from an understanding of the controlling physics to close the system. Reynolds-averaged Navier-Stokes (RANS) methods introduce time averaging into the governing equations where all flow quantities are decomposed into time-averaged mean values and their statistical deviations from the mean values. This approach is widely used in industrial applications, as it offers quick solutions with reduced computational costs. However, the level of details provided in RANS is comparatively low due to the time averaging operation and therefore the performance of RANS in highly unsteady flows is relatively poor. Conventional RANS formulations are extended to study transient flow motions leading to the unsteady RANS equations (URANS). Comparisons of URANS to experimental data has been made in various numerical work, see e.g. Benim et al. (2005), Celik et al. (2006), Wang et al. (2017), and limitations of the methods have been found in study of unsteady flow motions. Delafosse et al. (2008) applied URANS to describe hydrodynamics in a reactor stirred by a Rushton turbine, and found out that despite a quite good prediction of total kinetic energy, it fails to reproduce correctly the respective amounts of turbulent and periodic kinetic energy and distribution of turbulent dissipation rate, on which additional work is required to further address the problem.

The balance of accuracy and computing cost required for the accurate prediction of unsteady turbulent flames has led to a significant interest in, and development of Large-Eddy Simulations (LES) in recent years. In LES, the fluid motions are separated into two types with respect to their length scale, which is achieved by spatial filtering of the governing partial differential equations. The large-scale energy-containing motions are resolved both temporally and spatially and the small-scale contributions at the so-called sub-grid scale (*sgs*) level are modelled. These *sgs* motions have short length and time scales in most cases and, at least for the sub-grid fluxes, they exert a much less influential role and are much easier to model than is the case for the corresponding Reynolds averaged stresses and fluxes.

1.3 Predicting thermo-acoustic instabilities: LES approach

LES has proved a useful tool to address unsteady flame dynamics due to its intrinsically unsteadiness which is mandatory for the prediction of combustion dynamics. Besides, as discussed above, large scale coherent structures play an important role in the combustion dynamics, which are, by definition, resolved in the LES. Detailed reviews of numerical prediction using LES method for combustion instabilities can be found in Poinsot (2017).

LES can be used for predicting the combustion instabilities in two modes. The first approach is the forced open-loop LES, where incompressible LES (sometimes termed as 'low Mach number LES') is used together with low-order modelling techniques from acoustic theory (Giauque et al. 2005, Palies et al. 2011, Iudiciani & Duwig 2011, Han & Morgans 2015, Xia et al. 2019). The idea is to decompose the combustor into acoustic elements where the burner itself is seen as one part. The response of a flame to perturbations is often represented by flame transfer functions (FTF) (Bloxsidge et al. 1988) which describe the linear response of the system to low-amplitude forcing or non-linear flame describing functions (FDF) (Noiray et al. 2008) which allow consideration of higher amplitude disturbances. These transfer functions can be determined using LES by externally forcing the burner at a variety of frequencies and amplitudes. The resulting transfer function is then used as input data for acoustic codes (generally a one-dimensional code) to determine the actual occurrence and the characteristic of the combustion oscillation mode in the system. Recently modelling work extends the scope of the flame transfer functions to include the effect of indirect noises, which is found to have increasing importance in the prediction of aero-engine exhaust noise and can affect combustion instabilities (Morgans & Duran 2016). This mainly includes the modelling of entropic indirect noise (Marble & Candel 1977, Goh & Morgans 2011, Christodoulou et al. 2020) and compositional indirect noise (Magri et al. 2016, Ihme 2017, di Domenico et al. 2021). This open-loop approach is attractive for industrial use due to the reduced cost and ability to predict the overall acoustic behaviour of a specific combustor geometry over a wide range of operating conditions. However, given the the complexity of the coupling between the flame and the acoustic field, the modelling can become increasingly complex when different mechanisms involved in the combustion instabilities are to be included. Besides, with the simplification and assumptions on which most of the models base, the method provides lim-

ited insight into non-linear feedback mechanisms associated with the instabilities. One example of the method's limitations is its inability to predict the azimuthal instabilities (Poinsot 2017) in the annual combustors.

A second method is to use a fully compressible LES formulation to compute the entire combustor as a resonator (Poinsot & Veynante 2005). The propagation of acoustic waves is therefore enabled and proper wave reflections can be included by well-defined acoustic boundary conditions. Hence, inherent coupling mechanisms between the flame, flow and acoustics inside a combustion chamber can be directly accounted for and the LES should exhibit the self-excited modes exactly like the what is found in the experiments. Despite the advantages, these self-excited LES methods face many challenges i.e. proper boundary conditions including acoustic impedance at all inlets and outlets should be prescribed and the long transition time from stable to unstable operating conditions observed in some combustors which is almost impractical to compute numerically. Further requirements for the LES study are necessary in order to describe the problem more 'accurately', e.g. An & Steinberg (2019) argued that numerical simulations hence need to be able to reproduce flame extinction due to turbulent straining and hydrodynamic instability, in order to accurately predict the swirling flame configurations. Hence, there are only a limited number of numerical works in the open literature using compressible LES to capture the self-excited modes in the combustors e.g.(Roux et al. 2005, Franzelli et al. 2012, Lourier et al. 2017, Noh et al. 2019, Tachibana et al. 2015, Chen et al. 2019, Fredrich et al. 2021*a*,*b*).

1.4 Objectives and thesis structure

In order to predict self-excited combustion instabilities in gas turbine combustion chambers, a compressible LES code BOFFIN-LES (BOundary-Fitted Flow INtegrator) has recently been devised (Fredrich 2019). A transported probability density function (*pdf*) with a stochastic field method is employed for turbulence-chemistry interaction. The objective of this thesis is to explore and improve the capabilities of this LES method in the study of combustion dynamics. In order to tackle the problems and fill the gaps mentioned in the above introduction, this thesis presents the following tasks:

1. The evaluation of the predictive capabilities of the LES approach in the study of turbulent premixed flames in terms of non-linear dynamics i.e. localised extinctions and re-ignitions. The targeted flame is a turbulent counter-flow flame (TCF), which exhibits large scale transient motions and small scales local-extinction and re-ignition dynamics. It serves as a representative elementary process in combustion dynamics that occurs in real engines. The underlying physics of the local-extinction and re-ignitions in the flames are investigated. The effects of inlet boundary strategy with synthetic turbulence and stochastic field number on the results are assessed. The effect of the equivalence ratio on the flame dynamics is also studied.

2. The evaluation of the LES approach in predicting acoustic amplitudes in a resonator. The target configuration is a non-isentropic nozzle with compositional disturbances imposed at various locations to enable the isolation and identification of the direct and indirect noises generated. The effect of different injecting positions, main jet mass flow rates and injection gases are studied to investigate the noise generation, with the ratio of the indirect to direct noise quantified and analysed.

3. The application of the LES approach on the study of turbulent, reacting flows in complex geometries i.e. lab-scale swirling flames. The method's predictive capabilities under various operating conditions are assessed by comparison with available measurement data. The underlying physics of the governing feedback mechanisms and the related thermo-acoustic and hydrodynamic instability modes are investigated. The flame stabilisation and relation with coherent structures are discussed in particular. Finally, the interplay between the key physics are summarised with diagrams of various degrees of complexity created.

The rest of this thesis is structured as follow: The fundamental background information on the theory and mathematical modelling associated with LES of compressible, turbulent, reacting flows together with the numerical aspects of BOFFIN-LES including the boundary conditions are presented in Chapter 2. The first test case to be presented in Chapter 3 is a turbulent counter-flow flame, which represents an typical elementary reaction in combustors. Chapter 4 assesses the predictive capabilities of the method in a non-isentropic nozzle in noise generation problems. Chapter 5 will describe the investigations of a series of 'technically' premixed flames based on the well-known PRECCINSTA

(Prediction And Control of Combustion Instabilities in Industrial Gas Turbines) combustor, which focuses on the thermo-acoustic and hydrodynamic instabilities in the system and how the results change across the different operating conditions. The main conclusions drawn from this thesis are summarised in Chapter 6 with a brief description of potential directions for future work.

Chapter 2

Theoretical Backgrounds

LES has proved to be a powerful numerical simulation tools to address unsteady flame dynamics by providing better insight into the physical processes associated with the turbulent reacting flows. This chapter introduces and discusses the theoretical background of Large Eddy Simulations (LES) of turbulent reacting flows. The basic thermo-chemical relations and governing equations are described first followed by the filter equations in LES which will be utilised throughout this work. The filtered chemical source terms in the species transport equations include turbulence-chemistry interactions at the small, unresolved sub-grid scales (*sgs*), which are unclosed and require detailed modelling. The properties of various combustion regimes are briefly summarised and the transported probability density function (*pdf*) with stochastic field solution method is finally described. The chapter concludes with a discussion of the boundary conditions applied in the simulations and the numerical facts about the code.

2.1 Governing equations

A generic multi-component reacting flow varying over space and time is governed by the universal laws of conservation of mass, momentum and energy. These conservation principles can be described by a set of non-linear, partial differential equations (*pde*s). A solution to these equations provides in principle all the information we seek from a reacting flow. These *pde*s can be written in a cartesian frame of reference using the Einstein tensor notation as follow. The main quantities appearing in these equations are the time t, the density ρ, the pressure p, the velocity and spatial coordinate in i-direction ($i = [i, j, k]$) by u_i and x_i.

2.1.1 Continuity equations and Navier-Stokes equations

Based on the mass conservation principle, matter cannot be created nor destroyed within a control volume. This leads to the continuity equation written as:

$$\frac{\partial \rho}{\partial t} + \frac{\partial \rho u_i}{\partial x_i} = 0. \tag{2.1}$$

Newton's second law states that the rate of change of momentum of a notional fluid 'particle' equals the sum of the forces on the particle. When applied to a control volume, the momentum conservation equation can be written:

$$\frac{\partial \rho u_i}{\partial t} + \frac{\partial \rho u_i u_j}{\partial x_j} = -\frac{\partial p}{\partial x_i} + \frac{\partial \tau_{ij}}{\partial x_j} + \rho g_i \tag{2.2}$$

where g_i is the gravitational acceleration (assuming that the only body force acting upon the fluid is gravity). Gravity effects can be discarded since the flow of interest is characterised by very high Froude numbers ($u/\sqrt{gL}$) where L is a characteristic length , hence g_i in Eq.2.2 is neglected. τ_{ij} in the Eq. 2.2 denotes the viscous stress tensor, which for a Newtonian fluid can be expressed as a function of the molecular viscosity and the local velocity gradient [1] as follow:

$$\tau_{ij} = 2\mu e_{ij} = 2\mu \left[\frac{1}{2} \left(\frac{\partial u_i}{\partial x_j} + \frac{\partial u_j}{\partial x_i} \right) - \frac{1}{3} \frac{\partial u_k}{\partial x_k} \delta_{ij} \right] \tag{2.3}$$

[1] A Newtonian fluid is a fluid in which the viscous stresses at every point are linearly correlated to the local strain rate.

where μ is the dynamic viscosity, e_{ij} denotes the strain tensor and δ_{ij} is the Kronecker delta. Substitution of the above shear stresses (2.3) into Eq. 2.2 yields the so-called Navier–Stokes equations, named after the two nineteenth-century scientists who derived them independently. Viscosity in gases arises principally from the molecular diffusion that transports momentum between layers of flow and is strongly affected by the fluid's temperature. Its dependence on the temperature can be computed using the standard kinetic theory based on Lennard-Jones potentials for gaseous mixtures (D.W. Perry 2008).

2.1.2 Conservation equations of mass for a species α

In reactive flow, the mass conservation equation of each of the N_s species involved in the reaction needs to be solved. In a multi-component mixture, the mass, molar mass and specific molar number of each species α can be represented by m_α, W_α and n_α respectively, and the mass fraction Y_α and mole fraction X_α are defined as:

$$Y_\alpha = \frac{m_\alpha}{\sum_{\alpha=1}^{N_s} m_\alpha} = n_\alpha W_\alpha \tag{2.4}$$

$$X_\alpha = \frac{n_\alpha}{n} = \frac{n_\alpha}{\sum_{\alpha=1}^{N_s} n_\alpha} \tag{2.5}$$

where n denotes the total specific mole number of the mixture. The transport equation for the species α in the current work are characterised using n_α giving:

$$\frac{\partial \rho n_\alpha}{\partial t} + \frac{\partial \rho u_i n_\alpha}{\partial x_i} = -\frac{\partial J_{\alpha,i}}{\partial x_i} + \rho \dot{\omega}_\alpha \tag{2.6}$$

where $\dot{\omega}_\alpha$ is the chemical source term representing the net formation rate of the species in the reaction. Fick's law of diffusion is used for the species diffusion fluxes $J_{\alpha,i}$ in 2.6) as shown below (Kuo 2005):

$$J_{\alpha,i} = -\frac{\mu}{Sc_\alpha}\frac{\partial n_\alpha}{\partial x_i} \tag{2.7}$$

where Sc_α represents the Schmidt number defined as the ratio of momentum diffusivity (kinematic viscosity) and mass diffusivity as $Sc_\alpha = \mu/\rho D_\alpha$. D_α is the molecular diffusion coefficient for the species α into the multi-component mixture due to the different gradients of species concentration. An equal diffusivity assumption is made for all the species ($D_\alpha = D$, $Sc_\alpha = Sc$) as is common practice in the numerical study of reacting turbulent flows. Hence the sum of Eq. 2.6 over all the species recovers the global mass conservation equation (Poinsot & Veynante 2005).

2.1.3 Conservation equations of energy

There are several different forms of governing equation for energy, depending on the main variable (e.g. energy, enthalpy or temperature). A commonly adopted form in reactive flow is based on the static enthalpy h of the mixture which is the summation of the static enthalpy of each species h_α times its mass fraction:

$$h = \sum_{\alpha=1}^{N_s} Y_\alpha h_\alpha \tag{2.8}$$

from which the temperature can be determined (Bird et al. 2006). h_α includes the sensible enthalpy and the enthalpy of formation, Δh_α^0 at the reference temperature T_0:

$$h_\alpha = \underbrace{\int_{T_0}^{T} c_{p,\alpha} dT}_{sensible} + \underbrace{\sum_{\alpha=1}^{N_s} \Delta h_\alpha^0 Y_\alpha}_{chemical} \tag{2.9}$$

where $c_{p,\alpha}$ is the mass heat capacity of α and Δh_α^0 is the formation enthalpy of each species at the reference temperature T_0 (which is normally set as the $T_0 = 298.15K$ for ease of measurement). Hence, shown by Eq. 2.9, the sensible enthalpy is zero at $T = T_0$. $c_{p,\alpha}$ depends on temperature and can be estimated using the JANAF (Joint-Army-Navy-Air-Force) polynomials [2] as follow:

$$c_{p,\alpha} = \sum_{n=0}^{N_{pol}} a_{n+1} T^n \tag{2.10}$$

[2] https://janaf.nist.gov/

where a_n is the n-th JANAF coefficients. The energy conservation equation is then given by:

$$\frac{\partial \rho h}{\partial t} + \frac{\partial \rho u_i h}{\partial x_i} = \frac{\partial p}{\partial t} + u_i \frac{\partial p}{\partial x_i} - \frac{\partial J_{h,i}}{\partial x_i} + \tau_{ij} \frac{\partial u_i}{\partial x_j} + \rho \dot{\omega}_h \tag{2.11}$$

where $\dot{\omega}_h$ denotes the external heating source terms which may include radiation or an electric spark. The forth term on the right-hand-side (*rhs*) represents the viscous heating effect which is the contribution to the enthalpy of the fluid due to the internal viscous dissipation of kinetic energy. It is generally much smaller compared with the heat released in reaction processes within the framework of subsonic flows (Cant & Mastorakos 2007).

The heat diffusion fluxes $J_{h,i}$ have mainly two contributions: the heat fluxes caused by temperature gradient and the heat fluxes caused by the production or destruction of the scalars. Hence with Fourier law:

$$J_{h,i} = -k \frac{\partial T}{\partial x_i} + \sum_{\alpha=1}^{N_s} h_\alpha J_{\alpha,i} = -\frac{\mu}{Pr} \frac{\partial h}{\partial x_i} - \frac{\mu}{Pr} \left(1 - \frac{1}{Le}\right) \sum_{\alpha=1}^{N_s} h_\alpha \frac{\partial n_\alpha}{\partial x_i} \tag{2.12}$$

where k is the thermal conductivity. Pr is the Prandtl number which is defined as $Pr = \mu Cp/k$. The Lewis number Le is defined as the ratio between thermal diffusivity and the mass diffusivity:

$$Le = \frac{Sc}{Pr} = \frac{k}{\rho Cp D} \tag{2.13}$$

which is usually assumed as unity in the context of turbulent reacting flows (Poinsot & Veynante 2005). Hence, Pr and Sc can be represented with an uniform parameter as σ which is assigned as a universal constant with the value 0.7.

2.1.4 Summary

Table 2.1 summarises the governing equations of reacting flows in the current work, with the appropriate simplifications discussed above. In order to complete the above system of *pde*s, the ideal gas equation of state is introduced to relate :

$$p = n \rho R T \tag{2.14}$$

Continuity
$\frac{\partial \rho}{\partial t} + \frac{\partial \rho u_i}{\partial x_i} = 0$
Navier-Stokes
$\frac{\partial \rho u_i}{\partial t} + \frac{\partial \rho u_i u_j}{\partial x_j} = -\frac{\partial p}{\partial x_i} + \frac{\partial}{\partial x_j}\left[\mu\left(\frac{\partial u_i}{\partial x_j} + \frac{\partial u_j}{\partial x_i} - \frac{2}{3}\frac{\partial u_k}{\partial x_k}\delta_{ij}\right)\right]$
Species
$\frac{\partial \rho n_\alpha}{\partial t} + \frac{\partial \rho u_i n_\alpha}{\partial x_i} = \frac{\partial}{\partial x_i}\left(\frac{\mu}{\sigma}\frac{\partial n_\alpha}{\partial x_i}\right) + \rho\dot{\omega}_\alpha$
Energy
$\frac{\partial \rho h}{\partial t} + \frac{\partial \rho u_i h}{\partial x_i} = \frac{\partial p}{\partial t} + u_i\frac{\partial p}{\partial x_i} + \frac{\partial}{\partial x_i}\left(\frac{\mu}{\sigma}\frac{\partial h}{\partial x_j}\right) + \rho\dot{\omega}_h$

Table 2.1: Conservation equations for reacting flows.

.

2.2 Large Eddy Simulation

Only under restricted conditions (e.g. a laminar flow in a simple geometry) can analytical solution be obtained of the governing *pde*s. For most problem of practical relevance, numerical solution methods have to be adopted to solve the governing *pde*s with the specification of the appropriate initial and boundary conditions. In DNS, all the scales of motion are resolved by directly discretising and solving the Navier-Stokes equations. It is conceptually the simplest method, but the computational cost is also extremely high, as the computational mesh has to be fine enough to capture the small Kolmogorov scales that scale with Reynolds number. The balance of accuracy and computing cost required for the accurate predictions of turbulent flames has led to a significant interest in LES in recent years. With the filtering operation, transport equations can be solved using relatively coarser grids, making the simulation affordable for today's computing resources. Modeling are required for the open terms in the filtered equations which reflect the interaction of the unknown small scales with the resolved ones.

2.2.1 Filter operation

In LES, a spatial filtering operation is applied to the governing equations to separate the energy containing larger scale motions from the small scale motions. The spatial filtering operation of an instantaneous flow variable f at location $\mathbf{x} = (x_1, x_2, x_3)$ can be written as:

$$\overline{f}(\mathbf{x},t) = \int_{\Omega} G(\mathbf{x}-\mathbf{x}';\Delta(\mathbf{x}))f(\mathbf{x}',t)d\mathbf{x}' \tag{2.15}$$

where G is the filter function which must be positive and definite so that the filtered values of scalars remain bounded, and the nature of source terms is preserved (a filter that changes sign may change consumption terms to formation terms). Eq. 2.16 is defined over the entire three-dimensional flow domain Ω, and Δ is the filter width and is traditionally linked to the local mesh spacing $\Delta = (\Delta_i\Delta_j\Delta_k)^{1/3}$ (Vasilyev & Lund 1997). The filtering operation commutes with spatial differentiation if the filter width varies smoothly with position. In the present work, a box filter is a adopted defined as (Schumann 1975):

$$G(x-x',\Delta) = \begin{cases} \frac{1}{\Delta^3}, & if|x-x'| < \frac{\Delta}{2} \\ 0, & \text{otherwise} \end{cases} \tag{2.16}$$

which implies a cell average within the cell volume. The density variations in reacting flows can be treated by introducing a density-weighted filter (also known as Favre filtering) which shares the same property as the unweighted ones and is defined as $\tilde{f} = \overline{\rho f}/\overline{\rho}$.

2.2.2 Filtered equations of fluid motion

With the Favre filtering operation, the filtered continuity equation and momentum conservation equation can be written as follow:

$$\frac{\partial\overline{\rho}}{\partial t} + \frac{\partial\overline{\rho}\widetilde{u}_j}{\partial x_j} = 0 \tag{2.17}$$

$$\frac{\partial\overline{\rho}\widetilde{u}_i}{\partial t} + \frac{\partial\overline{\rho}\widetilde{u}_i\widetilde{u}_j}{\partial x_j} = -\frac{\partial\overline{p}}{\partial x_i} + \frac{\partial}{\partial x_j}\left[\mu\left(\frac{\partial\bar{u}_i}{\partial x_j} + \frac{\partial\bar{u}_j}{\partial x_i} - \frac{2}{3}\frac{\partial\bar{u}_k}{\partial x_k}\delta_{ij}\right)\right] - \frac{\partial\tau_{ij}^{sgs}}{\partial x_j} \tag{2.18}$$

The tilde stands for mass weighted and the overline stands for the conventional filtering. The filtered product $\widetilde{u_i u_j}$ differs from the product of filtered velocities $\widetilde{u}_i\widetilde{u}_j$, and the *sgs* stress τ_{ij}^{sgs} is introduced with the expression:

$$\tau_{ij}^{sgs} = \overline{\rho}\left(\widetilde{u_i u_j} - \widetilde{u}_i\widetilde{u}_j\right). \tag{2.19}$$

where τ_{ij}^{sgs} remains unknown and requires modelling. *sgs* stress tensor can be separated into deviatoric and isotropic parts, while the latter can be neglected in most compressible turbulent flows without much introducing appreciable errors (Erlebacher et al. 1992). Its deviatoric part is approximated via a Smagorinsky model (Smagorinsky 1963) by assuming a gradient diffusion hypothesis for the unresolved sgs stresses and relate it to a sgs viscosity μ_{sgs} as shown below:

$$\tau_{ij}^{sgs} - \frac{\delta_{ij}}{3}\tau_{kk}^{sgs} = 2\mu_{sgs}\left(\widetilde{e}_{ij} - \frac{\delta_{ij}}{3}\widetilde{e}_{kk}\right) \tag{2.20}$$

$$\mu_{sgs} = \bar{\rho}(C_s\Delta)^2||\widetilde{e}_{ij}|| \tag{2.21}$$

where $||\widetilde{e}_{ij}|| = \sqrt{2\widetilde{e}_{ij}\widetilde{e}_{ij}}$ is the Frobenius norm of the resolved the strain rate tensor e_{ij} given by:

$$\widetilde{e}_{ij} = \frac{1}{2}\left(\frac{\partial\widetilde{u}_i}{\partial x_j} + \frac{\partial\widetilde{u}_j}{\partial x_i}\right) \tag{2.22}$$

The use of a sub-grid viscosity μ_{sgs} mimics a diffusion process for the small scale motions, which are expected to be in the dissipation range of the energy cascade (Sagaut 2001). C_s in Eq. 2.21 is the Smagorinsky parameter and is obtained through the dynamic procedure by Piomelli & Liu (1995*a*).

2.2.3 Filtered scalar equations

Application of the density-weighted filter function to the reactive reactive species 2.6 and the static enthalpy 2.11 equations yields following set of filtered equations:

$$\frac{\partial\overline{\rho}\widetilde{n}_\alpha}{\partial t} + \frac{\partial\overline{\rho}\widetilde{n}_\alpha\widetilde{u}_j}{\partial x_j} = \frac{\partial}{\partial x_j}\left(\frac{\mu}{\sigma}\frac{\partial\overline{n}_\alpha}{\partial x_j}\right) - \frac{\partial J_{\alpha,j}^{sgs}}{\partial x_j} + \overline{\rho\dot{\omega}}_\alpha \tag{2.23}$$

$$\frac{\partial \overline{\rho}\widetilde{h}}{\partial t} + \frac{\partial \overline{\rho}\widetilde{h}\widetilde{u}_j}{\partial x_j} = \frac{\partial \overline{p}}{\partial t} + \widetilde{u}_i \frac{\partial \overline{p}}{\partial x_i} + \frac{\partial}{\partial x_j}\left(\frac{\mu}{\sigma}\frac{\partial \overline{h}}{\partial x_j}\right) - \frac{\partial J^{sgs}_{h,j}}{\partial x_j} + \overline{\rho\dot{\omega}}_h \tag{2.24}$$

The first and second term on the left-hand-side (*lhs*) of 2.24 can be shown together as the filtered material derivative of the pressure as:

$$\frac{D\overline{p}}{Dt} = \frac{\partial \overline{p}}{\partial t} + \widetilde{u}_i \frac{\partial \overline{p}}{\partial x_i} \tag{2.25}$$

$\frac{\partial J^{sgs}_{\alpha,j}}{\partial x_j}$ and $\frac{\partial J^{sgs}_{h,j}}{\partial x_j}$ denote the *sgs* fluxes, which are modelled with a gradient diffusion approximation (Schmidt & Schumann 1989) analogous to the Smagorinsky model adopted for *sgs* stress:

$$J^{sgs}_{\alpha,j} = \overline{\rho}\left(\widetilde{u_i n_\alpha} - \widetilde{u}_i \widetilde{n}_\alpha\right) = -\frac{\mu_{sgs}}{\sigma_{sgs}}\frac{\partial \widetilde{n}_\alpha}{\partial x_j} \tag{2.26}$$

$$J^{sgs}_{h,j} = \overline{\rho}\left(\widetilde{u_i h_s} - \widetilde{u}_i \widetilde{h}_s\right) = -\frac{\mu_{sgs}}{\sigma_{sgs}}\frac{\partial \widetilde{h}_s}{\partial x_j} \tag{2.27}$$

with σ_{sgs} representing the sub-grid scale diffusion coefficient (*sgs* Prandtl or Schmidt number), which is often referred to as the turbulent Schmidt number. Given the similarity of the species equation 2.23 and energy equation 2.24, the two equations can be rewritten in terms of a general reactive scalar ϕ_α with $\alpha \in [1, \phi_{N_{sc}}]$, where N_{sc} equals the number of species plus one (enthalpy):

$$\frac{\partial \overline{\rho}\widetilde{\phi}_\alpha}{\partial t} + \frac{\partial \overline{\rho}\widetilde{\phi}_\alpha \widetilde{u}_j}{\partial x_j} = \frac{\partial}{\partial x_j}\left(\frac{\mu}{\sigma}\frac{\partial \overline{\phi}_\alpha}{\partial x_j}\right) - \frac{\partial J^{sgs}_{\alpha,j}}{\partial x_j} + \overline{\rho\dot{\omega}}_\alpha \tag{2.28}$$

where $\overline{\rho\dot{\omega}}_\alpha = \overline{\rho\dot{\omega}}_h + D\overline{p}/Dt$ for the enthalpy. The filtered chemical source terms in the species transport equations remains open ($\overline{\dot{\omega}}(Y_\alpha, x) \neq \dot{\omega}(\overline{Y_\alpha}, x)$), which introduces the main complexity in turbulent combustion modelling.

2.3 Combustion modelling

In the previous section, the basic formulations of Large Eddy Simulation of turbulent reactive flows were outlined and models required to approximate the *sgs* stress and *sgs* fluxes are introduced. The difficulties encountered in evaluating the filtered values of the chemical source terms pose the main

challenge in the modelling of turbulent combustion. The complexity originates from the unknown interaction of turbulence and chemistry which take place at the smallest scales. Turbulence causes strong mixing at a molecular level which may interfere with the flame e.g. eddies at the smallest scales can interact with the reaction zone leading to local-extinction of the flame. Besides the turbulent motions, the chemical reactions occur on different scales making the problem a multi-scale one. Flame causes strong temperature variations and thus density and viscosity changes, which can generate flame induced turbulence or, on the contrary, a reduction in turbulent level due to the strong increase in viscosity under certain conditions (Poinsot & Veynante 2005). Detailed reviews of numerical modelling techniques in LES can be found in Veynante & Vervisch (2002), Pitsch (2006). The combustion model underlying this work is a transported *pdf* approach solved by the Eulerian stochastic fields method, which is presented in this section. Prior to this, however some of the characteristics of the various combustion regimes are summarised.

2.3.1 Combustion regime and models

There are a large number of combustion models, or closure assumptions, that have been proposed over the past few decades. In combustion modelling, most existing models have been proposed specifically for one combustion regime: non-premixed and partially and fully premixed flames. Since chemical reactions between fuel and oxidizer occur only at the molecular level, the mixing between fuel and oxidizer must take place before combustion. In non-premixed combustion the fuel and oxidizer are introduced independently to the reaction zone, primarily by diffusion, where mixing of the fuel and oxidizer occurs before their reaction. In the case of fast chemistry, i.e. chemical reactions having much smaller time scales than the turbulent time scales, the burning rate is limited by the transport and mixing process rather than by the chemical kinetics; the reaction solely occurs due to diffusive molecular mixing. Hence the non-premixed flames are traditionally called ‘diffusion flames’. In premixed combustion, fuel and oxidiser are mixed thoroughly prior to their burning in the chamber. Combustion is initiated normally either by ignition from a spark or by a pilot flame, creating a ‘flame’ that propagates into the unburnt mixture. The flame is characterised by a thin flame front - flamelet - (usually a few millimeters for hydrocarbon fuels in ambient conditions) propagating into the unburned

mixture. In the partially premixed burning regime, parts of the reaction field are governed by premixed flame propagation and finite-rate effects, e.g. auto-ignition, extinction or ignition, while other parts will involve mixing controlled reactions as encountered in diffusion flames. It has been shown in the previous work that it is possible to capture these phenomena within a single LES framework using the present *pdf* method to account for turbulence-chemistry interaction e.g.(Jones & Navarro-Martinez 2007). It has been employed successfully by, e.g.Bulat et al. (2014), Fredrich et al. (2021*a*) in low emissions industrial gas turbines which is highly applicable in the study of gas turbine where partially premixed and diffusion burning arises.

2.3.2 Eulerian stochastic field method for turbulent combustion

The combustion model underlying this work is a modelled transported probability density function (*pdf*) approach where the *pdf* equation is solved by the Eulerian stochastic fields method Valiño (1998). The main advantage of the method lies in its Eulerian formulation which allows a straightforward implementation into a finite volume CFD code. Besides, the fields are smooth and differentiable in space and the solutions do not involve spatially varying stochastic errors. Statistical moments are easy to compute. For detail of the application of the method in LES, see Gao & O'Brien (1998) and Jones & Navarro-Martinez (2007). The reader are referred to Libby & Williams (1994) and Pope (2000) for details of the *pdf* approach.

The sub-grid PDF

The *pdf* $P(\phi_\alpha(\mathbf{x},t) : \psi_\alpha)$ of a random variable can be used to describe the probability of an event occurring. In the present work, the *pdf* of a reactive scalar ϕ_α, $P(\phi_\alpha(\mathbf{x},t) : \psi_\alpha)$, is utilised where ψ_α is the phase (sample) space for the variable $\phi_\alpha(\mathbf{x},t)$. Specifically, $P_\alpha \mathrm{d}\psi_\alpha$ is the probability that $\psi_\alpha \leq \phi_\alpha \leq \psi_\alpha + \mathrm{d}\psi_\alpha$ for all $\alpha = 1,...,N_{sc}$. It is positive definite and satisfies the normalisation condition:

$$\int_{-\infty}^{\infty} P_\alpha(\phi_\alpha)\mathrm{d}\psi_\alpha = 1 \tag{2.29}$$

The one-point, one-time, fine-grained *pdf* can be defined via Dirac delta function δ as:

$$P_\alpha(\psi_\alpha) = \delta(\psi_\alpha - \phi_\alpha) \tag{2.30}$$

where δ has the following properties for variable ψ_α and ϕ_α:

$$\delta(\psi_\alpha - \phi_\alpha) = \begin{cases} 0, & \text{for } \psi_\alpha \neq \phi_\alpha \\ \infty, & \psi_\alpha = \phi_\alpha \end{cases} \tag{2.31}$$

It is worth noting that δ is not a function in the usual sense; instead, it is a generalised function whose definition and properties depend on the integrals:

$$\int_{-\infty}^{\infty} \delta(\psi_\alpha - \phi_\alpha) f(\psi_\alpha) \mathrm{d}\psi_\alpha = f(\phi_\alpha) \tag{2.32}$$

Eq. 2.32 is referred to as sifting property: from the function $f(\psi_\alpha)$, the integral in Eq. 2.32 sifts out the the particular value $f(\phi_\alpha)$. A joint *pdf* for the entire set of scalars $\underline{\psi} = [\psi_i, ..., \psi_{Nsc}]$ is then introduced as the product of the fine-grained *pdf* of each scalar:

$$\mathscr{F}(\underline{\psi}; \mathbf{x}, t) = \prod_{\alpha=1}^{N_{sc}} \delta\left[\psi_\alpha - \phi_\alpha(\mathbf{x}, t)\right] \tag{2.33}$$

where $\underline{\psi}$ is the entire phase space for ϕ_α. When the Favre filtering operation described in section 2.2 is applied to Eq. 2.33, a joint *sgs-pdf* (or filter *pdf*), denoted as $\widetilde{P}_{\mathrm{sgs}}$, can be achieved as follow:

$$\widetilde{P}_{sgs}(\underline{\psi}; \mathbf{x}, t) = \frac{1}{\overline{\rho}} \int_{\Omega} G(\mathbf{x} - \mathbf{x}'; \Delta(\mathbf{x})) \rho \mathscr{F}(\underline{\psi}; \mathbf{x}, t) \mathrm{d}\mathbf{x}' \tag{2.34}$$

where G is the same filter function as in Eq. 2.16. Hence, by definition, $\widetilde{P}_{\mathrm{sgs}}$ describes the probable states of the scalars within the filter volume at each gird point at every instant. All of the one point moments, $\widetilde{\phi}_\alpha^n$ of the scalars can then be obtained from:

$$\widetilde{\phi}_\alpha^n = \int_{-\infty}^{\infty} \widetilde{P}_{sgs}(\underline{\psi}; \mathbf{x}, t) \psi_\alpha^n \mathrm{d}\psi_\alpha \tag{2.35}$$

Transported *pdf* approach

Based on the species and energy equations (Eq. 2.6 and Eq. 2.11) and the application of the chain rule and Favre filtering, an equation describing the evolution of the filtered *pdf* can be obtained, Gao & O'Brien (1998):

$$\begin{aligned}\overline{\rho}\frac{\partial \widetilde{P}_{sgs}(\underline{\psi})}{\partial t}+\overline{\rho}\tilde{u}_j\frac{\partial \widetilde{P}_{sgs}(\underline{\psi})}{\partial x_j}-\frac{\partial}{\partial x_j}\left[\frac{\mu}{\sigma}\frac{\partial \overline{P}_{sgs}(\underline{\psi})}{\partial x_i}\right]+\sum_{\alpha=1}^{N_{sc}}\sum_{\beta=1}^{N_{sc}}\frac{\mu}{\sigma}\frac{\partial\overline{\phi}_\alpha}{\partial x_i}\frac{\partial\overline{\phi}_\beta}{\partial x_i}\frac{\partial^2\overline{P}_{sgs}(\underline{\psi})}{\partial\psi_\alpha\partial\psi_\beta}=\\ \underbrace{-\sum_{\alpha=1}^{N_{sc}}\frac{\partial}{\partial\psi_\alpha}\left[\overline{\rho}\dot{\omega}_\alpha(\underline{\psi})\widetilde{P}_{sgs}(\underline{\psi})\right]}_{chemical\ reaction}\underbrace{-\frac{\partial\overline{\rho u_j F(\underline{\psi})}-\overline{\rho}\tilde{u}_j\widetilde{P}_{sgs}(\underline{\psi})}{\partial x_j}}_{sgs-pdf\ transport}\\ \underbrace{-\sum_{\alpha=1}^{N_{sc}}\sum_{\beta=1}^{N_{sc}}\frac{\mu}{\sigma}\frac{\partial^2}{\partial\psi_\alpha\partial\psi_\beta}\left(\overline{\frac{\partial\phi_\alpha\partial\phi_\beta}{\partial x_j\partial x_j}F(\underline{\psi})}-\frac{\partial\overline{\phi}_\alpha}{\partial x_j}\frac{\partial\overline{\phi}_\beta}{\partial x_j}\overline{P}_{sgs}(\underline{\psi})\right)}_{sgs-pdf\ micro-mixing}\end{aligned} \tag{2.36}$$

Following the approach of Brauner et al. (2016) the resolved part of the micro-mixing term has been subtracted from both sides of the equation. The terms on the *lhs* contain only known variables and requires no special treatments. The first term on the *rhs* is the chemical reaction term, which now appears in closed form and requires only specification of a chemical reaction mechanism. $\dot{\omega}_\alpha(\underline{\psi})$ is the net formation rate through a chemical reaction in the case of chemical species or the pressure derivative $\frac{\mathrm{D}\overline{p}}{\mathrm{D}t}$ and external heat sources for the enthalpy. The second term on the *rhs* represents transport (convection) of *pdf* at *sgs* level due to the fluctuating velocity and is approximated by a gradient closure analogous to the modeling in Eq. 2.26 and Eq. 2.27, with the *sgs* Prandtl/Schmidt number σ_{sgs} assigned the value 0.7:

$$\overline{\rho u_j F(\underline{\psi})}-\overline{\rho}\tilde{u}_j\widetilde{P}_{sgs}(\underline{\psi})=-\frac{\mu_{sgs}}{\sigma_{sgs}}\frac{\partial\widetilde{P}_{sgs}(\underline{\psi})}{\partial x_i} \tag{2.37}$$

The last term on the *rhs* represents *sgs* mixing and describes the effect of molecular diffusion in the *sgs* level on the *pdf*. It is closed by the Linear Mean Square Estimation (LMSE) closure (Dopazo 1975). The mixing time-scale is given by $\tau_{sgs}=\overline{\rho}\Delta^2/\mu_{sgs}$, with the *sgs* mixing constant C_d is assigned the

value of 2 (Jones & Prasad 2010). The resulting closed form of the *pdf* equation becomes:

$$\overline{\rho}\frac{\partial \widetilde{P}_{sgs}(\underline{\psi})}{\partial t}+\overline{\rho}\tilde{u}_j\frac{\partial \overline{P}_{sgs}(\underline{\psi})}{\partial x_j}-\frac{\partial}{\partial x_j}\left[\frac{\mu}{\sigma}\frac{\partial \overline{P}_{sgs}(\underline{\psi})}{\partial x_i}\right]+\sum_{\alpha=1}^{N_{sc}}\sum_{\beta=1}^{N_{sc}}\frac{\mu}{\sigma}\frac{\partial \overline{\phi}_\alpha}{\partial x_i}\frac{\partial \overline{\phi}_\beta}{\partial x_i}\frac{\partial^2 \overline{P}_{sgs}(\underline{\psi})}{\partial \psi_\alpha \psi_\beta}=$$
$$\underbrace{-\sum_{\alpha=1}^{N_{sc}}\frac{\partial}{\partial \psi_\alpha}\left[\overline{\rho}\dot{\omega}_\alpha(\underline{\psi})\widetilde{P}_{sgs}(\underline{\psi})\right]}_{chemical\ reaction}+\underbrace{\frac{\partial}{\partial x_j}\left[\frac{\mu_{sgs}}{\sigma_{sgs}}\frac{\partial \widetilde{P}_{sgs}(\underline{\psi})}{\partial x_i}\right]}_{sgs-pdf\ transport} \tag{2.38}$$
$$\underbrace{-\frac{C_d}{2\tau_{sgs}}\sum_{\alpha=1}^{N_{sc}}\frac{\partial}{\partial \psi_\alpha}\left[\overline{\rho}\left(\psi_\alpha-\widetilde{\phi}_\alpha(\mathbf{x},t)\right)\widetilde{P}_{sgs}(\underline{\psi})\right]}_{sgs-pdf\ micro-mixing}$$

It it worth noting that both *sgs-pdf* terms involves contribution from *sgs* fluctuations only and are identically zero when *sgs* variance are zero, e.g. the fluctuations in all quantities over the filter volume are negligible. The main advantage of the transported *pdf* approach lies in that the chemical reaction terms appear in a closed form and that no combustion regime dependent modelling assumptions are invoked. The main obstacle to solving the *pdf* transport equation Eq. 2.38 is the high dimensionality of the equation: the joint *pdf* depends on space, time and all independent scalars. When standard difference methods are used, the computational cost increases exponentially with the number of total species, which is not feasible even with reduced mechanism adopted. Thus the only feasible method for solving the pdf equation are stochastic methods. The classical approach to solving the transported *pdf* equation are Lagrangian particle methods (Pope 1981, 2000) first introduced in the context of RANS, and extended to LES by Colucci et al. (1998), Raman et al. (2005), Pitsch (2006). In these methods, the *pdf* is described by a set of notional particles so that a separate Lagrangian particle solver must be coupled to the Eulerian momentum an continuity.

The stochastic field method

A more recent formulation is based on a pure Eulerian representation of the *pdf* and was first devised by Valiño (1998) and initially adopted in RANS context by Hauke & Valiño (2004). It was further developed in LES by Jones & Navarro-Martinez (2007, 2008), Jones & Prasad (2010) and is adopted in the present work. The joint *pdf* described by Eq. 2.38 is represented by an ensemble of N_{sf}

stochastic fields ζ_α^n with $n \in (1, N_{sf})$ spanning over the entire spatial domain. An equivalent system of stochastic differential equations (*sdes*) to represent the modelled transport *pdf* equations Eq. 2.38, which can be obtained either with the Itô or Stratonovich interpretation of the stochastic integral, see (Gardiner 1985). In the present work, the Itô formulation is adopted following Valiño (1998) and Sabel'nikov & Soulard (2005) and the stochastic fields evolve according to:

$$\bar{\rho}\mathrm{d}\xi_\alpha^n = \underbrace{\left[-\bar{\rho}\tilde{u}_i\frac{\partial \xi_\alpha^n}{\partial x_i} + \frac{\partial}{\partial x_i}\left(\Gamma\frac{\partial \xi_\alpha^n}{\partial x_i}\right) - \frac{C_d\bar{\rho}}{2\tau_{sgs}}\left(\xi_\alpha^n - \widetilde{\phi}_\alpha\right) + \bar{\rho}\dot{\omega}_\alpha^n(\underline{\xi}^n)\right]\mathrm{d}t}_{a(\xi)\mathrm{d}t} + \underbrace{\sqrt{2\bar{\rho}\frac{\mu_{sgs}}{\sigma_{sgs}}}\frac{\partial \xi_\alpha^n}{\partial x_j}\mathrm{d}W_i^n}_{b(\xi)\mathrm{d}W} \tag{2.39}$$

where $\Gamma = (\mu/\sigma + \mu_{sgs}/\sigma_{sgs})$ represents the total effect of the molecular and *sgs* diffusion coefficient. $\mathrm{d}W_i^n$ represents the Wiener process (Gardiner 1985) for each stochastic field n and each spatial component i, but is independent of spatial location $\mathbf{x}$. The Wiener process is approximated by $dW_i^n = \eta_i^n(\sqrt{\mathrm{d}t})$, where $\eta_i^n \in [-1, 1]$ represents a dichotomic random vector with zero mean and a variance of unity. The stochastic fields are continuous and differentiable in space and continuous but not differentiable in time (Valiño 1998). The fields are also smooth on the level of the filter width, which means they contain no hidden *sgs* scales and they do not vary within the filter cell. Equation 2.39 is a pure Eulerian formulation describing the evolution of a set stochastic fields representing a *pdf* whose modelled transport equation is Eq. 2.38. The solutions of the stochastic field equation Eq. 2.39 are not to be mistaken with any particular realisation of the real field, but rather form an equivalent stochastic system in the sense that all the one-point moments resulting from Eq. 2.39 and from the solution of Eq. 2.38 are the same. One of the most obvious advantages of this method is due to the Eulerian properties of the stochastic fields, conventional LES solvers can be adopted. Another major advantage is that the solutions contain no spatial stochastic errors so the the resulting density field is smooth and thus there are no stochastic errors arising in the velocity and continuity equations. All of the first point moments can be obtained by:

$$\widetilde{\phi}_\alpha^m = \frac{1}{N_{sf}}\sum_{n=1}^{N_{sf}}(\xi_\alpha^n)^m \tag{2.40}$$

Further details of the solution method and its implementation can be found in the previous work e.g. (Jones & Prasad 2010).

2.3.3 Chemical mechanism

In the study of turbulent reacting flows, due to the large number of reaction steps and chemical species involved in detailed kinetic schemes, it is not practical to utilise detailed mechanisms in the modelling of practical combustion systems. Systematically reduced mechanisms derived from the complete detailed schemes offer a convenient way of reducing the number of species involved in the combustion kinetics while maintaining an acceptable level of accuracy; they reproduce important combustion attributes such as laminar burning velocity, flame structure, ignition delays, extinction limits etc. In the study of flame dynamics, in order to correctly reproduce finite-rate chemistry effects such as local flame extinctions and re-ignitions, an accurate description of the chemical reactions is required. In the present BOFFIN-LES solver, two different reduced mechanisms for methane oxidation are included, which are both derived from the full detailed GRI-Mech 3.0 [3] by Sung et al. (2001) and Lu & Law (2008), respectively. Both mechanisms involve 15 steps and 19 species as shown in Table 2.2 and Table 2.3, respectively. The 15-step/19 species mechanism described and validated in Sung et al. (2001) has been shown to be capable of predicting a wide range of complex flame phenomena with satisfactory accuracy. Here a quasi-steady state (QSS) analysis is applied for minor intermediates, that is, to assume the rates of production and consumption are much greater in magnitude than the net rate of change of the species concentration. In the 15-step mechanism derived by Lu & Law (2008), the QSS species concentrations are solved analytically compared to the traditional algebraic iteration method is used in Sung et al. (2001). Besides, NO chemistry is excluded in the mechanism but can be added through an extended version with 17 steps and 21 species if required (Lu & Law 2008). Both mechanisms deliver similar results, while considerable speedup of the simulation can be achieved with the reduced mechanism by Lu & Law (2008) due to its analytical solution strategy, and the convergence issues that may arise in the solution of the concentrations of the QSS species are also prevented. The mechanism of Lu & Law (2008) was shown to perform noticeably faster with a reduction of computational time by more than half by Fredrich (2019).

[3] http://combustion.berkeley.edu/gri-mech/version30/text30.html

Step	Reaction
1	$CH_4 + H = CH_3 + H_2$
2	$CH_3 + OH = CH_2O + H_2$
3	$CH_2O = CO + H_2$
4	$C_2H_6 = C_2H_4 + H_2$
5	$C_2H_4 + OH = CH_3 + CO + H_2$
6	$C_2H_2 + O_2 = 2CO + H_2$
7	$CO + OH + H = CO_2 + H_2$
8	$H + OH = H_2O$
9	$2H_2 + O_2 = 2H + 2OH$
10	$2H = H_2$
11	$HO_2 + H = H_2 + O_2$
12	$H_2O_2 + H = H_2 + HO_2$
13	$O_2 + H_2 = 2NO$
14	$HCN + H + O_2 = H_2 + CO + NO$
15	$NH_3 + 3H + H_2O + 4H_2 + NO$

Table 2.2: 15-step reduced mechanism by Sung et al. (2001).

2.4 Boundary conditions and treatments

In order to solve the transient equations discussed in the previous sections, a correct prescription of the boundary conditions is required. The proper choice of boundary conditions is a critical issue in compressible LES. They depend not only on physical boundary conditions to ensure well-posedness, but also the 'numerical' implementation of boundary conditions involving extrapolation of variables and numerical scheme selected. The following section aims to identify the questions and present the boundary conditions utilised in BOFFIN-LES code.

2.4.1 Inlet boundary

The distribution of transported flow variables must be specified at inlet boundaries. With prescribed variables such as velocity, density, temperature and mixture compositions other quantities can be computed from ideal gas law. However, it is not usually so straight forward when dealing with

Step	Reaction
1	$2O = O_2$
2	$H + O = OH$
3	$O + CH_3 = H + CH_2O$
4	$O + CO = CO_2$
5	$H + O_2 = HO_2$
6	$2H = H_2$
7	$H + OH = H_2O$
8	$H + CH_3 = CH4$
9	$H + CH_2CO = CH_3 + CO$
10	$H_2 + CO = CH_2O$
11	$2OH = H_2O_2$
12	$OH + CH_3 = CH_3OH$
13	$2CH_3 = C_2H_6$
14	$C_2H_4 = H_2 + C_2H_2$
15	$O + C_2H_2 = CH_2CO$

Table 2.3: 15-step reduced mechanism by Lu & Law (2008).

turbulent inlet flows.

With LES, the three-dimensional velocity field and energy-containing turbulent motions are resolved both temporally and spatially. This requires an accurate prescription of the boundary conditions, which can influence the overall simulation results significantly (Keating et al. 2004). Ideally what is needed is a detailed knowledge of the turbulence levels and structure, at the inlet boundaries but such comprehensive temporal measurements are impracticable. As an alternative two simulation strategies are often selected: running a separate precursor calculation upstream the region of interest, or estimating the inlet boundary conditions with the use of a synthetic turbulence generator. Precursor simulation methods perform some form of explicit simulation of the upstream flow to generate a 'library' of turbulent data which can be introduced into the main computation at the inlet. This method has the merit that the inflow conditions are achieved from a genuine simulation of turbulence, thereby should satisfy many of the required turbulent characteristics, including spectra, Reynolds stress tensors, and all moments. However, this method can be costly for most applications, and the implementation and adjusting effort can be great in many cases.

Synthesis techniques aim at re-constructing a random field at the inlet with suitable turbulence-like properties using mathematical processes, which have the advantages that they can be easily manipulated with a small range of adjustable parameters to specify the desired turbulent properties, for instance turbulent length scales or energy levels. A simple method to introduce artificial unsteadiness at the inlet would be superimposing a white-noise random component to the inlet velocity. However, the energy in such a turbulent field is equally distributed over the entire wave-number range (Dhamankar et al. 2018), which disagrees with the description of physical turbulence in which the well-resolved low-wave-number range (or the large scales of turbulence) has a higher energy content (Pope 2000). Due to the lack of spatial or temporal coherence, the white noises can be instantly destroyed before triggering the transition to realistic turbulence (Lund et al. 1998). Therefore more sophisticated synthesis techniques thus concentrate on generating more 'realistic' fluctuations by introducing some degree of spatial and temporal coherence. Klein et al. (2003) designed digital filters capable of establishing a Gaussian two-point correlation function in random fluctuations. This filtered random signal features the required spatial length scales and can be further re-scaled to obtain a prescribed Reynolds stress tensor. The procedure has been further extended by di Mare et al. (2006) with a sophisticated formulation that does not presume a specific correlation function shape and is able to satisfy a prescribed Reynolds stress tensor, along with locally defined spatial and temporal correlation functions. This improved method was suggested to have be better performance in wall-bounded flows compared to the original version. And hence, the digital turbulence generator proposed by di Mare et al. (2006) is included in the present BOFFIN-LES solver. This technique has been applied for many LES study with success, e.g. in Jones et al. (n.d.), Bini & Jones (2008), Navarro-Martinez & Kronenburg (2011). Detailed reviews of numerical approaches to prescribe inlet boundary conditions for transient simulation can be found in Keating et al. (2004), Tabor & Baba-Ahmadi (2010), Dhamankar et al. (2018).

2.4.2 Outlet boundary

The most significant concern about outlet boundaries is no disturbances originated at the domain outlet propagate upstream. BOFFIN features different types of outlet boundary conditions as discussed

in the following section.

Zero gradient and constant pressure outlet boundary condition

For incompressible flows a simple approximation for the outlet boundary conditions is to assign zero gradient normal to the outlet boundary for all quantities, implemented via zero order approximations or, alternatively, to fix the pressure to a constant value with all other quantities extrapolated from interior points. The latter case corresponds to a fully reflective boundary. The zero gradient approximation can minimise the effects of the boundary on the solution only if the flow can be considered uni-directional. Hence when zero-gradient outlet boundary conditions are adopted, the outlet boundary is always located as far downstream of the region of interest as possible to minimise the effects of the boundary on the simulation in the regions of interest. These conditions are, however unsuited to compressible flows.

Non-reflective boundary condition

Unsteady simulations of compressible flows with low numerical dissipation (LES or DNS) require an accurate control of wave reflections at the computational boundaries, including physical waves (e.g. acoustic waves) and numerical waves (wiggles). The modelling of physical wave reflections is a challenging problem due to the unknown acoustic impedance at the boundaries. Numerical waves are referred to as the fluctuations generated by the interaction of discrete treatment and unsteady perturbations. These waves are spurious and can interact with boundary conditions or may propagate upstream and interact with the flow (Poinsot & Lele 1992), which causes major problems. A common method to tackle these problems is to apply non-reflecting or absorbing boundary conditions, one of which is a technique developed based on the characteristic wave decomposition, the so called characteristic boundary conditions. BOFFIN features a subsonic non-reflective outlet boundary conditions for the study of compressible flows, a short review and brief descriptions of which are provided below.

The characteristic boundary conditions adopted in the present work were developed based on the analysis of characteristic lines for the hyperbolic systems of Euler equations (Engquist & Majda

1977, Rudy & Strikwerda 1980, Thompson 1987) for inviscid flows. Poinsot & Lele (1992) extended the method to include viscous term, e.g. viscous dissipation thermal diffusion and species diffusion, to formulate Navier Stokes characteristic boundary conditions (NSCBC). The NSCBC approach was further extended by Yoo & Im (2007), Yoo et al. (2005) to include the transverse gradient terms, and by Lodato et al. (2008) to account for convection and pressure gradients resulting in a 3D NSCBC approach. The non-reflective outlet boundary conditions adopted in the present work is based on the approach of Rudy & Strikwerda (1980) supplemented with viscous term suggested by Poinsot & Lele (1992) and transverse term proposed by Yoo & Im (2007), Yoo et al. (2005). The resulting outflow boundary conditions are given by:

$$\left(\frac{\partial p}{\partial t}+\rho c\frac{\partial u_i}{\partial t}\right)+\underbrace{\alpha(p-p_\infty)}_{\textit{pressure relaxation term}}+\underbrace{\beta_t\left(u_t\frac{\partial p}{\partial x_t}+\gamma\frac{\partial u_t}{\partial x_t}-\rho c u_t\frac{\partial u_i}{\partial x_t}\right)}_{\textit{transverse term}}=0 \tag{2.41}$$

where c is the speed of sound and u_n and u_t are the velocity components normal and tangential to the outlet boundary and t is the transverse index varying from j to k. The pressure relaxation term includes the target far field pressure (ambient pressure) p_∞ and the pressure relaxation coefficient α is given by:

$$\alpha=\eta_p c\frac{(1-M^2)}{L} \tag{2.42}$$

where M denotes the average Mach number at the outlet boundary, L is the length of the computational domain and η_p is the pressure relaxation factor assigned as 0.28, which is found in Rudy & Strikwerda (1980) to be an optimal value to allow the boundary pressure to converge rapidly while suppressing the unwanted incoming waves. β_t is the transverse damping parameter set equal to M according to Yoo et al. (2005) and γ is the heat capacity ratio (also known as isentropic expansion factor) which is the ratio of the specific heat of a gas at constant pressure to that of a gas at constant volume (C_p/C_v) and arises because a classical sound wave induces an adiabatic compression, in which the heat of the compression does not have enough time to escape the pressure pulse, and thus contributes to the pressure induced by the compression. It is related to the speed of sound by $c=\sqrt{\gamma RT}$. The strategy to apply NSCBC at outlet boundaries in the present work is as follow: first the velocity and the

density are obtained using zero gradient boundary condition (from the interior nodes), after which the pressure can be achieved using the NSCBC given by Eq. 2.41. And the temperature can then be computed using ideal gas law. The effective implementation of the NSCBC into BOFFIN has been demonstrated previously by Fredrich (2019) using two test cases which are extensively used in the open literature.

2.4.3 Walls

For wall bounded flows, BOFFIN-LES features different types of non-slip wall boundary conditions according to the near wall resolutions. If the mesh is fine enough to provide a full resolution of the viscous sublayer , natural non-slip wall conditions $\tilde{u}_i = 0$ are applied directly. However, turbulent wall bounded flows are multi-scale phenomena and at high Reynolds number, the viscous sub-layer becomes progressively small with the consequence that the computational cost of resolving the viscous sub-layer become close to that required by DNS (Larsson & Kawai 2010). In this case, full resolutions of the viscous sub-layer is not feasible and approximate boundary conditions are hence adopted. In BOFFIN-LES, the wall model of Schumann based on the logarithmic law of the wall and described in Balaras et al. (1996) is applied to all solid boundaries. Despite the insufficient resolution of the boundary layer turbulence structure, such an approximate near wall treatment is likely to provide reasonably accurate time-averaged wall heat transfer rates (Hoffmann & Benocci 1995, Piomelli & Liu 1995*b*). The scalars at solid boundary are described using Dirichlet (fixed value) or Neumannn (fixed flux) boundary conditions. The former can be used for iso-thermal walls with imposed temperature ($\tilde{T} = T_w$) and the latter can be used in describing adiabatic walls with zero heat flux through the wall.

2.5 BOFFIN-LES code

The computational method utilised throughout this work is the code BOFFIN-LES (Fredrich et al. 2021*b*), a development of the in-house, incompressible BOFFIN-LESi (Jones et al. 2002). This in-

compressible code has been developed and validated to a wide range of reacting flow problems including (Jones & Prasad 2010, Bulat et al. 2014, Jones et al. 2015, Brauner et al. 2016, Gallot-Lavallée et al. 2017, Noh et al. 2018, Xia et al. 2019, Fredrich et al. 2019).

BOFFIN-LES is a fully compressible, block-structured LES based on a finite volume method (Ferziger & Perić 2002). It utilises a pressure based approximate factorisation formulation along with the pressure smoothing algorithm of Rhie & Chow (1983). Details of the algorithm and its implementation in BOFFIN-LESc are described in Fredrich et al. (2021*b*) and (Fredrich 2019) and thus will not be discussed further in the present study. For the momentum equation the convection terms are discretised using an energy-conserving discretisation scheme and the discretisation for all other spatial terms are approximated by second-order central differences scheme (CDS). For the stochastic fields equations, a total variation diminishing (TVD) scheme is used for the convection terms to avoid unphysical overshoots and resulting second law violations, along with CDS and an approximately factored Euler-Maruyama scheme for the stochastic term (Kloeden & Platen 1992). The advancement in time is performed with a second-order Crank-Nicholson scheme. For further details of the spatial and temporal discretisation schemes used in BOFFIN, the reader is referred to Jones et al. (2012). For an overall review on numerical techniques and schemes the reader is referred to the texts by Ferziger & Perić (2002), Versteeg & Malalasekera (2007).

Chapter 3

Model Validation: Investigation of Premixed Turbulent Counter-flow Flames

The first test case investigated is a series of fully-premixed turbulent counter-flow flames (TCF), with CH_4/air flames impinged by hot product counter-flow. Such a configuration can be used to study premixed flames undergoing intense strain with unsteadiness brought about by turbulent eddies and mixing and heat exchange with combustion products. These processes are typical of combustors with shear layer, flow impingement or vortex breakdown, e.g. in swirl-stabilised combustors. The incompressible flow assumptions are invoked for the scope of this chapter, and the proposed transported *pdf*/ stochastic field approach is utilised to simulate the sub-grid scale turbulence-chemistry interactions. The specific objectives are to evaluate the LES approach in the study of highly turbulent strained flames with non-linear dynamics and to investigate the mechanism of local-extinction and re-ignition in the case considered.

3.1 Background and motivations

Turbulent flames involve complex mutual interactions between unsteady flows and chemical reactions over a variety of temporal and spatial scales, which poses a great challenge for combustion research. Numerical simulations can provide researchers with further understanding of the turbulence-chemistry interactions, as they have the abilities to overcome the difficulties associated with measurement techniques. A variety of flame benchmarks have been established as targets for the TNF (Turbulent Non-premixed Flames) Workshop, which encourages discussions and collaborations of experimental and numerical research work on turbulent flames (Kempf 2007). As one of the target flames, turbulent counter-flow flames (TCF) provide a convenient benchmark for the study of phenomena relevant to practical combustion systems, and hence have been subjected to numerous investigations, with many attractive features such as simple flame shape, well-controlled boundaries and flexible operation modes.

In early experimental studies, Kostiuk et al. (1989, 1993*b*,*a*) examined a TCF with two axisymmetric premixed reactant streams, where the turbulence was generated by having the mixture flow through perforated plates in the nozzles. Mastorakos et al. (1992*a*,*b*) used this configuration to investigated the extinction limits and relative temperature characteristics in non-premixed and partially premixed TCF. It was observed that partially premixed flames were more resistant to extinction, and these TCF were reproduced numerically by Jones & Prasetyo (1996) using a RANS based *pdf*-transport approach. Sardi et al. (1999) continued this work with the measurements of conditional scalar dissipation rates in an iso-thermal opposed jet, and the results have been used for comparison in many computational studies (Kempf et al. 2000, J Eckstein et al. 2000). Korusoy & Whitelaw (2001, 2002) further performed the measurements of the velocity and strain rate in the iso-thermal flow with small separations of the nozzles. At Darmstadt University, Geyer et al. (2005*b*,*a*) developed an opposed jet burner and performed a series of measurements of iso-thermal and premixed TCF, including information on axial velocity, main species concentration, temperature and structure functions etc. These comprehensive descriptions of the flames provided rich information for the validation of the LES work. Recently at Yale University and Sandia National Laboratories, Coppola & Gomez (2009) and Coriton et al. (2011, 2013) developed a TCF burner aimed at creating highly turbulent flames and investigated its

extinction features. Pettit et al. (2011) reported works involving experimental and numerical investigations of diffusion flames with this burner. Tirunagari & Pope (2016), Tirunagari et al. (2016) studied the premixed mode of the burner numerically. The computational domain focused on the cylindrical region between the two nozzles exit planes with the inlet boundary conditions achieved from a simulation of the iso-thermal case with the domain extended to the nozzle inlets.

Turbulent opposed jet configurations are known to be prone to large scale instabilities. These are likely to be associated with the impingement of the jets resulting in both longitudinal fluctuations and tilting of the gas mixing layer between the jets which is easily observed by the naked eye during experiments or in snapshots of OH Planar Laser Induced Fluorescence (OH-PLIF) images (Gomez 2011). Because of the close proximity of the nozzle outlets to the impingement plane these instabilities are likely to be influenced by the details of the inflow jet turbulence and thus by the method used to generate turbulence upstream of the jet inlet, e.g. perforated plates or grids (Gomez 2011). The origins of the instabilities are not well understood, but they are clearly related to turbulent fluctuations since they are not detected under laminar conditions. The instabilities are the cause of the discrepancy between experimental measurements and predictions identified by Geyer et al. (2005*a*) and Lindstedt et al. (2005). Coppola & Gomez (2009), Coppola (2010), Gomez (2011) studied this instability in an iso-thermal TCF using Proper Orthogonal Decomposition (POD), and the existence of two modes of oscillation of the mixing layer, namely an axial one and a precessing one about the system axis were detected. They also confirmed these large-scale, low-frequency instabilities are chaotic in nature and typically exhibit large length and time scales. The POD analysis was extended to the OH-PLIF images under reacting conditions (Gomez 2011), which confirms the large-scale fluctuations of the mixing layer induce similar motions of the flame. These motions were found to to have little influence on the detailed instantaneous flame structure (Gomez 2011) but mainly affected the flame positions. Hence, in the study of turbulence-flame interaction it is natural to seek methods to filter out the effects of these large-scale fluctuations. A conditional algorithm was proposed and demonstrated to be capable of achieving this (Coppola 2010, Gomez 2011). It allows the study of turbulence-flame interactions, is hence incorporated in the present work and is described in detail in Section 3.4.4.

3.2 Case description

In the present work, the Yale premixed TCF (Coriton et al. 2013) is studied numerically using BOFFIN-LES. The burner system is presented schematically in Fig. 3.1, and detailed descriptions of it can be found in the experimental work by Coppola & Gomez (2009), Coriton et al. (2011). The present work aims to study the coupling effect of the turbulent flow field and the flame and to assess the predictive capabilities of the filtered *pdf*/stochastic fields method in reproducing this premixed TCF. Particular attention is paid to the fluctuations of the flow field and local-extinction and re-ignition phenomenon. Despite many previous studies of the TCF configuration, there is a limited availability of computational studies of localised extinctions in premixed TCF. Tirunagari & Pope (2017) visualised qualitatively local-extinction events in a series of premixed TCF using an LES method combined with a Lagrangian dynamic *sgs* model although little detailed analysis was provided.

The selected configuration is the premixed version of the Yale TCF burner. As shown in Fig. 3.1, both nozzles contain a convergent section terminated by a short straight pipe to the exit. The top flow (reactants side) is surrounded by a nitrogen co-flow with a bulk exit velocity of $2.1\mathrm{m}\cdot\mathrm{s}^{-1}$ which is not used for the bottom flow. This nozzle is identical to the nozzles applied in the study of non-premixed TCF studied by Pettit et al. (2011). The bottom nozzle is specifically designed to deliver a jet of combustion products with high temperature ended by a converging ceramic pipe with a wall thickness of 12.0 mm. The turbulence in the top stream is generated by forcing the reactants through a turbulence generating plate (TGP) enclosed inside the top nozzle. Different turbulent Reynolds numbers are achieved by varying the position of the TGP inside the nozzle, and the highest level of Re is investigated in the present work with $Re_t = 1050$. The volumetric flow rate of the reactant stream is kept constant at $1.42 \times 10^{-3}\ \mathrm{m}^3\cdot\mathrm{s}^{-1}$, while the bulk momentum of the combustion product stream is adjusted to balance the bulk momentum of the reactant stream. This allows the flame to stabilise near the mid-plane of the burner where optical access is available. The reactant flow comprises a mixture of $CH_4/O_2/N_2$ with the reactant equivalence ratio $\phi = 0.85$, while the hot product stream is generated by a stoichiometric methane flame with a temperature of 1850 K. Although the viscosity dissipation is high in the product stream due to the elevated temperature, the dynamic coupling of the opposed jets ensures that significant velocity fluctuations are present on the product side. The bulk

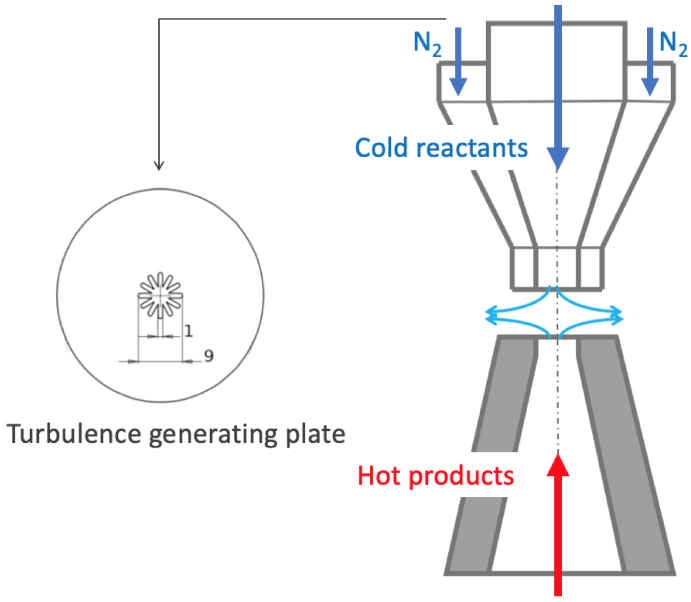

Figure 3.1: The schematic experimental configuration of the Yale TCF burner with a sketch of the turbulence generating plate.

average strain rate K_{bulk} is estimated by $2V_{bulk}/d_n$, where d_n is the nozzle separation distance and V_{bulk} is the mean bulk inlet velocity of the top nozzle kept constant as 11.2 m/s. The distance between the two nozzles is $d_n = 16$ mm that corresponds to a strain rate $K = 1,400\ s^{-1}$. These standard flow conditions for the present simulation are summarised in Table 3.1 where *onr* is oxygen to nitrogen ratio.

	Top	Bottom
Composition	$CH_4/O_2/N_2$	Hot Product
onr	30/70	26/74
$T(K)$	295	1850
ϕ	0.85	1.0

Table 3.1: Standard flow conditions.

3.3 Numerical set-up

3.3.1 Incompressible flow assumptions

In the target TCF flame where acoustic effects are neglected and the Mach number is low (i.e. $M < 0.3$ (Ferziger & Perić 2002)), the system of governing equations can be significantly simplified by introducing the incompressible flow assumptions. For subsonic combustion with low Mach numbers, the pressure can be assumed to be constant in the state equation Eq.2.14 which is replaced by $p = \rho RT = constant$. Therefore, the density is independent of pressure variation (i.e. the flow cannot be compressed) and is a function of the local temperature only. The pressure term appearing in the momentum equation e.q. 2.18 is no longer the thermodynamic pressure and is regarded as an elliptic perturbation field which acts, through continuity, only as a kinematic constraint on the velocity field In the energy equation 2.28, the pressure term $\frac{D\overline{p}}{Dt}$ in the source term can be set to zero (Poinsot & Veynante 2005).

3.3.2 Simulation parameters

The chemical kinetics mechanism employed for the oxidation of methane is the reduced mechanism purposed by Sung et al. (2001) as discussed in Section 2.3.3. Two cases, M11 and M12 with different size solution domains are studied and are illustrated schematically in Fig. 3.2 with the details listed in Table 3.2. As shown in Fig. 3.2, The M12 mesh is practically identical to the portion of mesh M11 between nozzle exits.

Case name	M11	M12
Total grid number (million)	2.89	1.47
Finest axial resolution (mm)	0.15	0.15
Finest radial resolution(mm)	0.1	0.1
Included regions	Nozzle and central domain	Central domain

Table 3.2: Mesh details and computational domains for the cases M11 and M12.

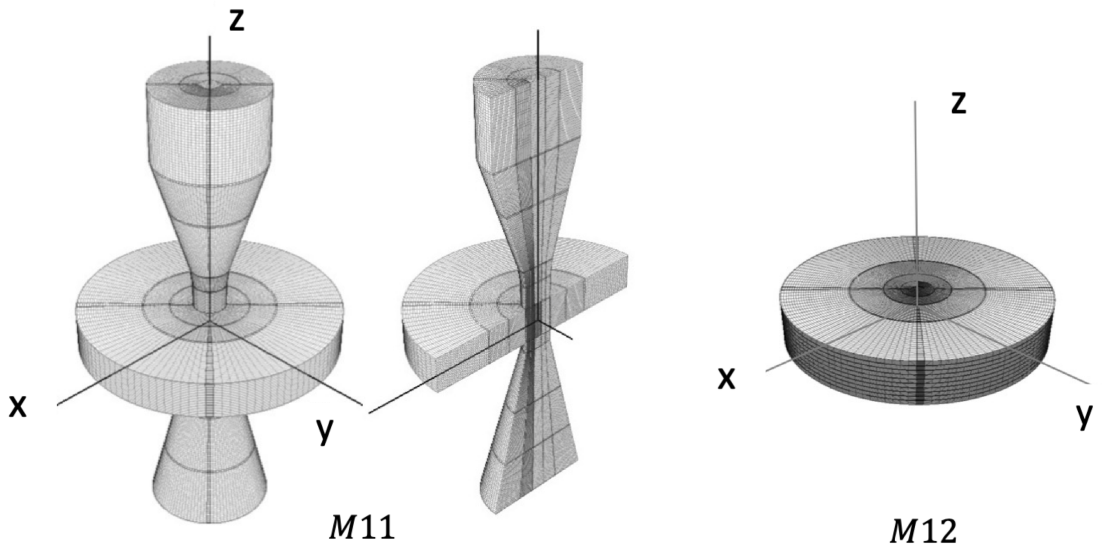

Figure 3.2: Views of the meshes for M11 and M12

The computational domain in M11 extends for 15 nozzle diameters in the axial direction (z), containing region between TGP and the inlet of the bottom duct. In the cross stream direction (x, y), both computational domains extend for 4 nozzle diameters in the region between two nozzle exits, which is aimed at reducing the influence of outlet boundary on the flow field in the regions of interest. The grid lines are gradually clustered towards the centre in both axial and radial directions where the best resolutions are achieved, and with a careful design, the grid number of M11 is limited to 2.9 million. A mesh study has been conducted and the chosen grid was shown to be sufficient to obtain mesh independent time-averaged velocity statistics.

In the present work, to reproduce the turbulence prevailing at the nozzle exits, an artificial inflow turbulence generator is applied. To prescribe meaningful fluctuations for boundary conditions, synthetic turbulence generated with the method described in Section 2.4 by di Mare et al. (2006) is applied at the inlet boundaries to re-produce the fluctuations in the flow for both M11 and M12. The synthetic inflow turbulence generator involves the specification of the turbulence levels $\overline{u'^2}$ and the corresponding integral length scales. For both cases a single estimated and constant integral length scale are used. For M11, the turbulent length scale is estimated based on the TGP orifice geometry; for M12, the mean velocities at the nozzle exit planes obtained from the M11 simulations are applied and turbulence length scale is estimated to be the radius at the nozzle. In both M11 and M12 the magnitudes of

the imposed turbulence are adjusted to give as close agreement as possible to the measured levels of root mean square (*rms*) velocity at the nozzles exits. Non-slip adiabatic boundary conditions together with the approximate near-wall, semi-log law based model of Schumann described in Chapter2.4 are applied at all solid boundaries.

The simulations were carried out with a constant time step of $\Delta t = 1 \times 10^{-6}$ s. The Courant–Friedrichs–Lewy (CFL) number is monitored instantaneously and limited below 0.25. For both cases, a convergence study is first carried out, which confirms that an initialisation time of 8 flow-through times is enough for a statistically stationary flow to develop. The time-averaged results for the flow field are collected over a period of about 6 flow-through times. The simulation was performed using ARCHER National Supercomputing Service (https://www.archer.ac.uk/). The total computational cost to perform an LES-*pdf* simulation for fully converging results is approximately 90,000 CPU-hours and 55,000 CPU-hours for M11 and M12, respectively.

3.4 Results and discussions

3.4.1 Flow field and flame topology

A non-reacting case is first established to verify the turbulent inlet boundary conditions and the applicability of the methodology, where the reactant flow is replaced by N_2 flow at the same flow rate and inlet temperature. Contour plots of the instantaneous and mean axial velocity on the central plane from downstream of the TGP to the bottom nozzle exit for M11 are shown in Fig. 3.3, together with a view of the axial velocity downstream of the TGP. From the mean velocity field in Fig. 3.3(b), the axial symmetry of the axial flow field and the counter-flowing effect can be observed. It shows the effect of feeding the gas stream through the star-shaped TGP and the development of the flow in the top nozzle. The jet breakup begins at about one diameter downstream of the TGP, with significant turbulent structures appearing in the shear layer. Due to the effect of mixing, the jet also spreads in the cross-section direction. These features are present until halfway along the converging pipe where the flow is significantly confined and becomes more homogeneous with the size of turbulent eddies

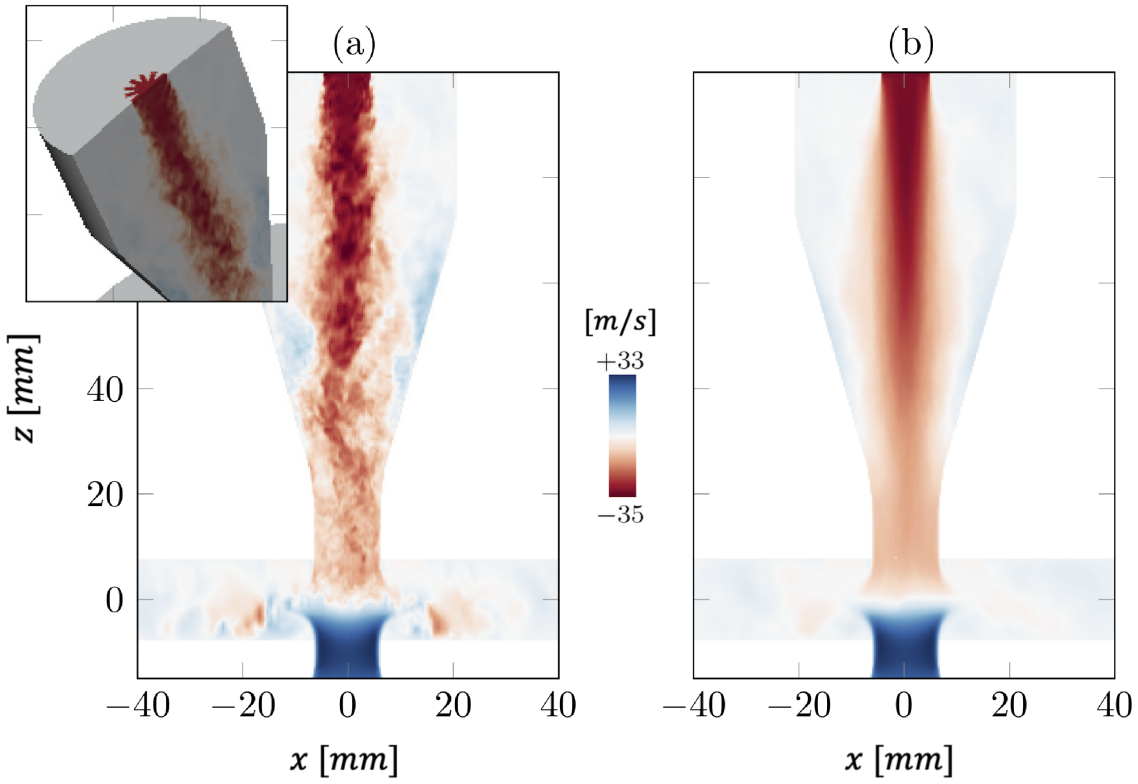

Figure 3.3: Instantaneous (left) and mean (right) axial velocity contour plot in the non-reacting case with M11, detailed on the TGP upstream of the top nozzle.

greatly reduced. In the central region, the top and the bottom jets impinge and the merged stream flows towards the atmosphere. These simulated flow field based on M11 provides insight into the flow development inside the nozzles downstream of the TGP and yields the mean velocity profiles at the nozzle exits, which are used for the smaller domain M12 simulations.

The reacting case with standard flow conditions listed in Table 3.1 are set up for M11 and M12 respectively and an example instant is presented here to illustrate the general topology of the flame. Fig. 3.4 displays snapshots of the mass fractions of CH_4, OH, temperature and Heat release rate (HRR) for M12 which provides an instantaneous visualisation of the flame. The turbulent premixed flame is identified by the region of high OH mass fraction shown in Fig. 3.4(b). When traversing from bottom to top, three regions can be detected, namely the hot product region, the flame region and reactant region. The virtual boundary separating the flame region and the hot products is referred to as the gas mixing layer interface (GMLI), and the boundary between the flame region and the reactants is the turbulent flame front, which can also be denoted by the region with the high value of

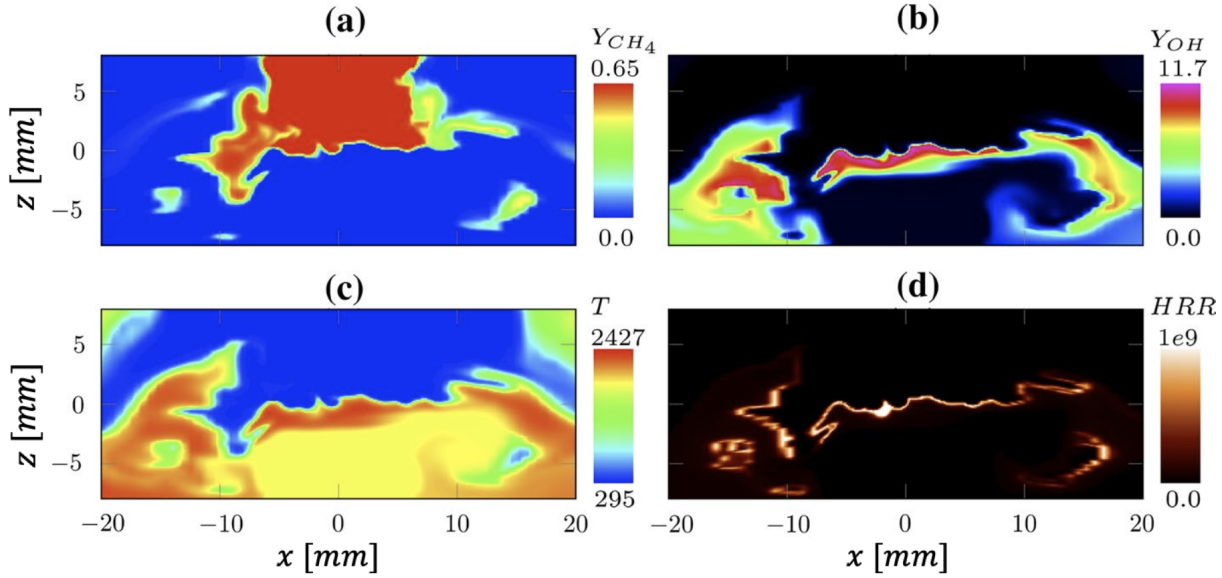

Figure 3.4: Instantaneous plots of (a) Y_{CH_4}, (b) Y_{OH}, (c) temperature and (d) HRR on a plane intersecting the solution domain along the centreline. z coordinate represents the axial direction with reactant stream on the positive half.

HRR shown in Fig. 3.4(d). Both of the GMLI and the flame front roll up in the downstream region where the flow leave the central domain laterally as an effect of the in-balance of momentum due to the upstream co-flow. In the OH snapshots, the flame is seen to be laminarised by the higher viscosity of the burned gases, while in contrast, strong fluctuations are obvious on the reactant stream side. Fig. 3.5 compares the transient heat release in the LES with M11 and M12 at various instances. It can be observed that both cases exhibit the influence of large scale turbulent motions with the flame front wrinkled and rolled up. However, the effect is much pronounced for the smaller solution domain M12 with the flame front significantly wrinkled and corrugated with 'pocket' structures and localised extinctions, almost certainly because of the higher inflow turbulence levels imposed (and consistent with the measured values) at the jet inlets for the smaller domain.

3.4.2 Conditional statistic approach

As described in Section 3.1, the GMLI together with the flame position fluctuate longitudinally. In order to analyse the local flow-field and flame-turbulence interactions, a conditional statistical approach is defined based on a relative frame of reference. A detailed description can be found in the work by

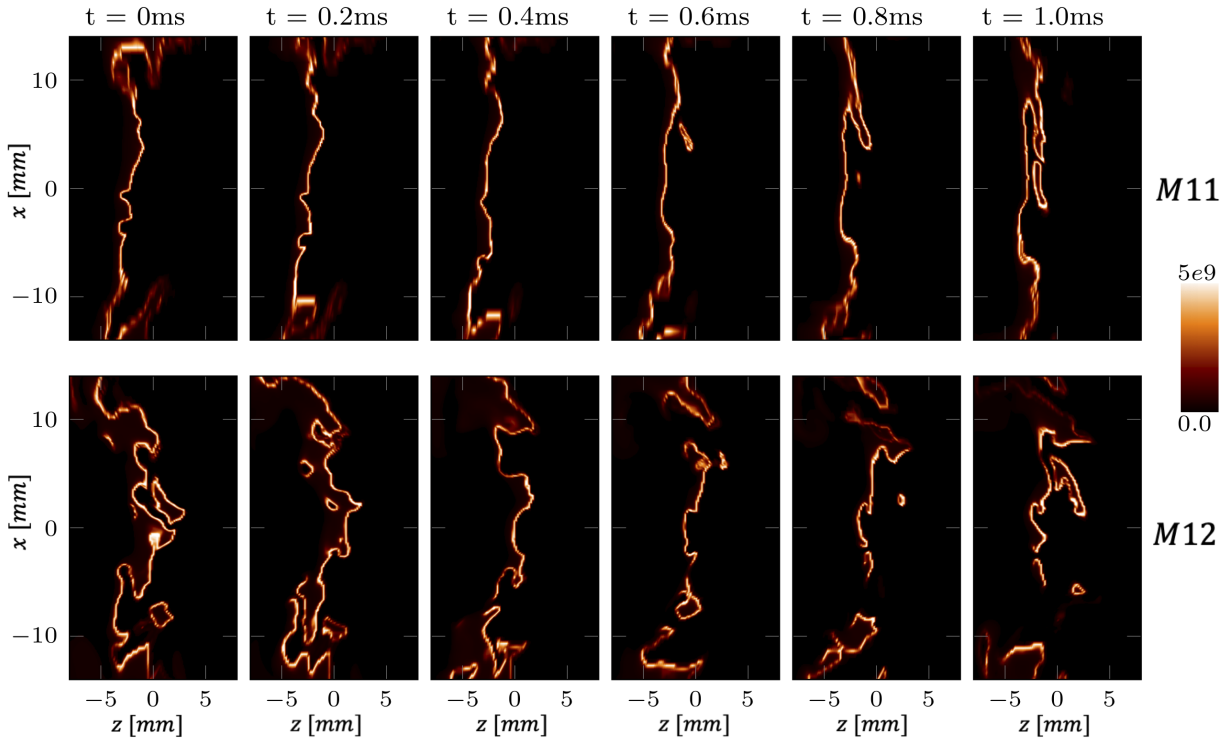

Figure 3.5: Temporal evolutions of the instantaneous HRR $[W/m^3]$ in the simulations with M11 and M12.

Coriton et al. (2013) and is briefly summarised here for the completeness of the present work.

Figure 3.6 presents an example of a fully intact flame front (a) and a local-extinction case (b). The figures on the top show the OH-PLIF field in a region between the nozzle exits, and the figures on the bottom show the corresponding profiles of OH-PLIF signal and $|\nabla(\mathrm{OH}-\mathrm{PLIF})|$ on the centreline (denoted by the green dashed lines) at the same instance. The figures are rotated such the hot product stream is on the left and the reactant stream is on the right. In both cases, the region on the left exhibits a moderate OH-PLIF signal value representing the OH content in the hot product stream. This region is hence designated as hot products. The region on the far right with OH-PLIF signal value close to zero is labelled as the reactant region. In Fig. 3.6 (a), a region with high level of OH-PLIF signals is found in between, which is caused by super-equilibrium OH concentrations produced by the flame front. This region is designated as the flame region. In Fig. 3.6 (b), along the burner centerline, the OH-PLIF signal reduces from the product stream value to the reactant stream value, indicating the flame is locally extinguished along the centreline.

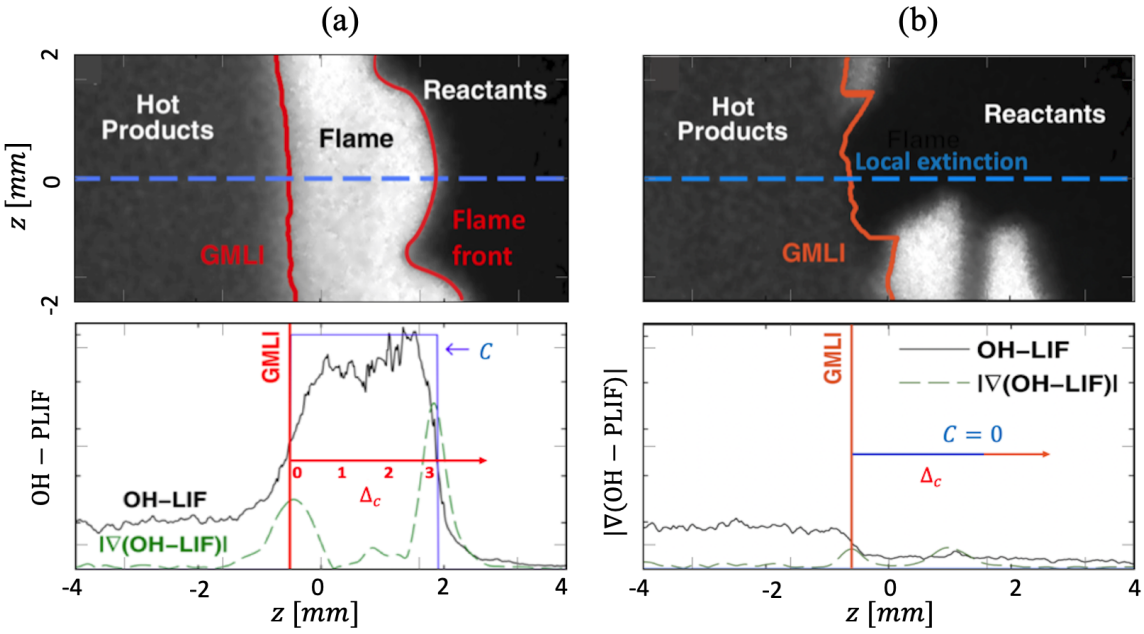

Figure 3.6: Schematic diagram of the GMLI (Coriton et al. 2013) for fully intact flame front (a) and a local-extinction case (b). Figures on the top are the sample OH-PLIF images in a region between nozzle exits. The blue dashed lines denote the burner centreline, and the red lines represent the GMLI and the flame front. The plots on the bottom are corresponding OH-PLIF and $|\nabla(\mathrm{OH}-\mathrm{PLIF})|$ signals. Plots of the progress variable c (blue lines) along the centreline under the GMLI reference frame are superimposed.

The GMLI is defined and found by the following procedure. When traversing the gradient of OH-PLIF ($|\nabla(\mathrm{OH}-\mathrm{PLIF})|$) profile along the centreline from left to right, the first peak is defined as the GMLI position. In Fig. 3.6(a), the location of the first peak is encountered when the OH-PLIF signal increases from the hot product stream to the flame region; while in Fig. 3.6(b), it occurs when OH-PLIF signal decreases from the product stream to the reactant stream. In the present study, the flame region is identified as the region to the right of the GMLI where the OH-PLIF signal exceeds a threshold value. The threshold value is 5% higher than the mean OH-PLIF signal in the hot product stream and kept constant in all the cases. If a flame is present, the flame front is determined by the locations where the OH-PLIF value exceeds the threshold value (Coriton et al. 2013). In Fig. 3.6(b), OH-PLIF signal remains below the threshold value, which is designed as a local-extinction condition. The fresh product layer thickness is hence defined as the separation between GMLI and flame front surface. When the flame is locally quenched, the GMLI and the flame front leading to the fresh product layer thickness falling to zero.

The probability of finding fresh combustion products along the centreline is quantified by the following procedure. A binary progress variable, C, is defined with a value of unity in the combustion products region (the hot product counter-flowing stream and regions of fresh combustion product) and is zero elsewhere. A local axial coordinate attached to the GMLI is then introduced, which is denoted by Δ_c. As shown in Fig. 3.6(b), Δ_c is parallel to the burner centreline with an origin coincident with the instantaneous GMLI position and increases in the direction towards the reactants stream. Under this local coordinate, the contribution to C from the counter-flowing product stream is excluded. In addition, the value of C in the burner reference frame can be affected by both localised extinctions and the variations of the position of the flame. Under Δ_c coordinate, where the fluctuations of the GMLI is filtered out, $C|\Delta_c$ is determined only by the flame topology and the flame brush thickness. The profiles of C as a function of the Δ_c coordinate are shown by the blue plots in Fig. 3.6 for both cases. When a flame is present $C|\Delta_c$ equals 1 in the region between $\Delta_c = 0$ and the flame front; in contrast when the flame is locally quenched, $C|\Delta_c$ equals 0 everywhere on the centreline, the condition shown in Fig. 3.6(b). Hence, the ensemble average of $C|\Delta_c$, $< C|\Delta_c >$, when approaching $\Delta_c = 0$ represents the probability of detecting fresh combustion products, and its complement $1 - < C|\Delta_c = 0 >$ provides the probability of local-extinction.

3.4.3 Flow field study

The flow fields are examined quantitatively in this section. We first consider the velocity field based in the fixed absolute coordinate system where it is important to remember that the unconditional *rms* velocities are affected by turbulent motions together with the large scale motions of the GMLI. These combined effects are referred to as total fluctuation in the following analysis.

Figure 3.7 compares the mean and *rms* axial and radial velocity components for M11 and M12 in the absolute coordinate system with the experimental data. The velocities are normalised by the bulk velocity of the upper stream, $V_{bulk} = 11.2$ m/s, and the locations of the upper and the bottom nozzle outlets are at y=8 mm and y=-8 mm respectively. W and U are the axial and radial mean velocities while w' and u' are the corresponding *rms* velocities. The simulated mean velocities profiles for M11 and M12 are in good agreement with the experimental data for both the axial and radial components.

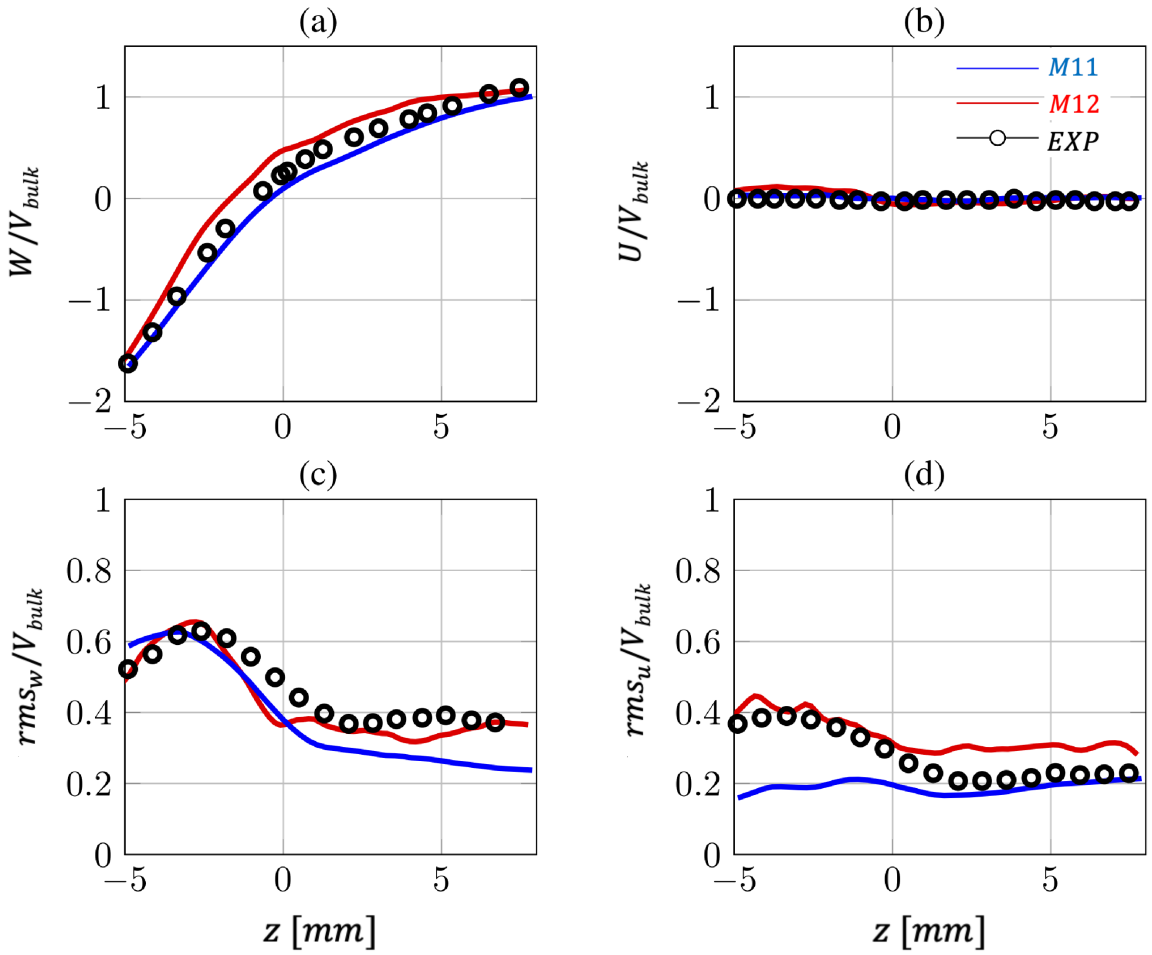

Figure 3.7: The normalised centreline profiles of the mean and *rms* axial and radial velocities compared with experimental data in the absolute frame.

In the case of the *rms* velocities, the axial *rms* velocity for M11 is under-predicted by 35% on the reactant side and the radial *rms* velocity is under predicted by around 45%. For M12, the axial *rms* velocity is well-reproduced at and in the vicinity of the nozzle exits but the under-prediction increases when approaching the central plane of the burner ($y = 0$). The largest discrepancy for the axial *rms* velocity is found around the stagnation plane ($W/V_{bulk} = 0$), where w'_{rms}/V_{bulk} is under predicted by about 25%. Since the *rms* velocity in the absolute reference frame represents the total fluctuations, this observed miss-match can not be related to specific physics, i.e. turbulent fluctuations or the GMLI location oscillations.

Hence, to filter out the effects of the GMLI fluctuations on the flow field, the conditional statistical approach described in Section 3.4.2 is employed: the velocity components are then presented in the

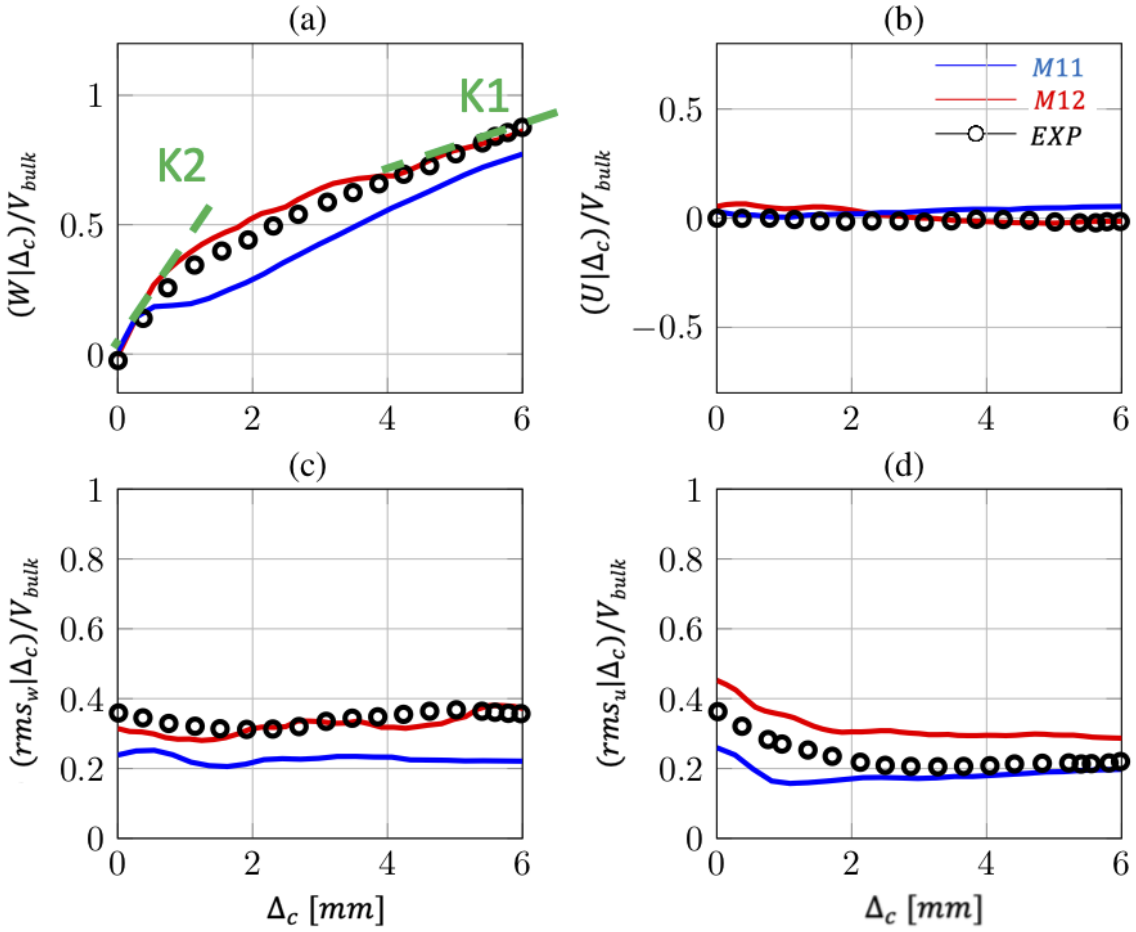

Figure 3.8: The normalised centreline profiles of the mean and *rms* axial and radial velocities in the coordinate reference to the GMLI. Δ_c coordinate represents the distance from the GMLI and increases in the direction of the top stream.

relative frame of the GMLI denoted by Δ_c. As shown in Fig. 3.8(a) and (b), the simulated conditional mean velocities for M12 are in good agreement with the measurements. At the GMLI, $(W|\Delta_c)/V_{bulk}$ (normalised conditional mean axial velocity) has a value of zero, which indicates the stagnation plane coincides the GMLI on average. The *rms* velocities for M11 are again under predicted. These discrepancies are mainly due to the low level of turbulent fluctuations at the nozzle exits in the case M11 as referred to previously. For M12 the evident good agreement with the predicted and measurements axial *rms* velocity indicates a reasonably good reproduction of the turbulent fluctuations generally. This is attributed to the better specification of synthetic turbulence at the nozzle exits, which is close to the region where these comparisons are made.

By comparing the results of M11 and M12, we conclude that with the selected turbulence generating

method, M12 better reproduces the turbulent fluctuations in the flow field of interest. In addition, this good match of *rms* in the absolute frame to the GMLI seems to suggest that the under-prediction of *rms* velocity by M12 in the absolute frame is mainly caused by the under prediction of the GMLI oscillations. This is not unexpected, as the GMLI dynamics are found to be closely linked to the details of the turbulence at the nozzle exits, which in the case of the smaller domain were supplied as boundary conditions via the digital turbulence method. Böhm et al. (2010) reported periodic fluctuations of the flow field in the top nozzle caused by vortex shedding, which is not included in M12. However whether these are associated with the jet impingement or vice-versa remains unclear. The results of M11 are not sufficient to clarify this, since simulated turbulence levels at the nozzle exit are substantially lower than observed.

In the case M11, however, it is not possible to specify realistic values of these that results in the measured values at the nozzle exit being reproduced. The turbulence generator is based on the assumption that the spectra at inlet are described by that observed in the final period of decay of isotropic turbulence. While this is unrealistic in many cases the effects are often inconsequential; the inflow turbulence interacts with mean shear, generating further turbulence which rapidly 'forgets' its origin (Tabor & Baba-Ahmadi 2010). However in the domain M11 there is no mean shear upstream of the nozzle so that the in-flowing turbulence relaxes to isotropy and dissipates over a distance comparable with the specified integral length scales. It is for this reason that the measured *rms* velocities at the nozzle exit could not be reproduced in the LES with M11.

3.4.4 Analysis of flame dynamics

Transient flame dynamics

We first examine the strain rate along the centre-line using the profiles of the conditional mean velocities. Figure 3.8 shows that, the conditional mean axial velocity decreases with a moderate slope of $K2 \sim 1100\ s^{-1}$ for Δ_c greater than 2 mm, and a larger slope of $K1 \sim 4000\ s^{-1}$ within 1 mm of the GMLI. This suggests in general that the flame experiences a much higher strain rate than the global bulk strain rate estimate of $K_{bulk} = 1400\ s^{-1}$ based on the exit velocity and the nozzle separation.

The conditional mean radial velocity is nearly zero, which is expected due to the axial symmetry of the mean flow field. In addition to the mean axial strain rate, local high velocity gradients can arise instantaneously with associated local high strain rates. To characterise the dynamics of the flame, the linkage between local-extinctions and the local resolved rate of strain field is analysed. Figure 3.9 shows the instantaneous plots of OH mass fraction and strain rate norm ||S||, captured simultaneously. These OH contours are plotted using a threshold value, which is selected to preserve the main features of the flame topology. Two continuous times series of OH mass fraction are displayed as examples, with t = 0 ms to t = 0.5 ms corresponding to a case of local-extinction and t = 1.2 ms to t = 1.9 ms corresponding to a re-ignition process. The results of M12 are used for the analysis in this section and the images are rotated 90° with the product stream on the left and reactant stream on the right.

As shown in Fig. 3.9, in the region close to the GMLI, a layer of high strain rate region can be found as a result of the jet collision, which extends towards the edge when being rolled up due to the co-flow around the top jet. At t = 0.2 ms, a pocket of reactants (denoted by a cyan circle) stretches into the reaction region at around z = 3 mm, pressing the flame front into the product stream; at t = 0.4 ms the flame front meets the GMLI and hence is locally extincted. A similar local-extinction process to that observed above can be found from t = 0.2 ms to t = 0.4 ms at around z= -3 mm with a smaller scale. The local-extinction takes place in a stochastic manner, which seems to be closely related to the local high strain rate caused by turbulent eddies with multiple scales. To further validate this, the vorticity magnitude is computed at t=0.2 ms, with four locations on the flame front (denoted by A, B C and D) selected to represent different conditions: B and C are positions where local-extinction occur, A and D are positions where flame sustain under different strain rate levels. The vorticity magnitudes at these four positions are computed to be $3,535.4\ s^{-1}$, $12,130.1\ s^{-1}$, $13,875.6\ s^{-1}$ and $7,206.5\ s^{-1}$ respectively. The vorticity in the regions of flame extinction (B, C) are almost double of that in the other regions. The above information allows an interpretation of the possible physical phenomena taking place in these turbulence/chemistry interactions: local extinction are closely related to fuel vortex breaking through the OH layer, with multiple scales random locations, which are caused by the turbulent motions in the reactant flow. This turbulence induced local-extinction process is also confirmed in the experimental work (Coriton et al. 2013), when increasing Re leading to a higher probability of finding the localised extinction along the centreline.

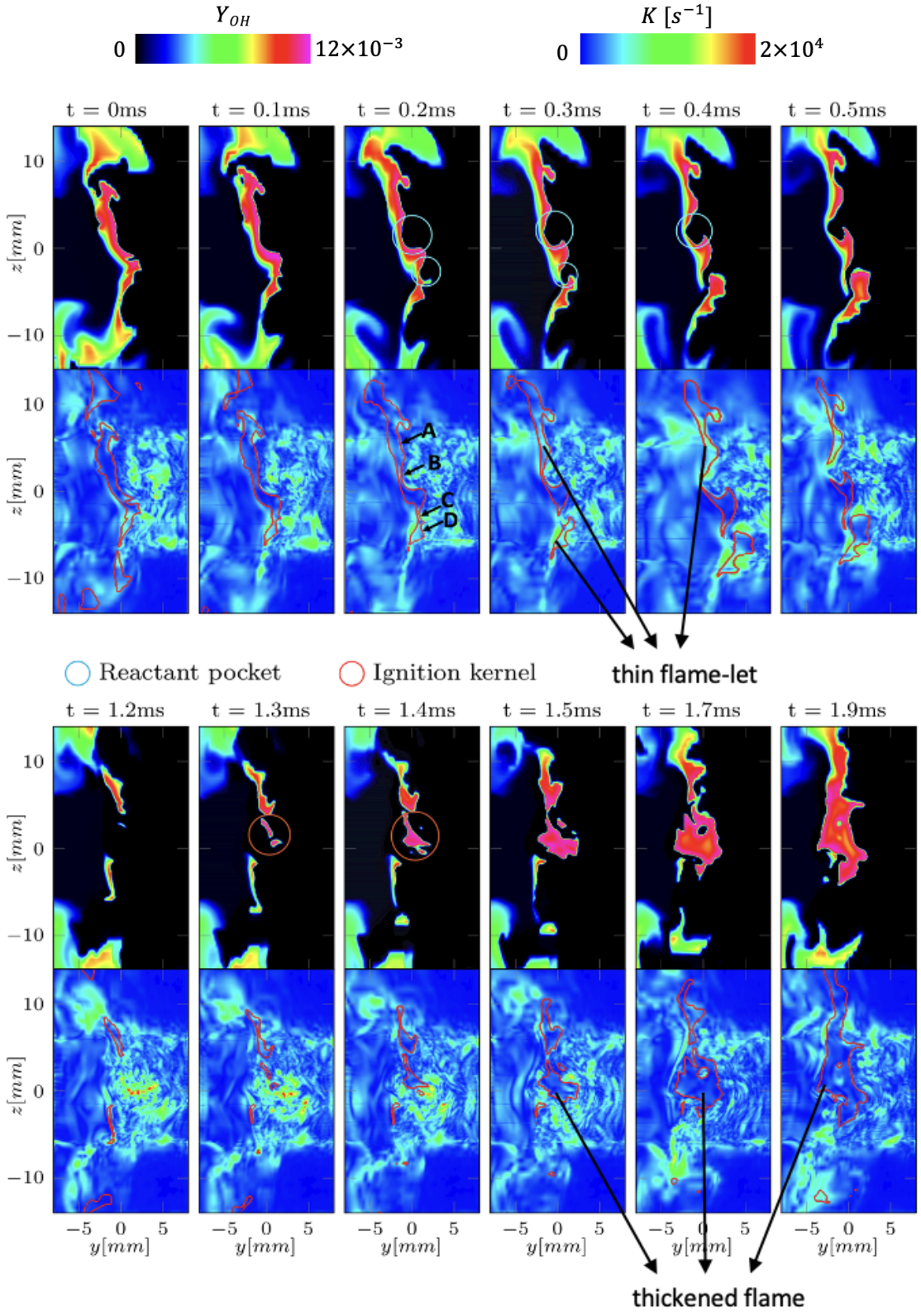

Figure 3.9: Time series of Y_{OH} and magnitude of the strain rate K on the centre plane illustrating the process of local-extinction and re-ignition in M12. The K fields have overlaid on top the contours of mean binarised Y_{OH} images in red.

In Fig. 3.9 the plots from t=1.2 ms to t=1.9 ms show a complete process of re-ignition. An ignition kernel (denoted by a red circle) first appears at $t = 1.3$ ms, which grows into burning 'islands' right away ($t = 1.4$ ms). This process takes plane in an region in the reactant stream with high local strain rates, which is again related to the turbulent motions. The flame edge and the ignited kernel propagate along the GMLI ($t = 1.4$ ms) and than connects with each other ($t = 1.5$ ms), and finally the flame is restored to an intact flame front ($t = 1.9$ ms). To summarise, the re-ignition process observed in the present case involves both turbulent transport and flame propagation. These two different scenarios for re-ignition are both observed in the experiments (Coriton et al. 2013), and have also been found in other study on turbulent flames, e.g. in a DNS study by Sripakagorn et al. (2004) on non-premixed turbulent flames, and in experimental work by Steinberg et al. (2011) where re-ignition governed by edge flame propagation and by turbulent mixing were found. Besides, it is obvious that the flame thickness at $t = 1.7 - 1.9$ ms (shown by OH contour) is much larger (≈ 5 mm) compared to the thin flame-let shown at the edge in $t = 0.4 - 0.5$, which is likely caused by small scale turbulent eddies. This is consistent with the reported Kalovitz number $Ka \sim 5$ in the experiments, which suggests a thickened wrinkled flame regime with small scale turbulent motions able to affect and thicken the flame preheat zone, while the reaction zone which remains thin (Veynante & Vervisch 2002) as shown by the HRR field. The reaction zone where heat is released has a thickness δ_r much lower than the flame zone δ_l (or thermal thickness) with $\delta_r \approx 0.1\delta_l$. As shown in Fig. 3.9, the thickened flame region is always coupled with low strain rate, while in thin flame-let region high strain rate can be found. The reason for this is that in laminar flames, the jet velocity in significantly dissipated within the reaction zone, leading to high velocity gradients and thus high strain rate, while this laminarised effect becomes less important for flames under high Re (Hult et al. 2005).

Conditional statistical analysis

To identify the frequency of the occurrence of regions of local-extinction and re-ignition, the conditional approach discussed in Section 3.4.2 is employed to analyse the statistics of the progress variable. In order to assess the influence of the *sgs* model contributions, the results of simulations with 1, 8 and 16 stochastic fields in the M12 case (denoted by M12-1, M12-8 and M12-16 respectively)

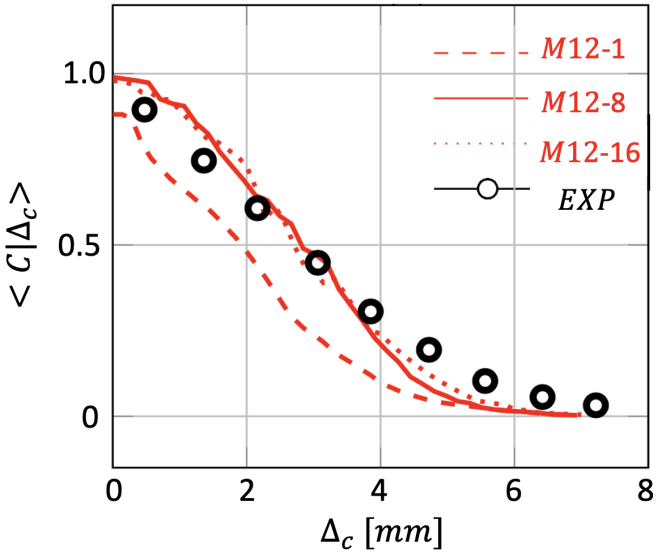

Figure 3.10: The conditional mean progress variable along the centreline for 1-field, 8-field and 16-field simulations compared with experimental measurements.

are compared in Fig. 3.10. With $N_s = 1$, the effect of *sgs* fluctuations on reaction rates are ignored, and consequently, the micro-mixing and stochastic term in Eq. 2.39 equals zero, which means no sgs chemistry models are applied. As can be found in Fig. 3.10, the conditional mean progress variable has monotonic profile with a peak at the GMLI.

Besides, it can be observed that both of the 8-field and 16-field simulations well reproduce the dynamic flame conditions measured in the experiments, with deviations found in the results with 1 stochastic field at each position in the relative frame. This suggests that the flame extinction and re-ignition dynamics under the conditions investigated is affected by the turbulence-chemistry interaction down to the *sgs* scale. However, the influence of the *sgs* combustion model is relatively small, which is somehow expected as the flame is adequately resolved with the grid (roughly 10 grids across the reaction region), and the sub-grid contribution will become limited. Comparison of the results of simulations with 8 and 16 fields shows both sets of predictions are very similar, although the 16-fields simulation gives slightly better results. This indicates that 8 stochastic fields are sufficient to represent the sgs chemistry effects for the case considered. This number has proven to be a good compromise between computational accuracy and costs in the previous study of non-premixed flame with Sandia flame D by Mustata et al. (2006) and a hydrogen jet flame by **?**, which is consistent with the findings

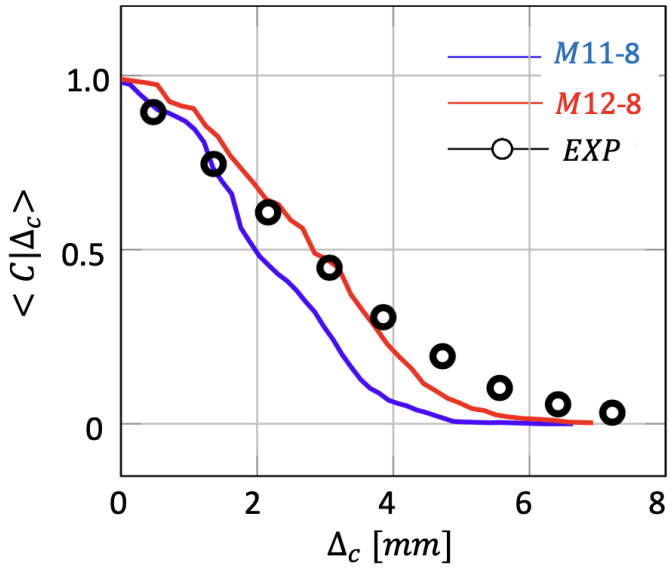

Figure 3.11: The conditional mean progress variable along the centreline for M11 and M12 simulations compared with measurements.

in the current work in the configuration of premixed TCF flames. This is probably driven by the fact, that LES resolves a large range of scales and the sub-grid *pdf* is assumed to be narrow, unlike in RANS, where the unresolved Reynolds stresses play a dominant role and thus a large number of stochastic fields is commonly used (e.g. 500 by Garmory et al. (2006)). This behavior may well be attributed to the fact that sgs fluctuations are small in an adequately resolved LES (Pitsch 2006).

Figure 3.11 compares the conditional mean progress variable in the M11 and M12 cases with 8 stochastic fields (named by M11-8 and M12-8 respectively). As presented in Fig. 3.11, both M11 and M12 reproduce the evolution of $< C|\Delta_c >$ with good accuracy, while better agreement with the measurements is found for M12. For M11, under-predictions of $< C|\Delta_c >$ are found in the regions away from the GMLI, which indicates a lower possibility of finding fresh combustion products and, in general, a thinner simulated reaction region. This is mainly due to the under-predicted turbulence levels in M11 shown by the conditional velocities fluctuations as discussed in Section3.4.3, which results in a weaker turbulent transport of the flame front.

To understand the effects of reactant-product stratification on local-extinction, the response of the flames with different reactant equivalence ratio are investigated, from $\phi_t = 0.5$ to $\phi_t = 1.0$; other flow conditions remain as the standard conditions. The profiles of $< C|\Delta_c >$ for case M12 with ϕ_t = 0.5,

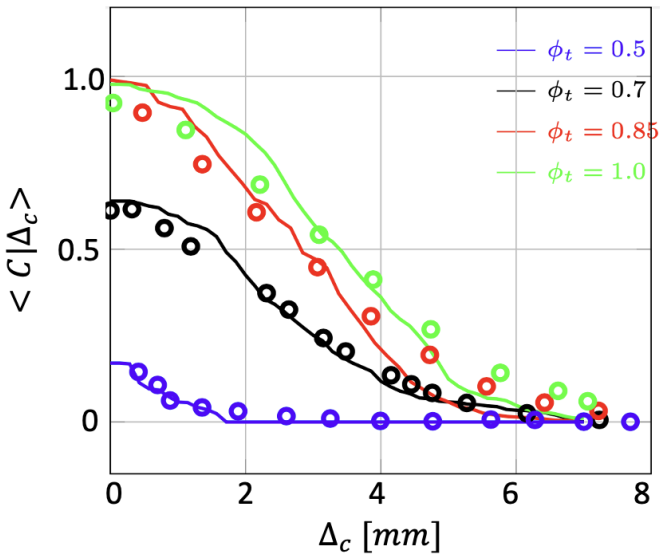

Figure 3.12: The conditional mean progress variable with various reactant equivalence ratio along the centreline for M12 simulations compared with experimental data.

0.7, 0.85*and*1.0 are displayed in Fig. 3.12. The variation of the probability of detecting fresh combustion products is well reproduced over all equivalence ratios. As ϕ_t decreases from 1.0 to 0.5, the conditional mean progress variable decreases significantly and monotonically. As discussed in Section 3.4.2, the complement of the ensemble average of the progress variable at GMLI, $1- < C|\Delta_c >$ at $\Delta_c = 0$ specifies the probability of local-extinction along the centreline. Hence, the probability of local-extinction for ϕ_t = 1.0, 0.85, 0.7 and 0.5 are about 2% 3%, 40% and 72% respectively. For the very lean case $\phi_t = 0.5$, $< C|\Delta_c >$ drops to zero after $\Delta_c = 2mm$, indicating that the flame is mostly extinguished and the turbulent flame brush thickness is less than 2mm most of the time. This is probably due to the decreased laminar burning velocities in leaner flames, and hence a smaller distance between the flame front and the GMLI, which is consistent with laminar flame calculations (Coriton et al. 2013) and is successfully reproduced here.

3.5 Conclusions

A series of premixed TCF were studied using BOFFIN-LES. The centreline profiles of the mean and *rms* velocities were well predicted with the inflow boundary condition method proposed. The

flame undergoes large scale transient motions and small scales local-extinction and re-ignition, which were well reproduced in the LES. The localised extinction processes are found to be related to the turbulent-chemistry interaction, which also plays an important role in the the re-ignition processes. Sensitivity analysis regarding the number of stochastic field showed that a relatively small number of stochastic fields are sufficient to model the *sgs* combustion effects for the case studied. The probability of localised extinction was well predicted by the LES, and the influence of the reactant mixture equivalence ratio was also successfully reproduced. Overall, the results demonstrated the capability and potential of the LES-*pdf* method in study of flame dynamics in unsteady stretched flames with strong turbulent fluctuations.

Chapter 4

Compressible Code Validation: Noise Generation in a Non-isentropic Subsonic Nozzle

In this chapter, an LES study on the noise generation in an Entropy Wave Generator (EWG) is presented. The disturbances are created by cross-flow pulse injections of a secondary gas with a different composition; the indirect noise is generated via a non-isotropic nozzle. The experiments are designed to feature two configurations with different injection positions, which enables the separation of direct and indirect noises. The specific objective of the present work is to evaluate the compressible LES code BOFFIN-LES in predicting acoustic amplitudes in a resonator terminated with a contraction part, which represents the typical structure in many industrial burners. In addition, different injecting positions, main jet mass flow rates and injection gases with various molar mass are studied to investigate the noise generation and propagation problem in the system.

4.1 Background and motivations

Combustion noise is a potential major contributor to aircraft engine and gas turbine noise, which has become an increasingly important topic over the last several decades (Dowling & Mahmoudi 2015). There are two main categories of combustion noise: direct and indirect combustion noise. Direct noise is caused by volumetric expansion and contraction due to unsteady heat released by unsteady combustion. The unsteady heat release rate is also accompanied by temperature, compositional and vortical perturbations, which if accelerated can eventually generate acoustic noise, known as the indirect noise (Howe 2010). In real engines, indirect noise is generated at the contracted chamber outlet or the first stage of the turbine, and propagates both downstream and upstream back into the combustor. Those travelling back can contribute to the triggering of thermo-acoustic instability in the combustion chamber (Morgans & Duran 2016) and may lead to significant damage to the combustor structure and even engine failure (Poinsot 2017).

Entropy indirect noise caused by temperature perturbations has been a topic for analytical study for over 50 years. Marble & Candel (1977) developed one-dimensional transfer functions for the noise generated via an isentropic compact nozzle for different conditions, which laid a foundation for further work on indirect noise generation. The theory was further extended to include a wider range of conditions and various low-order models have been proposed, e.g. by Goh & Morgans (2011) and Christodoulou et al. (2020). The generation of indirect noise by compositional inhomogeneities was first identified by Magri et al. (2016) and Ihme (2017) with transfer functions developed under compact nozzle assumptions. Magri (2017) further extended the work to include non-compact nozzles under subsonic and supersonic conditions. Giusti et al. (2018) investigated the relative contributions of compositional and entropic noise in a realistic rich-quench-lean combustor, where it was found that the compositional noise was not negligible and was expected to become louder in supersonic nozzles.

Following the above analytical efforts, several model experiments have been devised to investigate the generation of entropic and compositional noises. In German Aerospace Centre (DLR), an Entropy Wave Generator (EWG) was set up using a heating grid and convergent-divergent nozzle to generate entropic noise and the pressure signal was measured for both subsonic and supersonic regimes

(Bake et al. 2009). Recently in Cambridge University, an EWG rig has been set up to investigate indirect noises caused by entropic and compositional inhomogeneities (di Domenico et al. 2017, Rolland et al. 2018). The pressure signal upstream of the nozzle was recorded with various designs, successfully separating and identifying the direct and indirect noise. This work was further extended by (di Domenico et al. 2021) to account for the effect of non-isentropicity on the noise generation by compositional disturbances. Noise generation has been studied in the DLR EWG by Leyko et al. (2011) and Duran et al. (2013) and the Cambridge EWG by di Domenico et al. (2017), Rolland et al. (2018), di Domenico et al. (2021) using one dimensional analysis with different models proposed for indirect noise generation. A further step is to take account of the non-uniform distribution of entropic and compositional waves and the dispersion and convection of these waves inside the system: high accuracy simulations, which provides a three-dimensional description of the flow and turbulence, is a natural means whereby this can be achieved.

Morgans et al. (2013) performed incompressible DNS on a combustor channel flow to investigate the effect of flow advection of entropy waves, where dissipation effects were found to be negligible and that dispersion may not be sufficiently fast. Hence significant entropy wave strength remained at the combustor exit. Giusti et al. (2017) applied incompressible LES to study entropy waves and found that the waves decayed as a function of a local Helmholtz number based on the wavelength and axial distance. Moreau et al. (2017) performed compressible LES of the DLR EWG configuration, successfully reproducing the measured pressure signals and confirmed that the amplitude and shape of the entropy spot (temperature fluctuation caused by the heating device) was distorted especially when convected over a long distance in the downstream duct. Rodrigues et al. (2020) utilised URANS (unsteady RANS) to investigate the details of entropic and compositional waves generated by thermal and compositional perturbations in an open-end pipe without noise generation. The specific objectives of the present work are to evaluate the predictive capability of BOFFIN-LES in predicting the acoustic fluctuations with proposed boundary conditions in a resonator terminated with the contraction part, which represents the typical structure of many industrial burners. For this purposes, the noises generated by compositional perturbations in the Cambridge EWG with a non-isentropic subsonic nozzle are investigated. It appears that there have been only limited existing literature on numerical studies of the compositional noise and the present work will add to it. Compressible LES has been performed

on the 360° EWG configuration using BOFFIN-LES. Different injecting positions, main jet mass flow rates and injection gases corresponding to the experiments, are investigated with the underlying physics discussed in detail.

4.2 Case description

4.2.1 Experimental set-up

The target experiments of the present work are a series of test cases conducted with the Cambridge University EGW rig. The experimental configuration is shown schematically in Fig. 4.1(a) with the key dimensions summarised in Table 4.1. A flow of air with a controlled mass flow rate is fed into the duct through the inlet on the left of the duct upstream of the nozzle. A pulse of secondary flow is injected perpendicular to the main air flow. The primary airflow is supplied through a long flexible hose, attached via a flat flange to provide a simple acoustic boundary condition. The upstream duct consists of a steel tube with 42.6 mm inner diameter and a length of 1.65 m. A flexible plastic duct is placed downstream of the nozzle, which features the same inner diameter as the upstream tube and a length of 61 m, hence dumps the acoustic fluctuations and creat anechoic boundary at the outlet. The 'round-trip' time for the downstream duct is $2L_2/c \sim 350$ ms, where c represents the speed of sound. Hence for t < 350 ms, downstream acoustic reflections will not have any effect on the acoustic pressure (di Domenico et al. 2021). In contrast, the inlet boundary has a high reflection coefficient $R_i \sim 0.99$ (Rolland et al. 2018), which is effectively a highly reflective boundary for acoustic waves.

	L_1	L_2	D	D_{th}	L_p	L_c
length (m)	1.65	61	0.0426	0.0066	0.75	0.65 *or* 0.05

Table 4.1: Dimensions for the experimental configuration.

The convergent nozzle is 24*mm* long featuring a linear geometry profile and a throat diameter of 6.6*mm*, followed by the straight downstream pipe. Thus, the flow experiences an abrupt divergence downstream of the converging section, along with flow separations and large losses. Hence this convergent nozzle terminated with a straight pipe works in a way similar to an orifice plate. A series

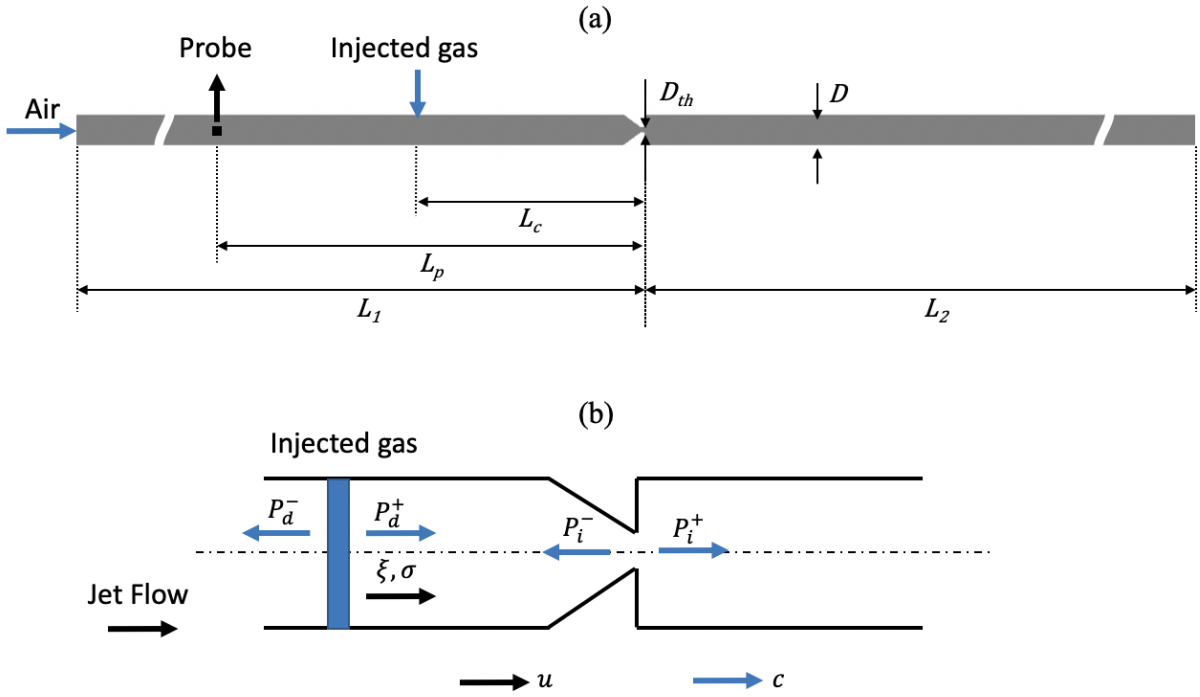

Figure 4.1: (a) A simplified layout of the experimental configuration. Specific dimensions are listed in Table 4.1. (b) A schematic diagram of the mechanism of the noises and waves generation and propagation in the system. Acoustics noise, compositional wave and entropic wave are denoted by P, ξ and κ respectively. The subscript d and i represent direct and indirect noises, and the superscript $+$ and $-$ represent the propagation directions of the acoustic waves respectively. The blues arrows represent the acoustic waves propagating at the speed of sound c, and the black arrows denote the jet flow rate at which the compositional and entropic waves travel downstream.

of measurements were carried out at eleven different air mass flow rates $\dot{m}_a$, and three of these, where the flow in the convergent nozzle is under subsonic conditions, are studied in the present work. The details of test cases considered are presented in Table 4.2. Corresponding to the experiment by di Domenico et al. (2021) the injected gas mass flow rates provide a fixed mass fraction of the gas ($Y_{He} = 0.02$ and $Y_{CO_2} = 0.2$) and a similar molar fraction for all cases ($X_{He} \sim X_{CO_2} \sim 0.14$).

4.2.2 Pulse injection and noise generation

Pulses of a secondary flow are injected along the cross-stream direction to generate species composition perturbations. Various injected gases are studied, including helium, argon, carbon dioxide and methane with each having a different density. Each pulse lasts for τ_p = 100 ms with a 0.25 Hz repeti-

tion rate, corresponding to a 4 s period. The mechanism of noise generation in the configuration can be simplified by using a quasi-one-dimensional framework as discussed in di Domenico et al. (2021), which is briefly introduced below for the completeness of the present work As shown in Fig. 5.1(b), the gas injection has three major effects in terms of the flow fluctuations: first, the injection leads to perturbations in the mass, momentum, energy and mixture fraction fluxes, generating direct pressure fluctuations which are referred to as direct noise, denoted by P_d (where P represents pressure); these perturbations also causes entropic fluctuations κ and additionally, compositional fluctuations are caused by the addition of the compositional flux, denoted by ξ. The flow variables can be decomposed into mean and fluctuating values such as $Y_i = \bar{Y}_i + Y_i'$. In the linear limit when $Y_i' << \bar{Y}_i$, these disturbances do not interact (Chu & Kovásznay 1958) and can be treated as waves with amplitudes related to relative flow variable fluctuations:

$$P^{\pm} = \frac{1}{2}\left(\frac{p'}{\bar{\gamma}\bar{p}} \pm \frac{u'}{\bar{c}}\right), \quad \kappa = \frac{s'}{\bar{c}_p} = \frac{p'}{\bar{\gamma}p} - \frac{\rho'}{\bar{\rho}} - \bar{\Psi}Z', \quad \xi = Z' \tag{4.1}$$

where γ, u, c, s, c_p, Z and Ψ represent the specific heat capacity ratio, velocity, speed of sound, entropy, heat capacity, mixture fraction and chemical potential function respectively (Magri et al. 2016). Direct noise travels both upstream ${P_d}^+$ and downstream ${P_d}^-$ at the speed $c-u$ and $c+u$ respectively, approximately equal to the speed of sound c. The entropic and compositional inhomogeneities are convected with the flow downstream towards the nozzle. Once these inhomogeneities are accelerated by the nozzle, indirect noise is generated and propagates both upstream ${P_i}^+$ and downstream ${P_i}^-$. The convective distance L_c represents the distance between the injector and the nozzle and varies with the injection location, with correspondingly different convective time delays $\tau_c = L_c/u$, where u represents the bulk flow speed. Two configurations, based on the injection location are created, namely a long configuration where the injected gas location corresponds to L_c = 0.65 m upstream of the nozzle and a short configuration with L_c = 0.05 m. In the former case a separation, τ_c between the direct and indirect noise arises whereas in the latter the direct and indirect noise are almost coincident. By comparing the results of both configurations the direct and indirect noise contributions can be identified and evaluated, which will be discussed in detail in Section 4.4.2.

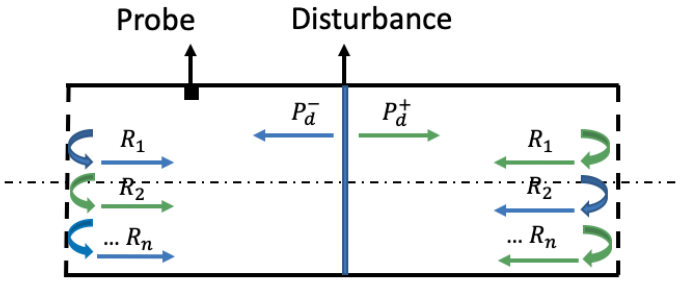

Figure 4.2: Schematic of reverberation processes in a straight pipe with a direct acoustic noise. The blue arrows represent the direct noise traveling backward and its reflections; the green arrows denote the forward traveling one and its reflections.

4.2.3 Reverberation

When an acoustic signal is reflected in an acoustic chamber repeatedly over a very short period of time, the measured acoustic pressure is effectively an ensemble of the original and all the reflected noises (Rolland et al. 2018). Fig. 4.2 shows the reflections of the direct noises in the upstream pipe schematically. The direct noise propagate in both backward and forward; for the backward travelling wave, once it reaches the upstream boundary, it reflects back towards the downstream boundary (nozzle in the EWG rig) where it will reflect once again etc. The forward traveling direct noise experiences a similar process except for it first reflects at the downstream boundary. The upstream probe detects all the pressure waves traveling pass it, including the original acoustic waves and the reflected waves; if the time for the reflected acoustic waves to travel back to the probe is smaller than the acoustic pulse, the successive reflected waves are superimposed with the direct noises being generated, and the probe measured an 'amplified' acoustic signals. In the present work, the acoustic 'round trip' time in the upstream pipe is $\tau_{round} = 2L_1/\bar{c} = 2 \times 1.65/340 \sim 0.01$ s. During the injection process, the sound wave in the upstream pipe reflects about $2\tau_p/\tau_{round} \sim 20$ times between the inlet and nozzle, which results in reverberation. The amplitude of the waves reduce after every reflection since the reflections are imperfect which causes the lost of the acoustic energy.

To summarise, to successfully predict the measured acoustic pressure signals, the LES work should be capable of well predicting the amplitude of the acoustic source and successfully capture the reverberation effect in the system . It is worth noting that in the EWG configuration, the nozzle is a second

acoustic source where the indirect noise is generated, which also has reverberations in the upstream pipe.

4.3 Numerical set-up

The present work aims at investigating the effects of different gas injection locations, various air mass flow rates and injected gases with different molar mass on the noise generations. Helium and carbon dioxide are selected to represent gases lighter and heavier than air respectively. This leads to eight test cases B1-B8, with details summarised in Table 4.2. All the simulations are carried out with constant time steps, with the CFL number limited below 0.25 and details can be found in the last column. In the case B1 and B3, with the highest primary mass flow rate $\dot{m} = 8\ gs^{-1}$, the Reynolds number is about 6,500 which lies within the Reynolds number range where laminar to turbulent transition may occur (Draad et al. 1998). The current simulations suggest that the flow is basically in the laminar regime accompanied by some turbulent structures

Case	Gas	$\dot{m}(gs^{-1})$	$\dot{m}_g(gs^{-1})$	$L_c(m)$	$\Delta_t(\times 10^{-7}s)$
B1	He	8.0	0.17	0.65	5
B2	He	8.0	0.17	0.05	5
B3	CO_2	8.0	1.62	0.65	5
B4	CO_2	8.0	1.62	0.05	5
B5	He	1.0	0.02	0.65	30
B6	He	1.0	0.02	0.05	30
B7	He	4.0	0.08	0.65	10
B8	He	4.0	0.08	0.05	10

Table 4.2: Numerical conditions for test cases B1-B8: primary mass flow rate $\dot{m}$, injected mass flow rate $\dot{m}_g$, convective distance L_c and time step Δ_t.

4.3.1 Boundary conditions and grids

The computational domain covers the upstream pipe, nozzle and part of the downstream pipe which is discretised with structured, multi-blocked meshes contains about 0.5 million grids. A view of

the computational mesh is shown in Fig. 4.3. The grids are smoothly clustered towards the nozzle and throat regions where the minimum mesh spacing exists. The minimum gird sizes are about 0.5 mm and 0.25 mm in the axial direction ($\delta^a{}_{min}$) and the radial direction ($\delta^r{}_{min}$) respectively. Before applying the unsteady injection, a mesh study has been conducted and the chosen grid was shown to be sufficient to obtain mesh independent time-averaged velocity statistics. Main flow parameters representing the operating conditions are then computed and compared with the experimental measurements for B1, B5 and B7 case, including the throat Mach number M_{th} upstream Mach number M_1 and the mean upstream pressure $\bar{p}_1$, as shown in Table 4.3. It can be seen that with the selected mesh

Case		$\dot{m}(gs^{-1})$	$\bar{p}_1(kPa)$	M_{th}	$M_1(\times 10^{-3})$
B1	EXP	8.0	125.4	0.686	11.05
	LES	8.0	129.3	0.676	12.8
B5	EXP	4.0	107.3	0.327	6.43
	LES	4.0	106.9	0.308	7.02
B7	EXP	1.0	101.7	0.081	1.70
	LES	1.0	100.3	0.088	2.20

Table 4.3: Key conditions for the selected cases.

resolution, the mean upstream pressure and Mach number at the upstream probe and the upstream pressure are reproduced with satisfactory accuracy in the LES for all three cases. The maximum grid size in the axial direction is about 10 mm, while the wavelengths of interest lie in the range 1 to 4 m and the corresponding time scale range is 0.003 to 0.01 s which nearly three orders of magnitude larger then the time steps as shown in Table 4.2. Hence the waves of interest are well resolved both in space and time.

In addition to the resolution of the mesh, the length of the computational domain is also of great importance in the current study of acoustic problems. As discussed in Section4.2.1, the length of the upstream and downstream pipe are 1.65 m and 61 m respectively, and it is impractical to include the entire geometry of the test rig in the simulation given this length. The selection of the computational domain (or in other words, the reduction of the domain) should be considered together with a proper choice of the boundary conditions. As for the inlet boundary, fully reflective inlet boundary conditions are imposed at the inlet of the pipe to match the actual impedance in the experiments discussed in

Section 4.2.1; the full length of the upstream pipe is kept, which is found to be necessary to accurately capture the reverberation effect. In a separate study, with a reduced upstream pipe length, both of the direct and indirect noise amplitudes are significantly over-predicted. For the outlet boundary, given its anechoic nature, non-reflective outlet boundary conditions are adopted at the downstream pipe exit, together with a reduced pipe length for cost consideration. Non-slip adiabatic boundary conditions together with the approximate near-wall, semi-log law based model of Schumann described in Chapter2.4 are applied at all solid boundaries.

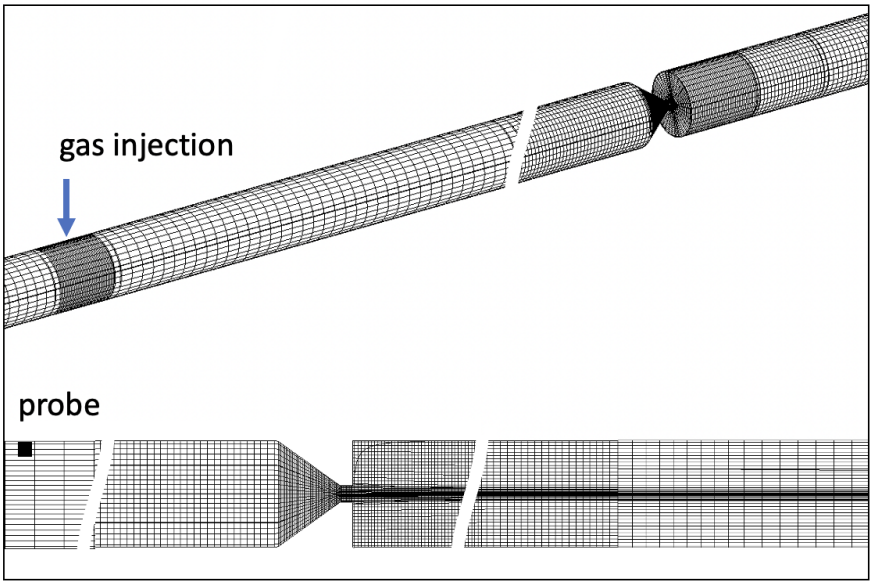

Figure 4.3: A view of the computational mesh with a slice in a mid-plane.

4.3.2 Simulation parameters

In order to investigate the noise generation and acoustic features, compressible LES with BOFFIN-LES on the the Cambridge EWG configuration is performed. The governing equations and modeling strategies are given in Section 2.2 and 2.3. The source term in Eq. 2.39 is neglected since there are no chemical reaction taking place. As discussed in Section 2.5, the convection terms in the momentum equations are approximated by a second order central difference scheme and as such there is negligible numerical dissipation – at least on a uniform mesh. As shown in section 4.2.2, the injection encompasses 100 ms and takes place every 4 seconds. In the simulations, each case is

initialised for one cycle of 4 seconds after which the data is collected and time-averaged. Phase and time averageing are carried out over two cycles. For each cycle it was found that after 0.8 seconds the pressure level settles to the background level and remains the case until the end of the cycle. Hence, in the simulations the injection period was reduced to 1 second after initialisation as a compromise between reliable results and computational costs. The computational cost to perform an compressible LES simulation for one cycle (1 s) is approximately 50,000 CPU-hours on the Isambard GW4 Tier2 HPC Service (https://gw4.ac.uk/isambard/).

4.4 Results and discussions

4.4.1 Flow field of the reference case

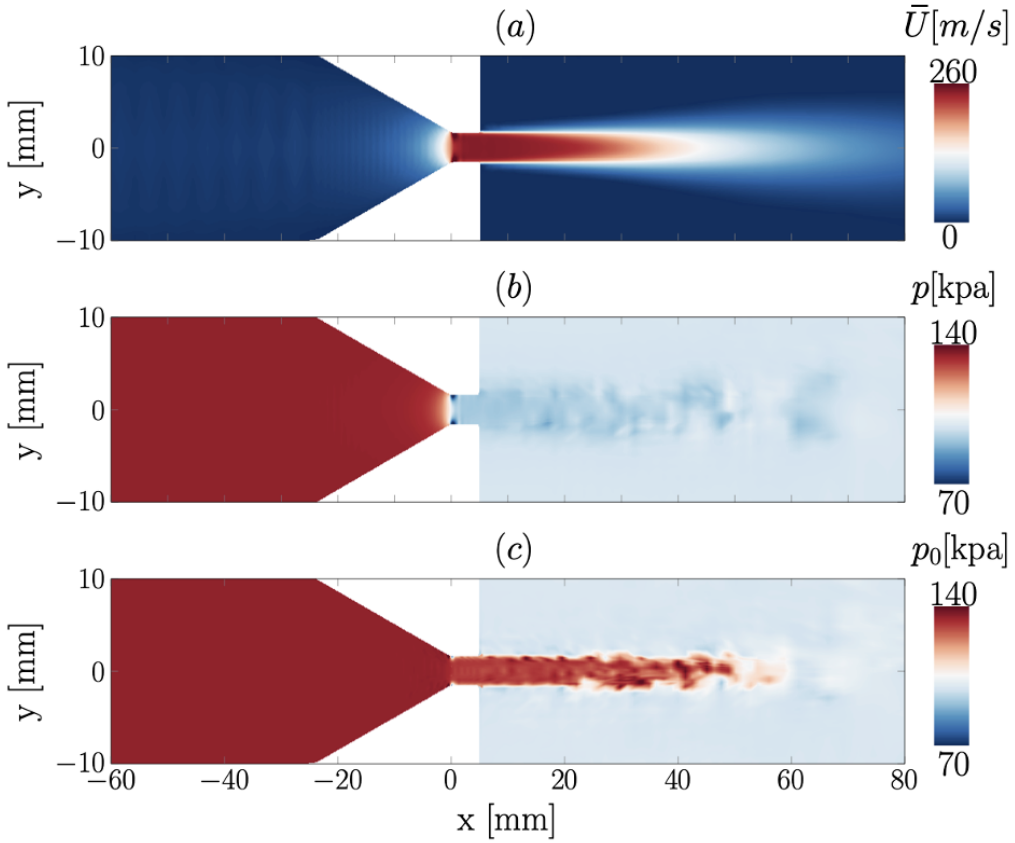

Figure 4.4: Sliced colour plots of (a) mean axial velocity $\bar{U}$, (b) pressure p and (c) total pressure p_0 in the the region of the nozzle.

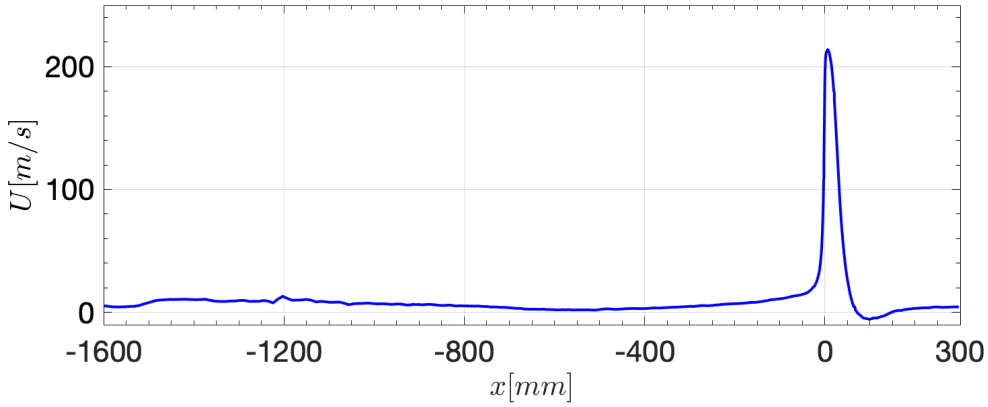

Figure 4.5: Mean axial velocities computed from the LES along the pipe centreline.

A flow without radial injection was set up first for each case to initialise the flow field. Hereby, the flow condition in B1 is selected as a reference case with the highest mass flow rate.

Fig. 4.4(a) shows a snapshots of mean axial velocity U, pressure p and total pressure p_0 though a slice across the centreline in the nozzle region. The flow is accelerated through the nozzle with the highest velocity U occurring at the throat, followed by a 'jet' like flow into the downstream pipe. The U profile along the pipe centreline is further shown in Fig. 4.5, which quantify the high velocity gradient in the region near the throat. Fig. 4.4(b) shows that the static pressure is almost constant in the upstream pipe and in the nozzle, which reduces rapidly as the throat is approached to its lowest value and then gradually increases to the downstream ambient pressure. Vortex shedding can be found in the downstream jet region, with high pressure and lower pressure region can be detected alternately. Fig. 4.4(c) shows the total pressure which has a constant value upstream and with a slight reduction in the nozzle and throat, implying that the flow is almost isentropic in this region. This is not the case when the flow exits the nozzle, where a sudden expansion occurs and the 'jet' flow becomes turbulent. Hence there is a large loss, shown in Fig. 4.4(c) with a lower total pressure at the nozzle exit, which gradually falls during the mixing with slower moving fluid until no obvious difference can be seen with the surrounding flow.

The injection of the secondary gas in the cross flow direction is then triggered. Figure 4.6 shows the evolution of the helium mass fraction snapshots for case B1 from t = 5 ms to t = 300 ms where the injection period extends from t = 0 ms to t = 100 ms. The helium flow enters the pipe at around t

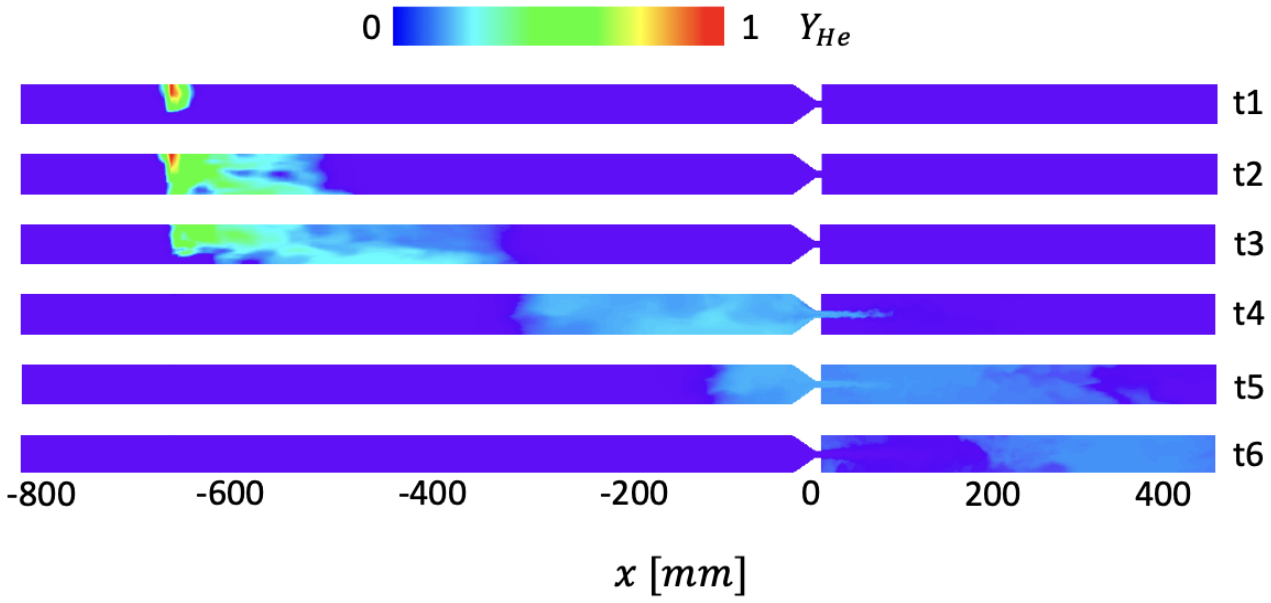

Figure 4.6: Temporal evolution of helium mass fraction in B1 on slice across the pipe centreline at t1 = 5 ms, t2 = 50 ms, t3 = 105 ms, t4 = 165 ms, t5 = 250 ms and t6 = 300 ms.

= 5 ms in the cross-flow direction and then mixes with the main air flow both in the radial and axial direction, after which it is convected downstream towards the nozzle by the main axial flow. At t = 165 ms, the helium reaches the nozzle, which gives rise to indirect noise generation as the helium wave is accelerated in the nozzle. This will be discussed later together with the temporal acoustic noise signal in the following section.

4.4.2 Long pipe configuration

The evolution of pressure fluctuations in the long configuration ($L_c = 650$ mm) is compared with the experimental measurements, shown in Fig. 4.7. The pressure fluctuation p' is normalised by the product of the specific capacity ratio $\bar{\gamma}$ and the mean pressure $\bar{p}$. Figure 4.7(a) and (b) show the upstream pressure signals in B1 and B3 with helium and carbon dioxide injected respectively. The blue lines represent the LES results while the black solid lines represent the experimental measurements. The red dashed lines are the exponential decay fit of the acoustic energy loss predicted by the reverberation model proposed by Rolland et al. (2017).

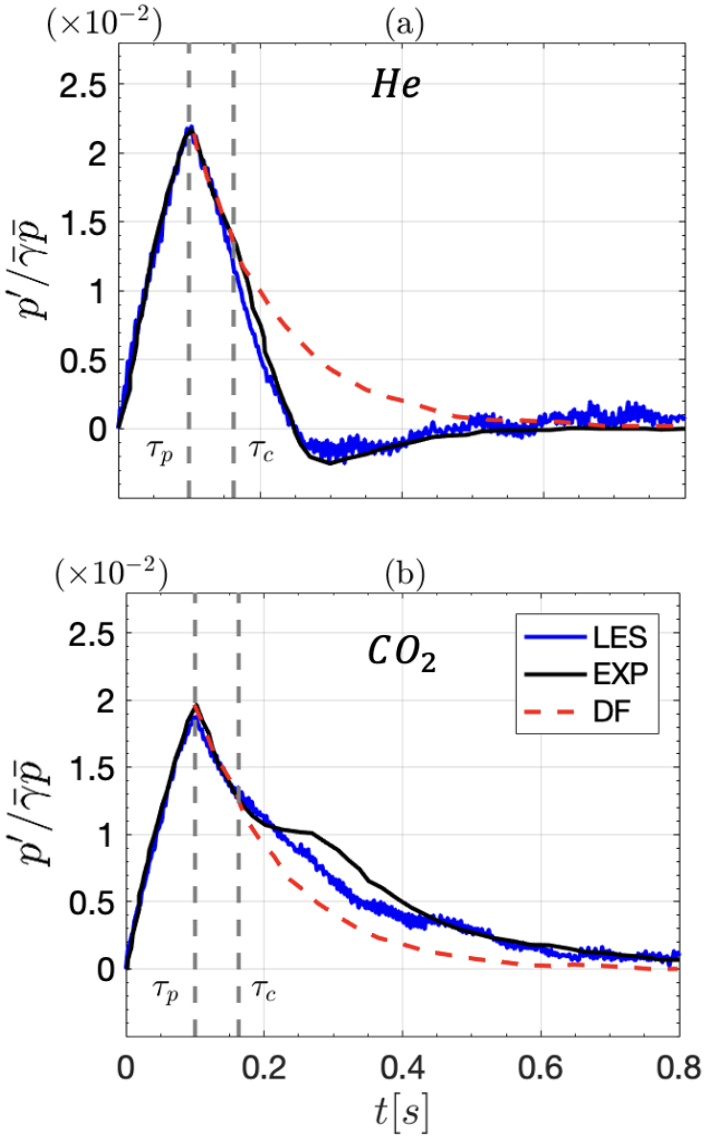

Figure 4.7: Phase averaged, normalised acoustic pressure fluctuations in the long pipe configuration at the pressure probe. (a) B1 with He injection and and (b) B3 with CO_2 injection. Two vertical dashed lines mark the end of the injection duration τ_p and the convective time of the compositional waves $\tau_c \sim 163ms$.

The pulse injection lasts for 100 ms and ends at $t = \tau_p$, during which time the acoustic p' rises rapidly and reaches a maximum at $t = \tau_p$. This corresponds to the acoustic waves generated as a direct result of the gas injection together with the reverberation effects. After reaching the maximum value, the pressure signal begins to fall due to the loss of acoustic energy. Both the measured and simulated p' decay exponentially and follow the decay fit line up to $t = \tau_c \sim 163$ ms, when the injected gas reaches the nozzle, as shown in Fig.4.6 at $t = 165$ ms. At $t = \tau_c$, the injected gas reaches the nozzle where it is accelerated, generating indirect noise which propagates upstream towards the probe (P_i^-, Fig. 4.1). Hence, p' begins to deviate from the decay fit curve in both in the measurements and LES. In the case B1, the indirect noise is negative while in B3 it is positive, which is due to the relative higher excess densities of helium with respect to air and lower excess density of carbon dioxide with respect to air. The indirect noise reaches a maximum at around $t = 0.26$ s, which is close to the time where the compositional wave is fully convected through the nozzle. This is supported by the fact that $t = 0.27$ s is very close to the summation of pulse injection time and convective delay $\tau_c + \tau_p \sim 0.263$ s. On comparison of the measurements and LES p' profiles up to $t = 0.16$ s, it can be observed that the peak amplitudes, arrival times and the shapes of the p' signal are well reproduced by the LES, suggesting strongly that the time histories of the compositional disturbance source are well defined and the acoustic boundary conditions are determined appropriately. In the case of the indirect noise, both the measurements and LES p' begin to deviate from the theoretical decay model at around $t = 165$ ms with the time of the indirect noise generation being well reproduced by the LES, implying that the bulk convective velocities are accurately computed. The amplitude of the indirect noise is slightly under-predicted in both case, which is more obvious in B3 and will be discussed together with results in the short pipe configuration in the following section.

4.4.3 Short pipe configuration

In the short pipe configuration, the cross-stream gas is injected very close, at 50 mm, to the nozzle corresponding to a convective time delay of the compositional and entropic wave of $t = \tau_c \sim 0.001 - 0.01$ s, which is very short compared with the pulse duration $t = \tau_p = 0.1$ s. This suggests the direct noise and indirect noise are generated almost simultaneously. In contrast to the long configuration

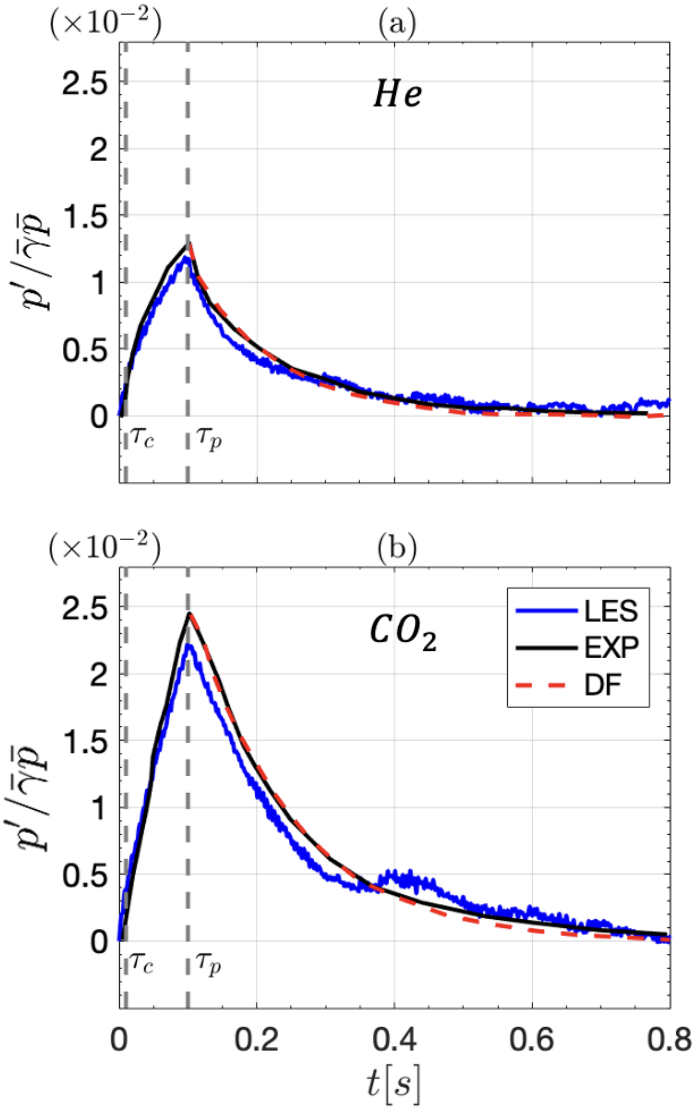

Figure 4.8: Normalised acoustic pressure fluctuations in the short pipe configuration at the upstream probe, (a) B2 with He injection and and (b) B4 with CO_2 injection.

cases discussed above where the direct noise and indirect noise are separated, the two sources of noise largely overlap in the short configuration. Figure 4.8(a) and (b) show the upstream pressure signals for the cases B2 and B4. From $t = 0$ to $t = \tau_c$, there is only direct noise present and p' increases as a consequence. Between $t = \tau_c$ and $t = \tau_p$, indirect noise is also generated, and p' represents the acoustic perturbation as a combined effect of the direct and indirect noise. Beyond τ_p there is only indirect noise present in the pipe, whilst after $t = \tau_p + \tau_c$, no noise is generated and the acoustic pressures decay until all the acoustic energy is dissipated. Additionally, a spread bump with a very low amplitude in B4 at around $t = 0.4$ s can be found as shown Fig. 4.8(b). In LES, the acoustic signal decays as a result of as the acoustic power loss due to the imperfect reflections at the edges of the system together with the numerical dissipation. This unexpected bump could be related to miss-match of the nozzle impedance, while a further investigation requires a finer mesh to resolve the flow across the nozzle, which is excluded from the current work for the consideration of cost.

When observing Fig. 4.7 and Fig. 4.8 together and comparing the maximum p' at τ_p for B1 in Fig. 4.7(a) and B2 Fig. 4.8(a), it can be found that the peak p' is much smaller by about 50% in the short configuration, caused by the negative indirect noise. In contrast for the CO_2 cases, with positive indirect noise, the maximum p' is higher in case B4 shown in Fig. 4.8(b) compared to that for B3 in Fig. 4.7(b), consistent with the positive indirect noise found in the long configuration. Since p' maxima represent the direct noise amplitudes in the long configuration and the superposition of direct noise and indirect noise amplitudes in the short configuration the results can be used to estimate the ratio, C_{id}, of the indirect to direct noise. The simulated ratio is computed to be around 0.45 for He and 0.20 for CO_2 compared with the values obtained from the measurements of about 0.42 for He and 0.27 for CO_2. The difference between He and CO_2 indirect noise amplitude is physically intuitive: the molar mass difference between He and air ($W_{air} - W_{He}$ = 25 g/mol) is higher than the one between CO_2 and air ($W_{CO_2} - W_{air}$ = 15g/mol), which results in greater changes in the flow composition and hence greater compositional wave amplitude, which finally leads to higher indirect noise amplitude.

Overall, the direct noise amplitudes are well-captured by the LES, while the indirect noises are slightly under-predicted with the deviation more obvious with CO_2 injection. This deviation is largely due to the over-prediction of the loss in the flow shown by a higher upstream pressure and therefore the

slight mismatch of throat Mach number and the upstream pressure, which influences the computed indirect acoustic source strength and the reflections at the nozzle. As discussed in subsection 4.2.1, the injected mass fraction of helium injected into the main flow is relatively low ($Y_{He} = 0.02$), while the amount of carbon dioxide injected ($Y_{CO2} = 0.2$) which is likely to be large enough to show the impact of the over-predicted loss in the fluid. In addition, the acoustic signature has been found to be related to the convection process and dispersion effect in the upstream pipe (Rodrigues et al. 2020). To further investigate this, a finer mesh is required to resolve the compositional and entropy waves propagation and dispersion, which is beyond the scope of the present work.

4.4.4 Influence of mass flow rate

Pressure signals with different air mass flow rates are studied with LES for both the long and the short pipe configurations. As discussed in Section 4.4.1, an air flow is set up in each case. The upstream pressure in cases with different mass flow rate can be used to investigate the isentropicity of the nozzles using the total pressure loss coefficient which can be expressed as follow:

$$C_{p0} = \frac{p_{0,j} - p_{0,2}}{1/2\rho_j {u_j}^2} = \frac{p_{0,1} - p_{0,2}}{1/2\rho_j {u_j}^2} \tag{4.2}$$

where C_{p0} is a normalised pressure loss coefficient and the subscripts 1, 2, j represent the upstream, downstream and position where the flow just begins to become non-isentropic. A non-isentropicity parameter β_l is introduced to indicate the level of total pressure losses occurring in the system, which is defined as $\beta_l = A_j/A_2$ where A represents the cross-section area (Domenico et al. 2019). Hence according to the definition of β_l, two limits can be given: when the flow is fully isentropic, $C_{p0} = 0$ and $\beta_l = 1$; when A_j equals to the throat area $A_t h$, the highest loss occurs in the nozzle, and hence $\beta_l = A_t h/A_2$. The latter case corresponds to the configuration of an orifice plate with the same throat area $A_t h$. As discussed in the experimental work for a given geometry and mass flow rate, each value of β_l corresponds to a specific upstream pressure $\bar{p}_1$ and to a specific mean pressure loss. The pressure $\bar{p}_1$ as a function of air mass flow rate $\dot{m}$ obtained by LES and the experiments is shown in Fig. 4.9. The two limits of isentropic flow (L2) and orifice plate (L1) predicted by the analytical

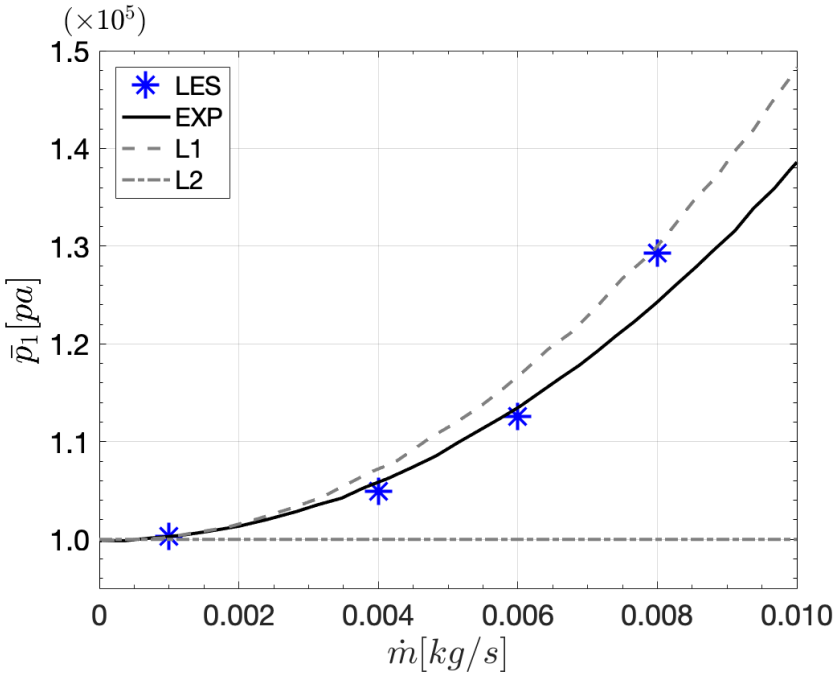

Figure 4.9: LES predicted upstream pressure $\bar{p}_1$ versus mass flow rate compared with experimental measurements. Two analytical limits are presented with L1 for the orifice plate limit and L2 for a fully isentropic nozzle.

model (di Domenico et al. 2021) are also depicted. As shown in Fig. 4.9, the basic trend of $\bar{p}_1$ rising with $\dot{m}$ is captured well by the LES. The value of $\bar{p}_1$ is well predicted until $\dot{m}$ reaches 6 g/s, but is over-estimated in B1 which is slightly lower than the $\bar{p}_1$ given by the theory for an orifice plate with the same mass flow rate. This indicates larger loss in the simulation when the flow rate is high and the Mach number in the nozzle is close and above unity. The larger discrepancy in $\bar{p}_1$ may be associated with the occurrence of shocks in the vicinity of the sudden expansion downstream of the nozzle and in these circumstances the accuracy of Boffin-LES is uncertain.

$\dot{m}(gs^{-1})$	Cases	C_{id}
1	B7, B8	0.11
4	B5, B6	0.37
8	B1, B2	0.46

Table 4.4: An estimation of the ratio of indirect noise to direct noise C_{id}.

Figure 4.10(a) presents the upstream non-dimensional pressure fluctuations for B1 ($\dot{m} = 8\ gs^{-1}$), B5 ($\dot{m} = 4\ gs^{-1}$) and B7 ($\dot{m} = 1\ gs^{-1}$) based on the long pipe configuration, while Fig. 4.10(b) shows the

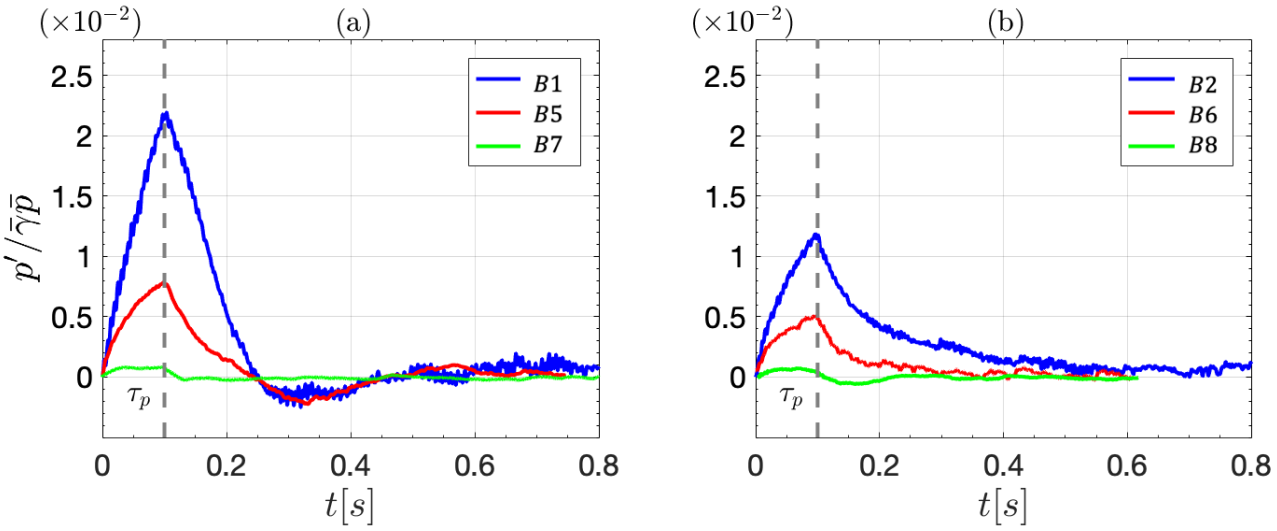

Figure 4.10: Normalised acoustic pressure fluctuations in (a) long configuration and (b) short configuration caused by injections of three different jet mass flow rates. The legends show the test cases in each plot and detailed conditions of each case are shown in Table 4.2

results in B2, B6 and B8 where the jet mass flow rates are the same as B1, B5 and B7 respectively but the short pipe configuration is adopted. In Fig. 4.10(a), the direct noise amplitude (represented by the normalised peak p') reduces from B1 to B7 with the lower mass flow rates. An estimation of the ratio of indirect noise to direct noise C_{id} can be obtained using the method outlined in section 4.4.3 and are listed in Table 4.4: $C_{id} \sim 0.11$ for $\dot{m} = 1\ gs^{-1}$ for the cases B7 and B8; $C_{id} \sim 0.37$ for $\dot{m} = 4\ gs^{-1}$ for B5 and B6; $C_{id} \sim 0.46$ for $\dot{m} = 8\ gs^{-1}$ for B1 and B2. It can be found that the ratio of the indirect noise to direct noise increases with the jet mass flow rate. Since the normalised compositional wave amplitudes are the same in all the cases with the fixed mass fraction of the injected gas to the main jet (Y_{He} is constant), this changes in the indirect noise ratio are mainly due to the increased entropic noise generated by the compositional disturbance, which is found to positively scale with the main jet mass flow rate (di Domenico et al. 2021).

4.5 Conclusions

The present work described the results of an LES study of the noise generation in an Entropy Wave Generator comprising a resonator with a non-isentropic nozzle. A fully compressible LES is per-

formed for the full 360° EWG configuration with careful choices of boundary conditions and computational domain. The disturbances are created by a cross-flow pulse injection of a secondary gas with a different composition. The pressure signal extracted from the LES reproduced the direct and indirect noise generating process and matched the measurements to a good level of accuracy for different injection gases. When the jet mass flow rates increased with a fixed compositional disturbance, the direct noise amplitude and the ratio of indirect to direct noise were found to increase as an effect of a higher entropic wave amplitude created by the compositional disturbance. The predicted noise amplitudes were found to be closely related to the losses in the system, which was over-predicted in the simulation when the Mach number in the nozzle approaching unity and shocks may exist. Under this condition the accuracy of the numerical method is uncertain. Overall, the results indicates the capability of the LES method and the successful applications of the acoustic boundary conditions with appropriate assumptions and interpolations in the study of acoustic related problems.

Chapter 5

Application to technically premixed PRECCINSTA flames

In this chapter, the last stage of the present work including the numerical study of a series of technically premixed, swirl-stabilised flames in the PRECCINSTA model combustor is presented. The fully compressible formulation of BOFFIN-LES is applied to study the unsteady combustion with thermo-acoustic and hydrodynamic instabilities. The specific objectives are to assess the predictive capabilities of the LES approach in the context of combustion dynamics under various operating conditions including different equivalence ratios and hydrogen addition and to investigate the flame dynamics in these swirling flames. To allow for this, the iso-thermal flows are first investigated, based on which three reacting cases are established. Flame topology, flow field and the related thermo-acoustic and hydrodynamic instabilities are studied and results are compared with available measurement data. The dominant feedback mechanism of the observed thermo-acoustic fluctuations are identified; the evolution of the precessing vortex core (PVC) are discussed together with the related flame stabilisation process. The interplay of the thermo-acoustic oscillations, PVC structure and the flame stabilisation process are summarise in the end, with the potential effect of the wall-heat transfer on them discussed.

5.1 Background and motivations

The target swirling flame configuration is the well-known PRECCINSTA burner, originally derived from an industrial design by Turbomeca, was first investigated as part of the EU project 'Prediction and Control of Combustion Instabilies in Industrial Gas Turbines' (PRECCINSTA). It involves lean, partially premixed, swirl-stabilised flames at atmospheric pressure. The experimental investigations of the PRECCINSTA burner at DLR were initially performed by Meier et al. (2007). The PRECCINSTA burner can be operated under a 'technically' premixed (TP) mode and a perfectly premixed (PP) mode. In reality, however, premixing of fuel and oxidiser must occur inside the combustor for safety reasons, creating only partially premixed reactants because of the limited space and time available for mixing, which is referred to as the TP mode. In the TP mode, the fuel is injected into the swirler and does not premix perfectly with the air before reaching the flame. Compared to PP flames, thermo-acoustic oscillations in TP flames exhibit an additional complexity as they are driven not only by velocity fluctuations but also by equivalence ratio fluctuations in the unburned mixtures entering the flame zone (Lieuwen & Zinn 1998, Schuermans et al. 2010, Hermeth et al. 2013).

Meier et al. (2007) initially examined PRECCINSTA TP CH_4/air flames with different operating conditions and focused on condition: (a) a quiet flame (F1), thermal power $P_{th} = 30$ kW and equivalence ratio $\phi = 0.83$; (b) an unstable flame (F2), $P_{th} = 25$ kW and $\phi = 0.7$. In the pulsating flame, self-sustained thermo-acoustic fluctuations were observed with a dominant characteristic frequency; Boxx et al. (2012) later detected a helical precessing vortex core (PVC) in the F2 flame, which features a frequency twice of the thermo-acoustic mode. Meier et al. (2007) identified a fluctuating fuel supply, subject to a convective time delay, as the main mechanism of the thermo-acoustic fluctuation in pulsating flame F2. The quartz glass windows for optical access to the flame were loosely mounted to the chamber to avoid thermal stress, which was observed to be vibrating and not fully gas-tight and potentially damp the thermo-acoustic oscillations. Stöhr et al. (2017) compared the flame dynamics of a TP flame and a PP flame with the burner operated under a different condition with $P_{th} = 15$ kW and an equivalence ratio $\phi = 0.8$. It was found that the strong unsteady interactions between the equivalence ratio fluctuations and velocity fluctuations dominated the thermo-acoustic mode in TP flames, supporting the findings by Meier et al. (2007). Recently Chterev & Boxx (2019) and Kushwaha et al.

(2021) extended the range of operating conditions of the TP flames: P_{th} from 10 kW to 30 kW, ϕ from 0.65 to 1.05 and hydrogen concentration from 0% to 40%. The flame and flow behaviour were found to vary significantly across different operating conditions, and the impact of H_2 enrichment on the flame dynamics also strongly depended on the operating conditions. The effect of hydrogen enrichment was also investigated by (Chterev & Boxx 2021) at elevated pressure up to 5 bar with a slightly increased burner length design.

Combustion of hydrogen enriched flames has gained growing worldwide interest. Hydrogen as a fuel may offer higher energy density and lower emission, and it can be reproduced from renewable power sources such as solar, wind and geothermal energy (Edwards et al. 2008). Compared to CH_4, H_2 has a higher adiabatic flame temperature (at stoichiometric conditions in air, 2383 K and 2220 K), lower flammability limit (ϕ = 0.14 and ϕ = 0.46) and higher maximum adiabatic laminar flame speed (320 cm/s and 40 cm/s) (Glassman et al. 2014). Hence changes in the fuel by hydrogen enrichment can drastically change the combustion characteristics, including the lean blow-off limit, auto-ignition, flashback and combustion instabilities (Lieuwen et al. 2008). Taamallah, LaBry, Shanbhogue & Ghoniem (2015) and Shanbhogue et al. (2016) experimentally investigated the flame shape transition in a series of hydrogen-enriched swriling flames. They found that hydrogen addition brought down the critical equivalence ratio at which the flame shape transitions occurred. Karlis et al. (2019) further examined the applicability of the extinction strain rate as a scaling parameter of the observed combustion dynamics transitions in methane hydrogen flames.

Only a few numerical works in the published literature have attempted to investigate the TP unstable flames in the PRECCINSTA burner. Franzelli et al. (2012) first performed a compressible LES of the F2 flame to capture the self-excited thermo-acoustic mode. It was concluded that both the compressibility of the fluid and the fuel-air mixing must be included to predict the thermo-acoustic coupling in the F2 flame. Fuel was found to accumulate periodically in the swirler, confirming the explanation for the mechanism of the TP feedback loop proposed by Meier et al. (2007). An over-estimation of the dominant frequency was attributed to a mismatch of the acoustic impedance at the fuel injection. Lourier et al. (2017) performed a scale-adaptive simulation of the F2. For a better defined acoustic inlet boundary, a choked orifice plate was installed in the air supply, leading to a marginal decrease

of the predominant thermo-acoustic frequency by about 15 Hz compared to the original experiments. Besides, the combustion chamber side walls were made of quartz glass plates in the experiments by Meier et al. (2007), which are loosely mounted in the corners of the chamber in order to avoid thermal stress. Due to the loose support, the side walls are vibrating and not fully gas-tight, which may lead to damping of the thermo-acoustic oscillation. In order to assess the influence of the quartz windows, pressure spectra were measured both for the original configuration with quartz glass windows and a modified configuration with rigid metal walls. Power spectral density (PSD) analysis showed that fixing the chamber wall increased in the thermo-acoustic amplitudes of around 10 dB for both the chamber and air plenum pressure, while suppressing the damping effect with the frequencies unaltered. Recently, Fredrich et al. (2021*b*,*a*) examined the combined effects of interacting thermo-acoustic and hydrodynamic instabilities in flame F2 using BOFFIN-LES. A superposition of velocity fluctuations and equivalence ratio oscillations was identified to drive the thermo-acoustic feedback loop. An oscillation of the instantaneous swirl number was found to be correlated to the periodic oscillations of the flame angle and the excitation and suppression of hydrodynamic flow phenomena including a single PVC and toroidal vortex.

5.2 Case description

Figure 5.1 shows a schematic of the burner. Four sections can be identified from left to right, namely the air plenum, injection unit, combustion chamber and exhaust pipe. The injection unit comprises a radial swirler with 12 rectangular vanes and a burner nozzle with a conical central bluff body. Dry air is fed into the air plenum via a large orifice, and the fuel gas is injected into the air flow through 12 small tubes within the swirler, where the air and fuel are mixed with high momentum. The combustion chamber is confined with four thick quartz windows with a square cross section of 85×85 mm and a length of 114 mm. The hot products exit the chamber through a converging pipe followed by an exhaust pipe with 40 mm diameter and finally into the atmosphere.

The pressure signals are recorded to provide information on combustion dynamics using 2 microphone probes: one in the plenum (Probe PL) and one in the chamber (Probe CH) as shown in Fig. 5.1.

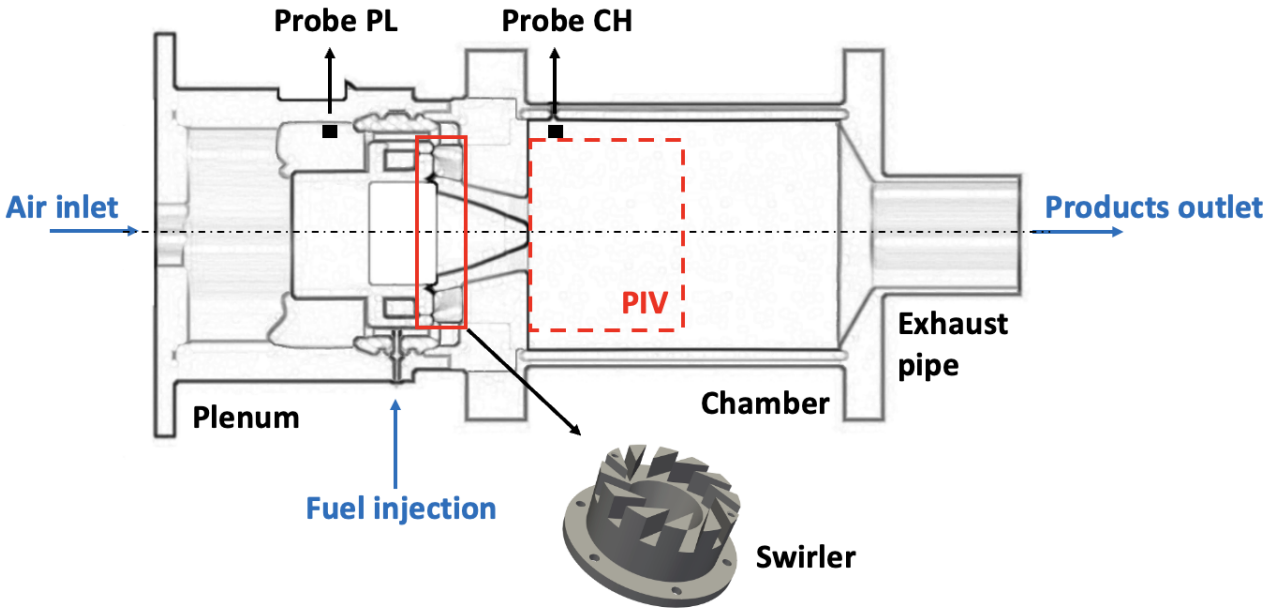

Figure 5.1: The experimental configuration of the PRECCINSTA burner (Chterev & Boxx 2019).

The flames are visualised by line-of-sight OH chemiluminescene (OH-CL) measurement which is a common and reliable marker for the heat release rate (Chterev & Boxx 2021). Velocity fields are measured using 10 kHz stereo partial image velocimetry (PIV) with the optical view marked in Fig. 5.1. The Reynolds number at the exit of the nozzle based on the cold flow and the exit diameter is about 35,000. The swirl number is fixed and is estimated at a value of 1 in the experiments. It is worth noting that the swirl number here is referring to the 'geometry swirl' number which is a predetermined value using the geometry dimensions of the swirler. The effective swirl number S describing the the degree of swirl in a swirling flow originally proposed by Chigier & Beér (1964) is defined as:

$$S = \frac{Gy}{RGz} = \frac{\int_0^{R_n} wvr^2 dr}{R_n \int_0^{R_n} w^2 r dr} \tag{5.1}$$

where Gy is the axial flux of the azimuthal momentum, Gz is the axial flux of axial momentum and R_n is the burner nozzle equivalent radius. This effective S estimated using axial and azimuthal velocities was found to differ significantly from theoretical estimate, which is smaller than the corresponding geometrical one in most cases (Palies et al. 2010).

Among all operating conditions, the present work focus on five cases as summarised in Table 5.1.

Case	N1	C1	N2	C2	C3
H_2 by vol	0%	0%	0%	0%	38%
P_{th} (kw)	20	20	22.8	22.8	22.8
ϕ	0.65	0.65	0.85	0.85	0.85
$\dot{m}_{air}$ (g/s)	10.55	10.55	9.12	9.12	8.91
$\dot{m}_{CH_4}$ (g/s)	0.399	0.399	0.456	0.456	0.380
$\dot{m}_{H_2}$ (g/s)	0	0	0	0	0.029
Reacting (Y/N)	N	Y	N	Y	Y

Table 5.1: Operating conditions for the selected cases.

Constant and uniform velocities, consistent with the mass flow rates, were applied at both the air and fuel inlet boundaries. All cases have a similar thermal power ~ 20 kW. C1 features a lower fuel/air equivalence ratio $\phi = 0.65$, while in C2 $\phi = 0.85$. In C1 and C2 the fuel consists of pure methane, while in C3 the fuel is enriched with 38% hydrogen by volume. Two iso-thermal cases N1 and N2 feature the same operating conditions as C1 and C2, respectively. All selected cases are performed under atmospheric pressure, and the fuel and air mixture are slightly preheated to reach temperatures between $T \sim 310\ K$ and $T \sim 380\ K$.

The reason for such a selection is the rich physics observed in these cases. In C1, an oscillating flame with strong self-excited thermo-acoustic oscillations was detected; the flame presents an M shape, which is closely related to the formation of a PVC structure (Oberleithner et al. 2015). C2 represents an unstable case with weak thermo-acoustic oscillations: the dominant thermo-acoustic fluctuation amplitude is about 20% of the one in C1 in pascal. Besides, the flame remainds attached to the burner centre body, which features a V shape. C3 aims at investigating on the effect of H_2 enrichment compared to C2, where the thermo-acoustic oscillations found in C2 are suppressed and the flame retains a V shape. When compared with previous work on the PRECCINSTA flames, flame C1 has great similarity to the pulsating flame F2 in Meier et al. (2007), which numerically has been investigated by Franzelli et al. (2012), Lourier et al. (2017), Fredrich et al. (2021*b*,*a*). The present work is one of the first numerical work to investigate the C2 type flame and C3 flame (or any other stable flame) using a fully compressible LES method.

5.3 Numerical set-up

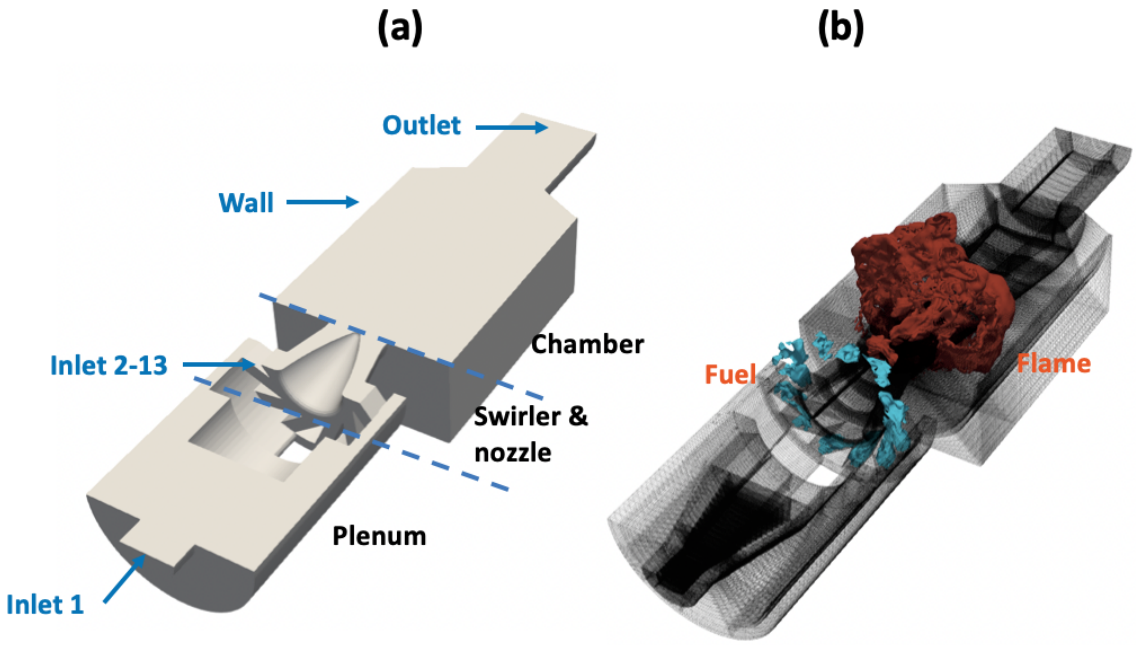

Figure 5.2: Left: A view of the computational domain cut half along a centre line. Right: Computational mesh on the half domain, with iso-contours of the instantaneous fuel mass fraction (blue) and HRR (red) showing the region of fuel injection and flame zone, respectively.

In order to investigate the thermo-acoustic response of the system, compressible LES, BOFFIN-LES is performed, with the governing equations and modelling strategies described in Section 2.2 and 2.3 employed. The reduced chemical kinetics mechanism employed for the oxidation of methane and hydrogen is the reduced mechanism by Lu & Law (2008) as introduced in Section 2.3. GRI-Mech 3.0 has been validated in many experimental work for CH_4/H_2/air flames and very good agreement was obtained for key combustion attributes including larminar flame speeds, ignition delay time, NO_x levels, profiles of major species, extinction strain rates, etc (Ren et al. 2001, 2002, Halter et al. 2005, Chaumeix et al. 2007, Hu et al. 2009). Reduced mechanisms developed from GRI-3.0 (Hawkes & Chen 2004, Safta & Madnia 2006) and from GRI-2.11 (Jackson et al. 2003) were also examined for CH_4/H_2 flames, where good agreement over a wide range of mixture conditions were achieved. Hence, it is convincing that the reduced mechanism compares well with the full GRI mechanism to capture the qualitative effect of H_2 addition.

The computational domain is shown in Fig. 5.2(a) (cut half), which includes the region in the air

plenum, swirler, nozzle and the combustion chamber. Air is injected with a constant air mass flow rate at the inlet of the air plenum (inlet 1); fuel is injected via twelve injectors in the swirler (inlet 2-13). Consequently, instead of assuming perfect premixing, the fuel-air mixing is explicitly computed in the simulation to represent the TP mode.

The computational mesh is shown in Fig. 5.2(b) with iso-contours of the instantaneous fuel mass fraction (blue) and heat release rate (red) showing the region of fuel injection and reaction, respectively. The structured mesh consists of about 2.7 million grid cells, which are clustered in the reaction zone and the fuel-air mixing region, leading to lengths ranging from 0.1 to 1 mm in all three spatial directions. Besides, the mesh is refined towards the domain walls resulting in an dimensionless wall-normal distance y^+ between 20 and 30 in the swirler and nozzle regions, and below 10 in the combustion chamber. As discussed in Chapter 2.4, such a mesh distribution is not sufficient to resolve the boundary layer turbulence structure accurately, as a consequence wall-functions are applied at all solid boundaries. In combustion chamber flows of the type considered here, the flow is dominated by turbulence generated far from walls; the turbulence in the vicinity of a solid surface and the wall shear stress exerts a negligible influence on the overall flow structure. Mesh independent study has been done and the current mesh has been shown to have the ability to capture the main flow motion and resolve the acoustic waves of interest.

Non-adiabatic combustion chamber walls with fixed temperature (Dirichlet boundary conditions) are implemented on all the chamber walls and the centre body to include the wall heat transfer effect. In the previous study of confined swirling flames, many experimental and numerical studies have found on the impact of wall heat transfer on flame stabilisation and dynamics, and thermo-acoustic instabilities were also found to be closely related to themal boundary conditions. As suggested by Kedia et al. (2011), the flame-wall interaction was found to be crucial in closing the feedback loop between the heat release rate and the velocity oscillations, which may result in a resonant behaviour. The temperature in the region near the flame holder was found to be closely related to the flame root dynamics and correlated to the unsteady flame behaviour in many configurations, e.g. a backward-facing step combustor (Hong et al. 2013) and swirling flames (Foley et al. 2017). The temperature of the combustor side walls were also found to have a strong impact on the flame shape and stabilisation

(Guiberti et al. 2015), near-wall scalar fields and local-extinction (Benard et al. 2019, Fredrich et al. 2019).

Ideally, wall temperatures under the each operating condition should be measured and used as boundary conditions for the simulations, which however, is not available for the many experiments. In the PRECCINSTA burner, the surface temperatures were measured only in Yin et al. (2017) with the operating condition $P_{th} = 20$ kW and $\phi = 0.7$, which is different from the operating condition selected for the current study but close to C1 with a slight lower equivalence ratio ($\phi = 0.65$). The chamber side walls were measured to be around 1400 K and the base plate wall around 700 K, and these values are used as fixed wall temperatures in the current simulations. The resulting preheated air and fuel temperature are estimated as 320 K in the simulations based on the measurements of the F1 flame. The rationality of these estimations are confirmed by the experimentalists (Chterev 2020). Non-reflective outflow boundary conditions described in Chapter 2.4 are adopted at the outlet of the chamber.

All parameters of the models and boundary conditions are fixed at the numbers presented in Chapter 2; that is to say, none of them are adjusted to match the experimental results. The simulations were carried out with a constant time step of $\Delta t = 1 \times 10^{-7} s$. The largest CFL number is monitored instantaneously and limited below 0.25. All simulations were set to develop for about 6 combustor flow-through times based on the bulk flow velocity through the combustion chamber. Statistics were subsequently collected over a further of 6 combustor flow-through times. The total computational cost to perform an LES/PDF simulation for each case amounts to about 1,500 CU (1 ARCHER2 CU = 1 Node hour = 128 CPUhs) on the ARCHER2 UK National Supercomputing Service (https://www.archer2.ac.uk).

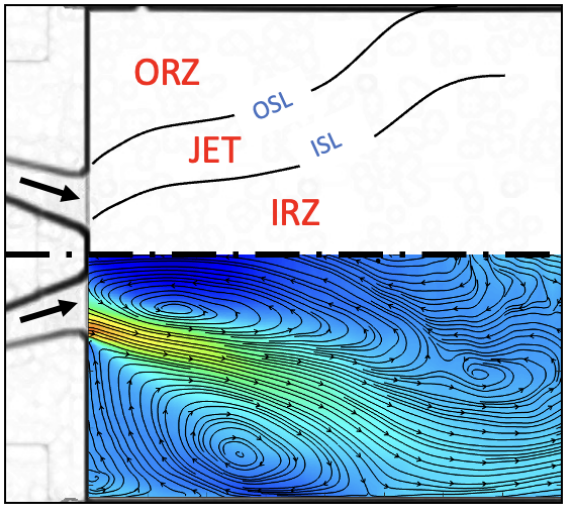

Figure 5.3: Top: Notional fluid features for swirling flow. Bottom: Mid-plane contour of axial velocity with time-averaged streamlines in N1.

5.4 Results and discussions: non reacting cases

5.4.1 General flow structure

Swirling flames exhibit complex hydrodynamic features and many fundamental aspects of the flow structures and instabilities are still under active investigation. A comprehensive overview of these phenomena can be found in Candel et al. (2014). Figure 5.3 shows a swirling flow field with time-averaged streamlines. Although the centerbody is tapered, at the current high swirl number the flow separates along the centerbody resulting in three regions (Meier et al. 2007): the swirling conical jet; the outer recirculation zone (ORZ), which is a toroidal recirculating zone caused by the sudden area expansion from the nozzle to the chamber and the confinement of the chamber walls; the inner recirculation zone (IRZ), which is created by the swirl-induced vortex breakdown. The IRZ is of particular importance in stablising the flame, which provides a low speed region where the flame can anchor and serves as a continuous ignition source through re-circulation of hot burnt products (Durox et al. 2013). The inner shear layer (ISL) separates the jet and the IRZ and provides a flame stabilisation location, which can origin upstream from the dump plane due to the flow separation from the centre body. The outer shear layer (OSL) is the layer between the jet and the ORZ, providing a

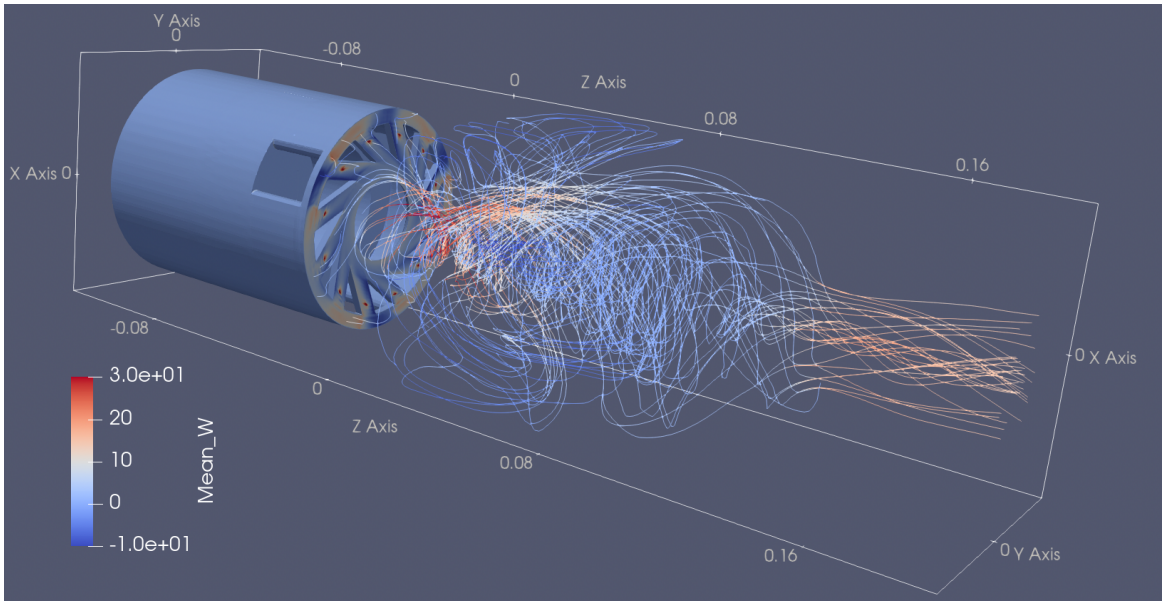

Figure 5.4: Time-averaged 3D pseudo streamlines coloured by mean axial velocity in the region downstream of the swirler in N2.

secondary stablisation location for the flame which starts from the annulus lip.

In addition to the in-plane motions, the radial swirl generates strong azimuthal motions in the flow, which can be visualised by representative 3D streamlines of the flow field as shown in Fig. .5.4. It can be seen that the flow develops precessingly in the nozzle after leaving the swirler and then into the chamber where the recirculation in the ORZ is shown by the bending streamlines with negative axial velocity; the jet region features a high axial velocity shown by the red streamlines; the IRZ is not distinct in the present view since it is wrapped by the annular jet. The azimuthal motion together with the radial and axial velocity present a strong precessing motion with an increasing precession angle in the jet and the downstream region of the IRZ, before entering the convergent downstream nozzle where the flow is accelerated in the axial direction and becomes more homogeneous.

5.4.2 Flow field analysis

For the characterisation of the flow field, the non-reacting case, N1 and N2 are studied in the first place. The time-averaged flow field of N1 is shown in Fig. 5.5 and Fig. 5.6 as an example. LES predictions are compared with measurements in terms of mean axial (W), radial (U) and azimuthal

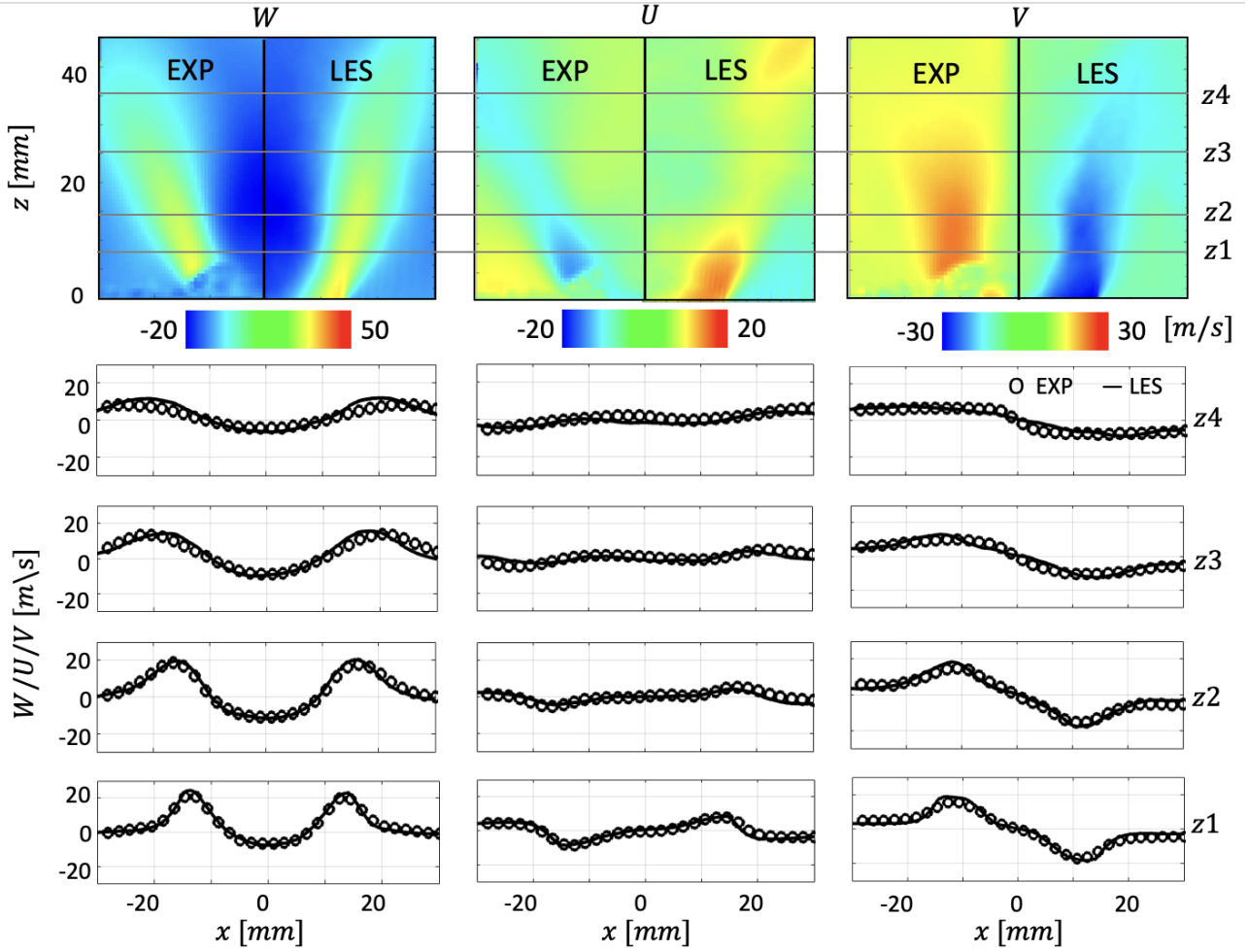

Figure 5.5: Comparison of mean axial (W), radial (U) and azimuthal (V) velocities. Top: Velocity contours; Bottom: velocity profiles.

(V) velocities, and *rms* axial (rms_w), radial (rms_u) and azimuthal (rms_v) velocities, respectively. For all the images in the present work, the chamber dump plane is defined as $z = 0$ mm. Contours on a mid-plane of the combustor are shown with radial profiles at four downstream positions ($z1 = 7$ mm, $z2$=15 mm, $z3 = 25$ mm, $z4 = 35$ mm) presented for a quantitative comparison. As can be seen in Fig. 5.5, there is an artefact in the velocity field measurement out to about 7 mm from the dump plane in the PIV figures from the experiments. This is caused by a strong reflection of the laser at the burner surface and has little influence on the regions of interest.

The comparison for all the contours and profiles shows that the overall flow field is well reproduced. The jet axial velocity reaches a peak ~ 25 m/s at the nozzle exit, while the highest backflow velocity in

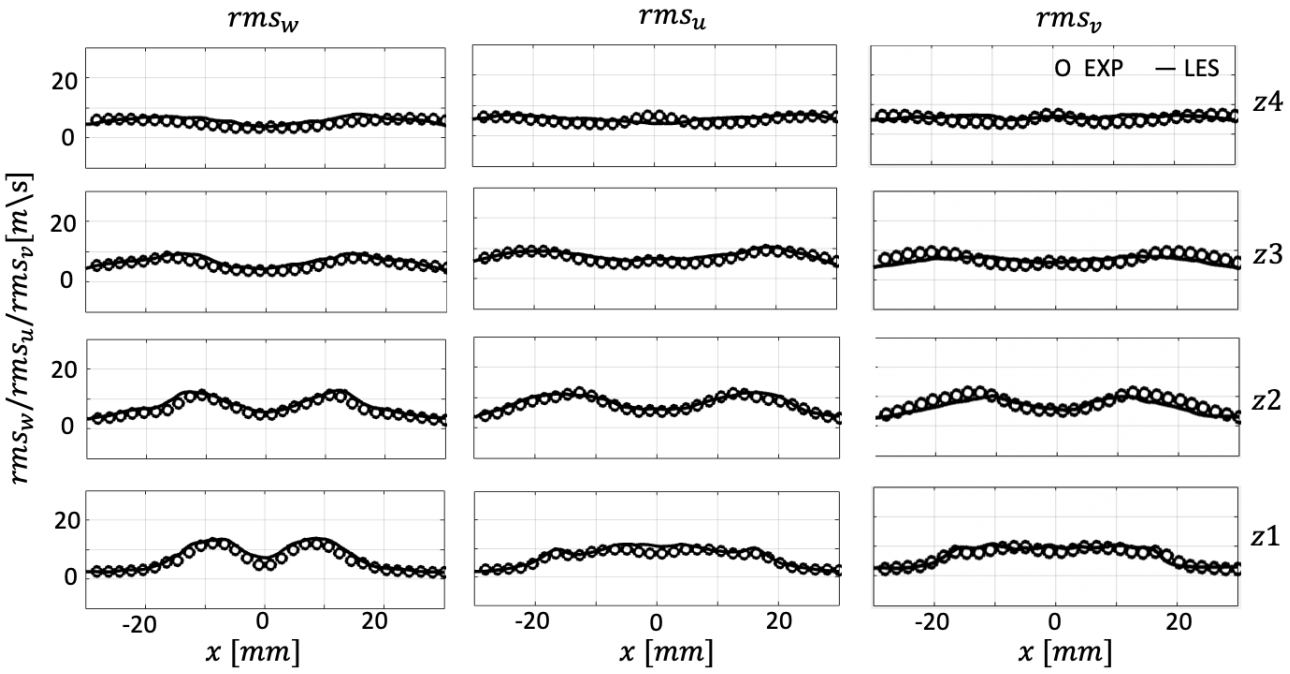

Figure 5.6: RMS axial (rms_w), radial (rms_u) and azimuthal (rms_v) velocities profiles.

the IRZ is ~ -10 m/s at about z2. The mean velocities are well predicted for all velocity components including the azimuthal velocity V, which indicates the swirl level in the LES is in good agreement with the measured one. According to the definition of the swirl number as shown in Eq.5.1, the swirl number at the dump plane is found to be $S \sim 1.06$ in the LES and remains nearly constant. The width of the IRZ from z = 35 mm to further downstream is slightly under-predicted, which indicates a smaller spreading angle of the swirling jet. The flow spreading angle is strongly affected by the flow separation at the nozzle lip, which requires a very fine near-wall mesh to resolve. The slightly narrower ISL suggests that the flow separation is early in the simulation, resulting in a slight under-prediction of the jet spreading angle. This is a well-known limitation of most LES in combustion chambers, but has a limited influence on present work which focuses on combustion dynamics and thermo-acoustic oscillations (Roux et al. 2005).

The *rms* velocities predicted by LES are also in excellent agreement with the experimental results, which suggests the fluctuations in the flow are well predicted. There are high levels of axial fluctuations (rms_w) in the IRZ close to the nozzle outlet around the centreline. This is contributed by the turbulent fluctuation as well as the coherent structures in the flows, which is discussed in the analysis

of the transient behaviour of the flow field in the next section. The time-averaged flow field (mean and *rms*) of N2 shows similar results as N1, except for a lower velocity magnitude for all components due to the lower total mass flow rate as listed in Table 5.1. Overall, the mean flow field and the velocity fluctuations in the non-reacting cases are well-reproduced by the LES.

5.4.3 Dynamic analysis

PVC is interpreted as a nonlinear global mode of instability in local linear stability analysis in both laminar flow (Gallaire et al. 2006) and turbulent flow (Oberleithner et al. 2011). In swirling flows as the swirl number increases, the flow undergoes a strong vortex break down, which can induce a spiralling vortex structure, PVC, in the vicinity of the ISL as a result of a super-critical Hopf bifurcation (Liang & Maxworthy 2005). The role of the PVC in swirling flows is discussed in iso-thermal flows in the review on vortex breakdown (Lucca-Negro & O'Doherty 2001), and in reacting flows in the reviews by Syred (2006) and Candel et al. (2014). The emergence of the PVC in iso-thermal PRECCINSTA flows was first reported by Roux et al. (2005), where low-pressure iso-surfaces were used to visualise the PVC structure. Large scale vortical structures in the flow are often visualised using low pressure iso-surfaces (Poinsot & Veynante 2005), since coherent structures are found to be associated with local minima of the pressure field (Jeong & Hussain 1995) which are strongly coupled with high levels of velocity fluctuations. Hence in the present work, coherent structures in the simulations are also identified using the same method with low-pressure iso-surfaces.

As shown in Fig. 5.7(a), a helical PVC structure can be found in the vicinity of the ISL, originating from the region in the nozzle below the dump plane. The vortex core grows anti-clockwise from the top view (same as the swirl direction), while it precesses clockwise, which is typical for PVC structure to precess in the same direction as the flow but is winding in the opposite direction (Oberleithner et al. 2011). Figure 5.7(b) shows the flow field on a 2D slice perpendicular to the y-axis as shown by the red dashed line in Fig. 5.7(a), where a distinct zig-zag vortex pattern can be found. The PVC features a precessing frequency related to the vortex core precession f_{pvc} which is a global frequency and is typically the same throughout the combustor (Syred 2006). In the present burner f_{pvc} can be determined using velocity probes in the ISL or the chamber acoustic signals (Boxx et al. 2012), which

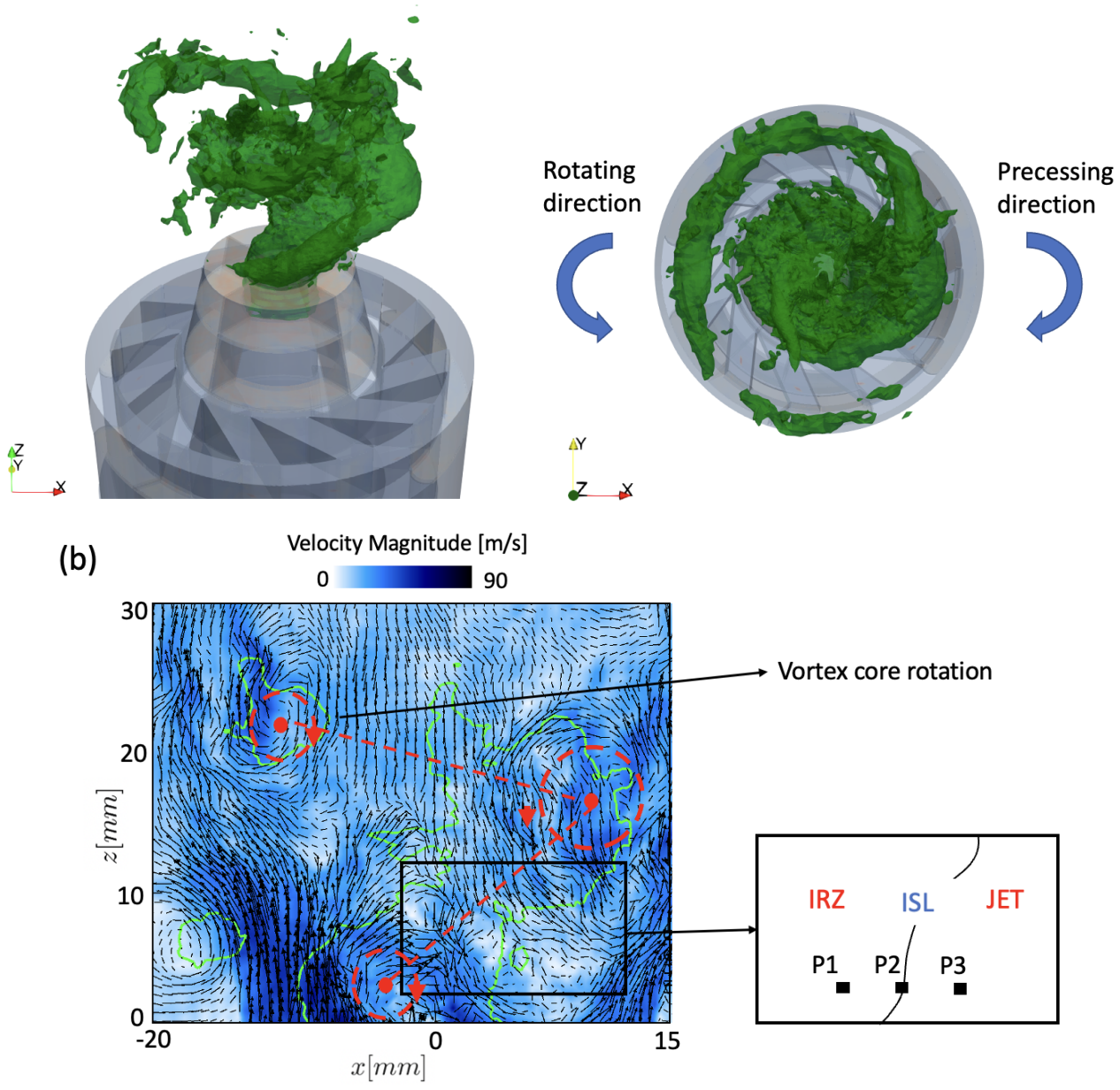

Figure 5.7: Coherent structure visualisation: (a) 3D low pressure iso-surfaces; (b) In-plane velocity vectors and the pressure contours overlapped on the velocity magnitude.

is presented in the following section.

Spectra analysis

To investigate the dynamics of the flow field, the velocities are monitored at three probes within the IRZ (w_{IRZ}), ISL (w_{ISL}) and Jet (w_{Jet}), with the locations shown in the frame in Fig. 5.7.

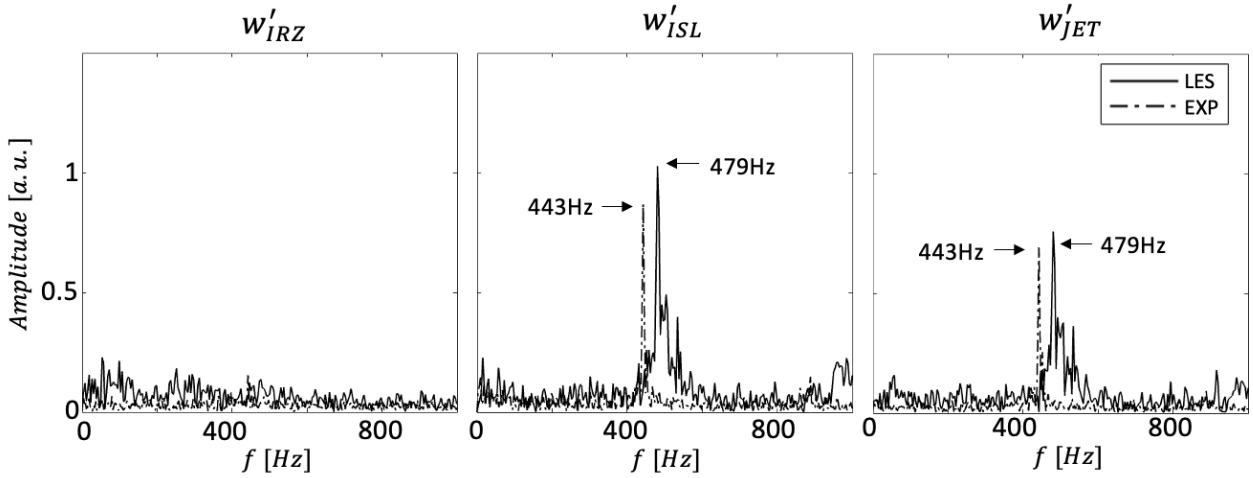

Figure 5.8: Spectra of the axial velocity fluctuations in N1: Comparison of the experiments (experiment) and LES results. The monitoring probes are in the IRZ, ISL and the jet region as marked in Fig. 5.7. The signals are normalised by the peak amplitude achieved in the w'_{ISL} spectra.

The existing modes in these signals are retrieved via frequency spectra obtained using fast Fourier transformation (FFT). Fig. 5.8 compares the axial velocity flucutaion spectra of w'_{IRZ}, w'_{ISL} and w'_{JET} achieved from the LES and the experiment results in N1. It should be noted that the experimental FFTs are built for a duration of 1 s, while the numerical spectra are calculated over a time of 0.1 s. Despite the shorter physical time in LES, the results have been found to be almost insensitive to the length of duration after about 0.05s. The sampling frequency of the velocity and pressure is 10 kHz and 100 kHz, respectively in the experiments, and 1000 kHz in the LES. Frequencies of interest are below 1000 Hz in the PRECCINSTA configuration (Meier et al. 2007). Hence, the waves of interest are well resolved in both the experiments and in the LES.

The w'_{ISL} spectra in Fig. 5.8 shows a distinctive single peak at 479 Hz in the LES and 443 Hz in the experiment, which are also found in the spectra of w'_{JET} in the jet region with a relatively lower

magnitude but not seen in the w'_{IRZ}. This indicates the existence of strong periodic hydrodynamic fluctuations in the ISL and the jet with a fixed frequency, which corresponds to the observed PVC precession. The predicted dominant f_{pvc} is hence 479 Hz in the LES which is close to the measured 443 Hz in the experiments (about 8% difference). In isothermal flows, the frequency of the PVC can be readily characterised by the swirl number S and a Strouhal number defined as $St = fl/u$, where f is the frequency of vortex shedding, l is the characteristic length and u is the flow velocity. Hence, given the good prediction of the velocity field, the slight discrepancy of f_{pvc} is likely due to a mismatch of the predicted vortex shedding details in the vicinity of ISL.

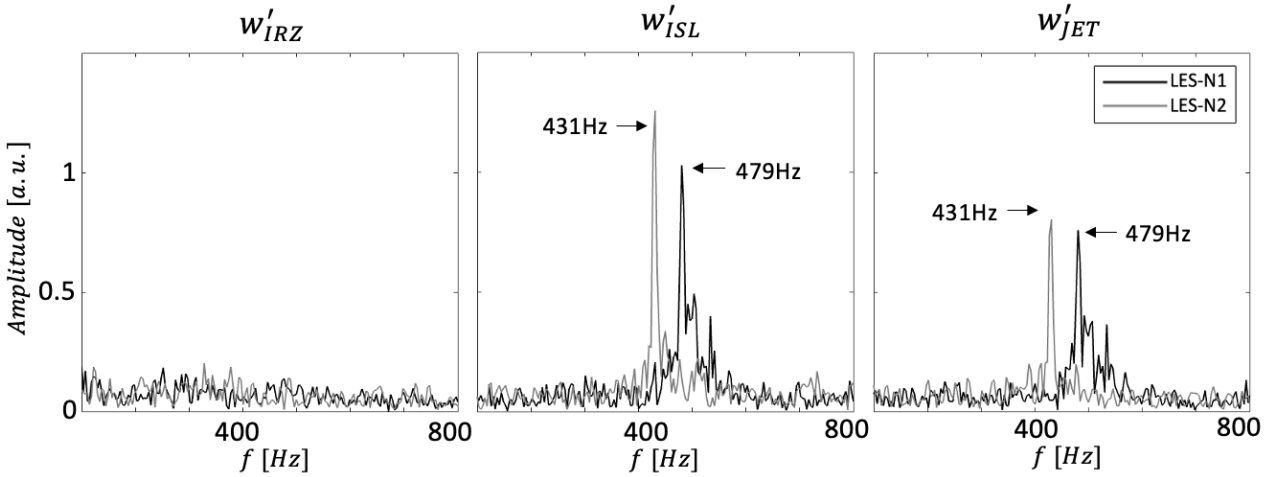

Figure 5.9: Comparison of axial velocity spectra in N1 and N2.

Due to the fact that no measurements are available for N2, the LES results of N2 are compared with N1 as shown in Fig. 5.9. The f_{pvc} in N2 is found to be 431 Hz compared to the 479 Hz found in N1, which is consistent with the claims by Syred (2006) that the PVC frequency increases quasi-linearly with the flow rate. In the previous experimental study of the PRECCINSTA burner, a PVC is always found active in the non-reacting flows, while in reacting flows the PVC was found to be suppressed under certain conditions (Roux et al. 2005, Oberleithner et al. 2015). This hydrodynamic mode is also found in the chamber pressure fluctuations: the pressure spectra of p'_{ch} are shown in Fig. 5.10 for N1 and N2, with a dominant peak at 479 Hz and 431 Hz, respectively, which are not observed in the plenum. This supports the hydrodynamic nature of the observed 479 Hz oscillations with effects confined inside the chamber instead of being global. It can be understood as such that the PVC acts acoustically like a rotating solid placed in the flow (Roux et al. 2005), which radiates weakly outside

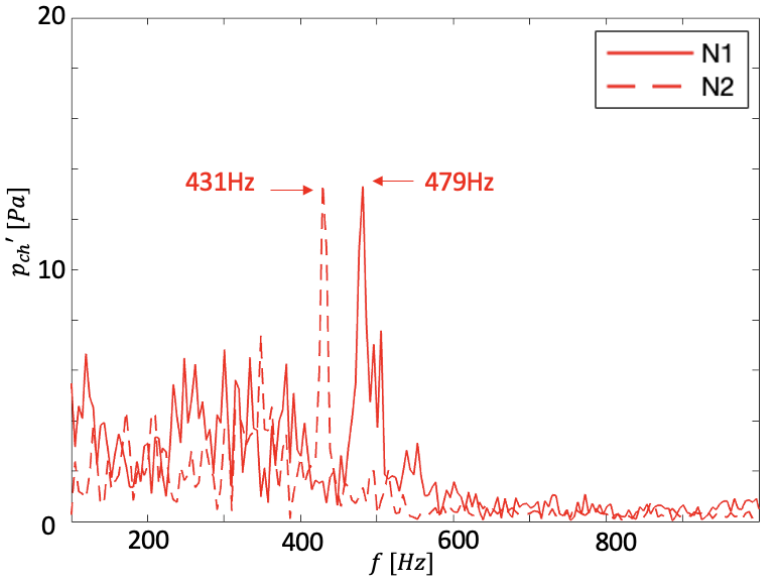

Figure 5.10: Combustion chamber pressure fluctuation spectra p'_{ch} in N1 and N2.

of the chamber.

Vortical structure evolution

The PVC evolution and its interaction with the ISL are investigated and shown in Fig. 5.11 and Fig. 5.12. Different phase angles are defined based on w'_{ISL} oscillations, as shown in Fig. 5.11(a): in each cycle, at $\theta = 0°$, w'_{ISL} has roughly the highest negative value, and starts to climb slowly until $\theta = 270°$ when the highest positive velocity is reached; after this, w'_{ISL} drops rapidly to the minimum value, at $\theta = 360°$, when the next cycle begins. This process is closely related to the precession of the PVC. At $\theta = 270°$, shown in Fig. 5.11(b1), the probe intersects with the upper edge of the PVC which is precessing clockwise from the top view; with this precesssion motion, the jet is pushed away and the IRZ expands locally; the probe is then enclosed into the helical structure and the local w reduces due to the rotation and re-circulation inside the PVC until $\theta = 360°$ when the lower edge of the PVC reaches the probe (shown in Fig. 5.11(b2)). Then w'_{ISL} begins to increase as an effect of the localised contraction of the IRZ and the jet expands, until the PVC upper edge reaches it again in the next cycle. Figure 5.12 shows the precessing PVC structure in one cycle. Clearly, a single PVC dominates the flow field and exists consistently, which precesses by 360° in one cycle with a nearly

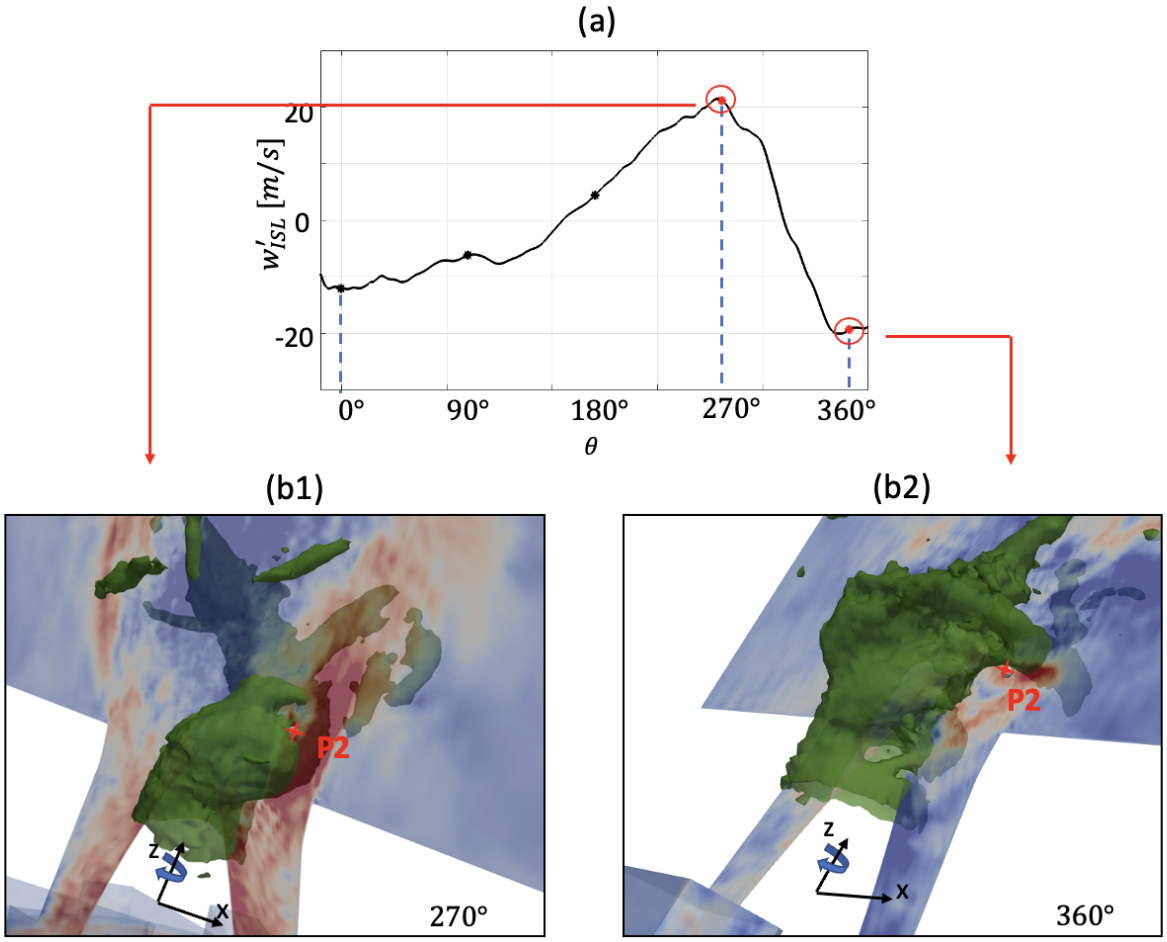

Figure 5.11: Top: Axial velocity fluctuation in the ISL in one cycle from phase angle $\theta = 0^\circ$ to 360°. Bottom: Typical PVC interaction with axial velocity on the mid-plane at $\theta = 270^\circ$ and $\theta = 360^\circ$. The position of the probe on the mid-plane is marked with a red star sign in each figure.

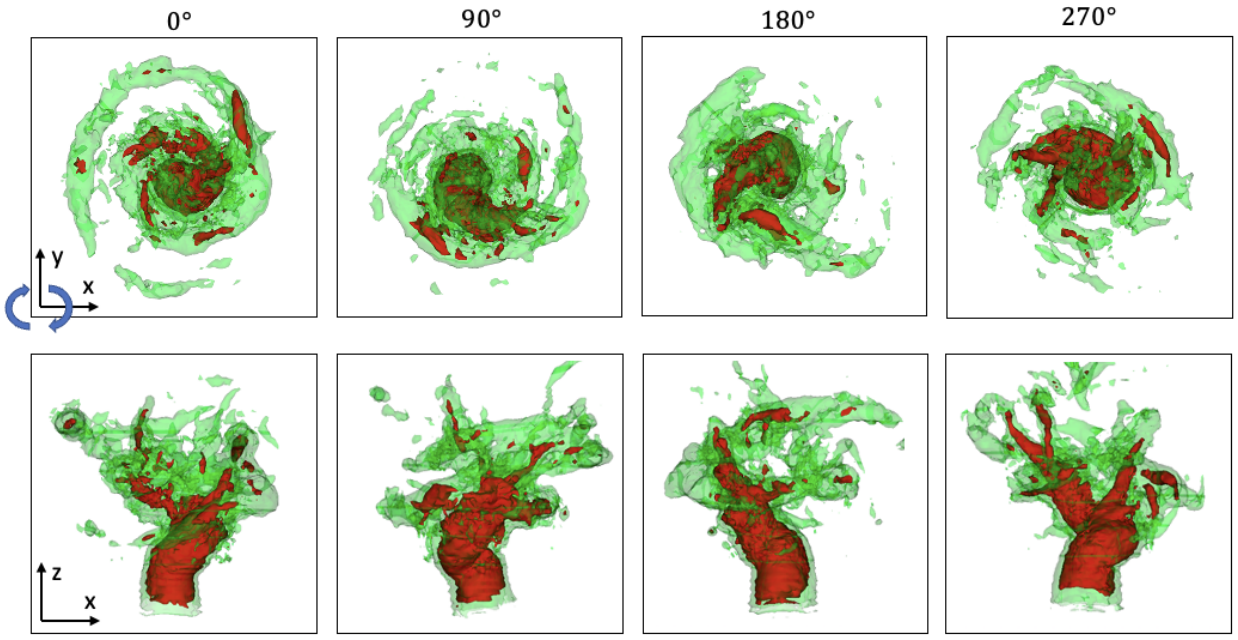

Figure 5.12: Typical PVC structures in one cycle. Top: Top view from +z; the curved arrows around the axial indicating the PVC is precessing clockwise from the top view. Bottom: Side views from -y. Red contours are iso-surfaces of $P = 99600$ Pa and green ones are $P = 99800$ Pa, describing the core and edge of the PVC, respectively.

constant spinning rate. The frequency of the PVC precession about the axis can also be estimated from the period time for one cycle which is about 2.37 ms as shown in Fig. 5.11(a). Hence the f_{pvc} in N1 is computed to be 434 Hz, which is close to the dominant mode frequency of 479 Hz found in the spectra. This further confirms the main dynamic mode is a single PVC mode in the non-reacting cases in the LES study.

To summarise, the iso-thermal flow field is found to be dominated by a consistent PVC, which causes the expanding and contracting of the IRZ at the same frequency. The PVC frequency can be detected in the power spectra of the velocity fluctuations at the ISL and the jet probe, which is successfully predicted by the LES compared to the measurements. The flow field and hydrodynamic features of the iso-thermal cases are well predicted by the simulations, which suggests the LES framework and sub-models are capable of capturing the complex flow dynamics in this combustor.

5.5 Results and discussions: reacting cases

In this section, the reacting cases C1, C2 and C3 with the conditions listed in Table 5.1 are investigated. Thermo-acoustic instabilities and hydrodynamics instabilities are observed in all the cases. The flame topology together with the flow field are discussed in the first place, followed by the dynamic analysis of each case.

5.5.1 Flame topology and flow field

Effect of the equivalence ratio and H_2 enrichment

In order to visualise the flame topology and its location, the time-averaged HRR, OH mass fraction (Y_{OH}) and axial velocity (W) on the mid-plane are shown in Fig. 5.13 from left to right. The W fields are overlaid on top by the contours of a binarised Y_{OH} using a threshold value. The threshold value of Y_{OH} is set as 80% of the maximum value in each case, with which the key features of the flames are reserved. From top to bottom are the results of C1, C2 and C3 respectively. Flame regions are characterised using HRR images and the Y_{OH} field showing the presence of hot burned products. The results present two main types of flames in terms of the flame topology: in C1 the flame features an M shape which is lifted above the centre cone; while in C2 and C3 a V shape flame stabilised along the ISL can be found. As discussed in Section 5.4.1, ISL can start upstream of the dump plane, so is ISL stabilised flame in C2 and C3 where the flame is attached to the centre cone and origins from below the dump plane. The different flame shape is mainly caused by the the higher ϕ in C2 and C3 and hydrogen addition in C3 which increase the extinction stretch rate of the flame base. Hence, C2 and C3 flame can withstand higher hydrodynamic strain in the ISL and are likely to remain attached, compared to C1 flame. The flame lifting process is also closely related to the PVC structure: when the flame cannot withstand the local strain in the ISL, the flame detaches partially from the ISL which is then aided by a PVC structure until the formation of a detached M-shaped flame (Oberleithner et al. 2015). The flame lift-off process in the present work will be discussed in detail together with the coherent structure in Section 5.5.3. Besides, C2 and C3 present a blurry reaction

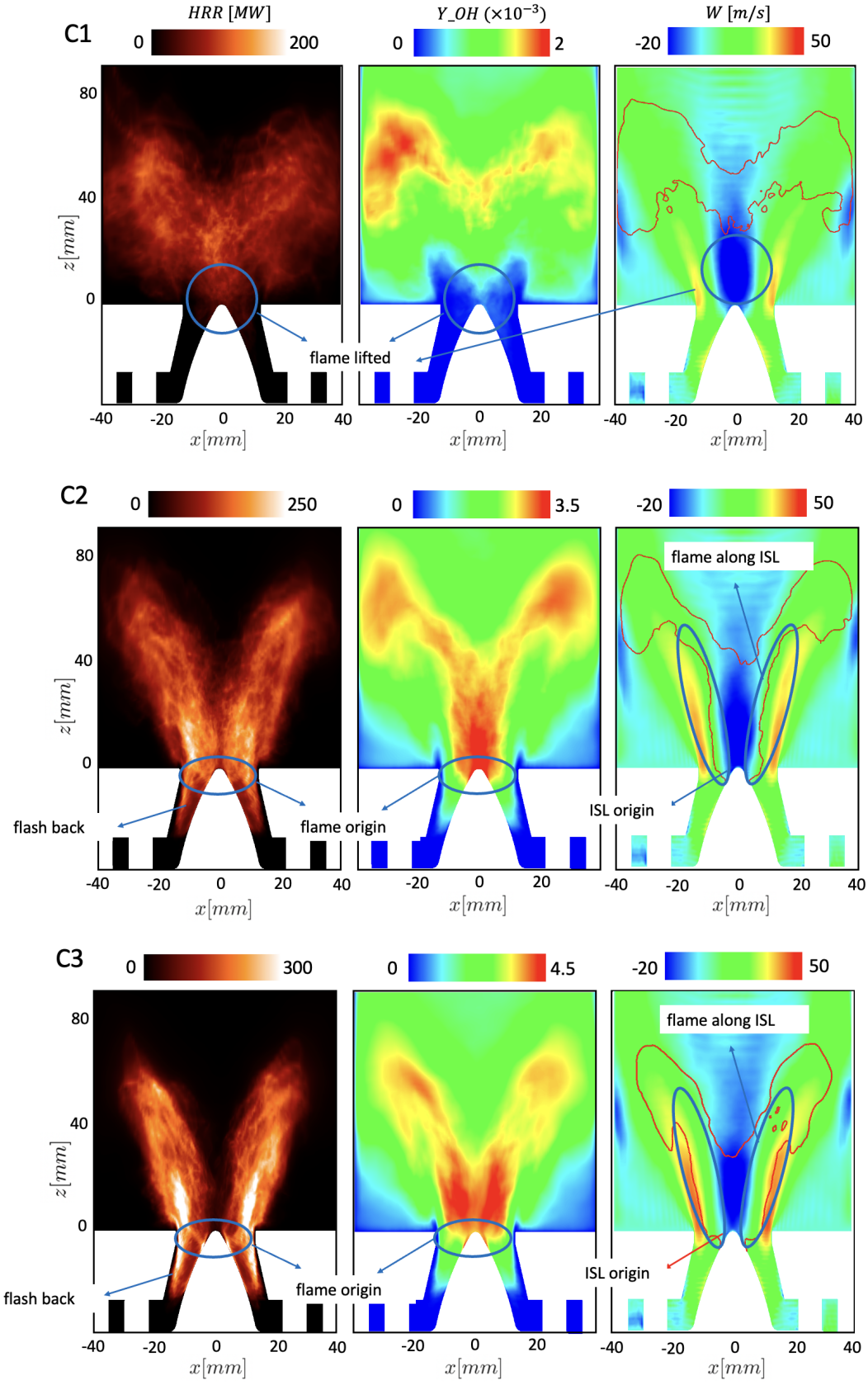

Figure 5.13: Time-averaged mid-plane images of HRR (left), Y_{OH} (middle), and W fields (right) for C1 (top), C2 (middle) and C3 (bottom). The W fields have overlaid on top by the contours of the mean binarised Y_{OH} images in red.

region in the upstream region in the nozzle in C2 and C3, which is absent in C1. This indicates the flame stabilisation location move in time during the observed strong thermo-acoustic oscillations. The flame flashbacks and other transient motions will be discussed further in Subsection 5.5.2. Another observation is the increasing HRR level from C1 to C3. For C1 and C2, the equivalence ratio ϕ increases from 0.65 to 0.85 leading to higher HRR in C2. For C2 and C3, despite the same ϕ, hydrogen enrichment results in a higher flame temperature and HRR due to the higher heat value of the fuel. Besides, with hydrogen addition, the flame becomes more compact and shorter in length, and stabilises closer to the combustor nozzle, which suggests a higher thermal loading to the combustor hardware. This is likely due to the increased flame speed, which enables the flame to stabilise in the regions with higher flow speed, i.e. the region close to the nozzle exit.

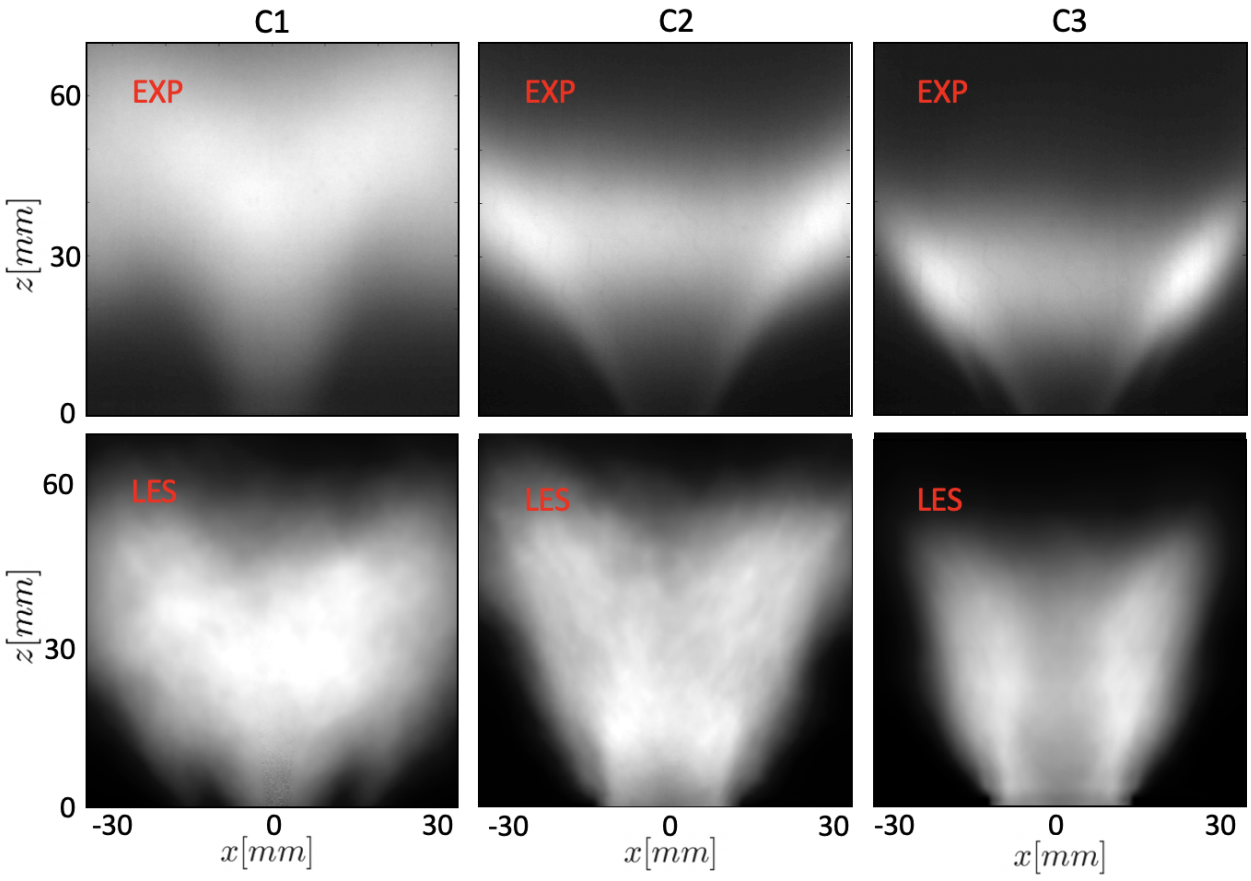

Figure 5.14: Experimental mean OH-CL images (top) compared to line-of-sight integration of the LES mean HRR for C1, C2 and C3.

Comparison with the measurements

Fig. 5.14 compares the simulated and measured mean flame topology. The measured averaged OH-CL images are compared with the line-of-sight integrated mean HRR in the LES. It can be observed that the flame form in each condition is well predicted in LES; an M shape lifted flame in C1 and a V shape flame in C2 and C3. The effect of hydrogen enrichment on shortening the flame and making it more compact which is found both in the LES and experiment. However, it can be found in Fig. 5.14, the most active region with the highest HRR signal exists in the region above $z = 30$ mm in C2 and above $z = 20$ mm in C3 in the experiment, while in the LES the flame is more active in the region close to the centre bluff body. Moreover in C2 and C3, the flame is found to be longer in the longitudinal direction and spread less in the transverse direction, compared to the OH-CL from the measurements. This is due to the coherent structures found in the LES, which interact with the ISL and significantly modify the flame stabilisation.

The flow fields are also significantly affected by the observed strong thermo-acoustic oscillations and hydrodynamic instabilities. Figure 5.15 and Fig. 5.16 show the radial profiles of the mean axial velocity W and the *rms* axial velocity rms_w for C1, C2 and C3 at the same downstream locations as presented in the non-reacting cases. For C1, the mean axial velocity magnitude and the jet spread angle are well-reproduced in the LES despite a slight over prediction of the jet velocity. However, in C2 and C3, the difference between the measurement and simulation is obvious: LES predicts a narrower jet and higher jet velocity, as well as a higher reverse flow velocity in the IRZ. The predicted *rms* velocities for the pulsating flames with the PRECCINSTA burner are checked numerically for the first time, which are shown in Fig. 5.16. In the experiments, the *rms* velocity in C1 is found to be the highest compared to those in C2 and C3, which is consistent with the thermo-acoustic features detected as discussed in Subsection 5.2. In LES, strong axial velocity fluctuations are found in all three cases, especially in C2 and C3 where rms_w can reach as high as 40 m/s. In each LES case, the IRZ exhibits the most violent fluctuations, followed by the jet region. The flows are not only subjected to turbulent fluctuations, but to the coherent structures and strong thermo-acoutisc oscillations, which all contribute to the high *rms* velocities in all reacting cases investigated. The difference between the predicted and measured flow field are consistent with the flame topology comparison as shown in

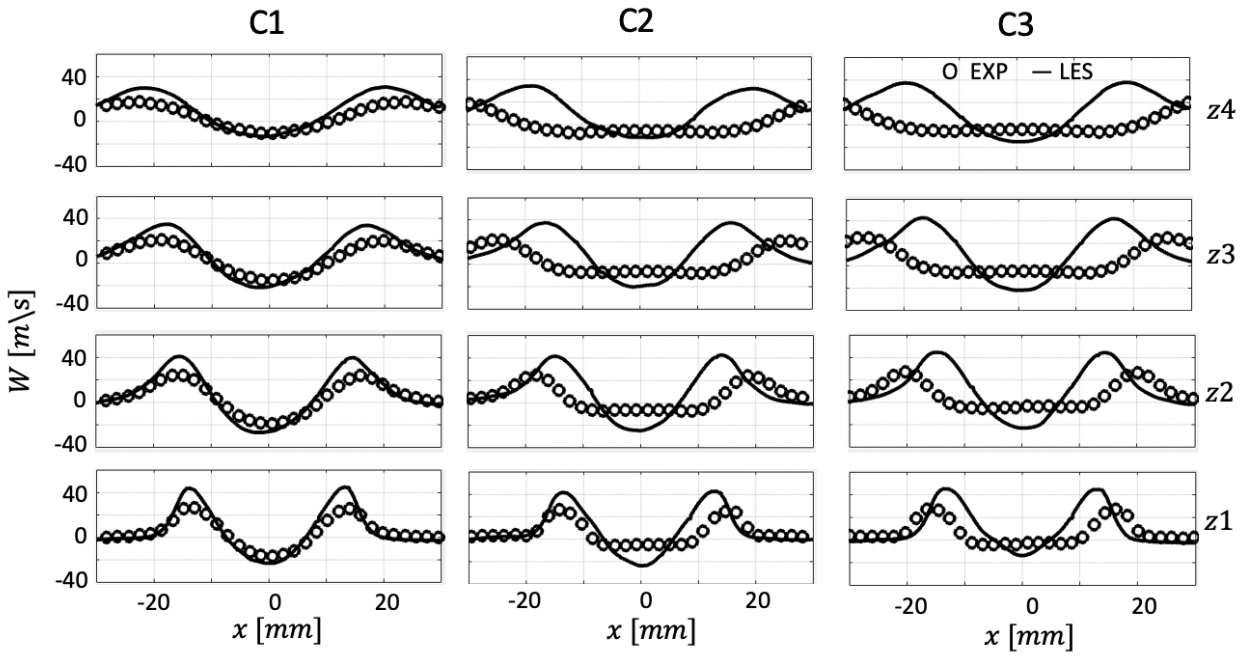

Figure 5.15: Comparison of the mean axial velocity W for C1, C2 and C3 at four downstream positions. - LES, ○ experiment.

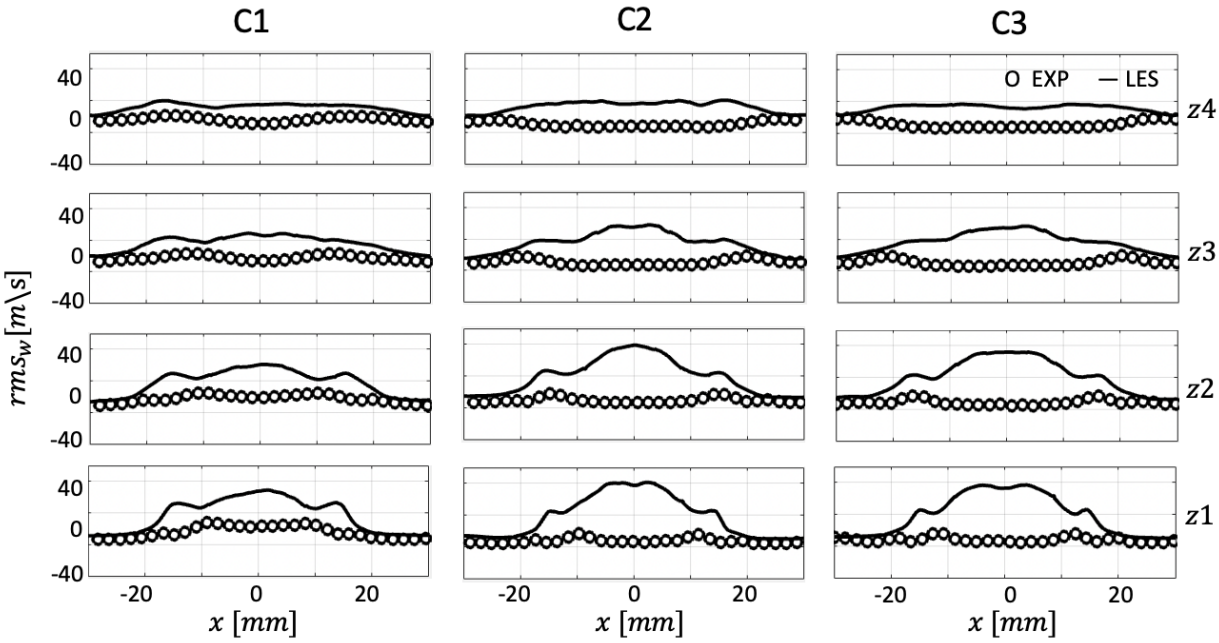

Figure 5.16: Comparison of the *rms* axial velocity rms_w for C1, C2 and C3 at four downstream positions. - LES, ○ experiment.

Fig.5.14, which are related to the flame dynamics and will discussed in the rest part of this chapter.

5.5.2 Thermo-acoustic instabilities

Strong flame oscillations are observed in the LES, which have significant impact on the flame topology and velocity moments as shown above. As is introcuded in Section 5.1, previous studies on the PRECCINSTA burner identified the main driving mechanism of the thermo-acoustic instabilities for this geometry is the convective coupling between the Helmholtz modes of the burner and the heat release via mass flow and equivalence ratio fluctuations (Meier et al. 2007, Franzelli et al. 2012). The air supply line has high acoustic impedance but the pressure in the large plenum volume responds to the acoustics resulting in air mass flow fluctuations. In the TP mode when air and fuel are injected separately, the high impedance of the fuel line leads to fuel accumulation in the swirler, creating equivalence ratio disturbances subject to the convective delay. A similar driving mechanism of the thermo-acoustic instabilities is detected in the currently investigated cases, with detailed discussions provided in this section.

Limit-cycle oscillations

The dynamic behaviour of the three cases are monitored using the signals of the pressure in the plenum p'_{pl}, chamber p'_{ch} and the axial velocity at the ISL probe w'_{ISL} as done already in the discussion of non-reacting cases. The air mass flow rate $\dot{m}_{tot}$ and fuel mass flow rate $\dot{m}_{fuel}$ at the dump plane are also monitored. In addition, the volume-integrated (or global) HRR in each case is monitored. In the system stability analysis, a widely used approach to determine whether the coupling between the acoustic field and the unsteady reaction rate leads to instability is the global Rayleigh criterion (Rayleigh 1878) defined as:

$$\frac{1}{T}\int_{\Omega}\int_{T} p'(x,t)\dot{q}'(x,t)d\Omega dt > 0 \tag{5.2}$$

where p' and $\dot{q}'$ are the local pressure and HRR fluctuations, and T and Ω are the time duration and volume of interest (flow domain in the current case). Eq. 5.2 states that the relative phasing of the

acoustic pressure and the HRR fluctuation would determine whether positive feedback exists in the thermo-acoustic cycle.

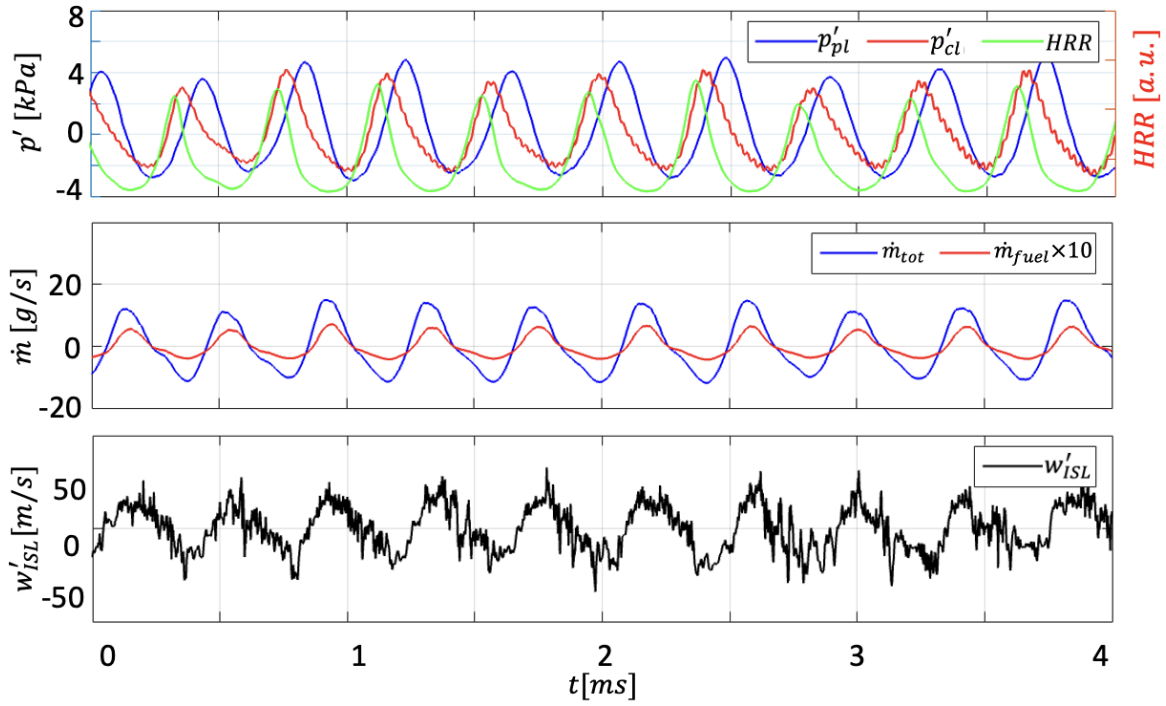

Figure 5.17: Temporal variations of the monitored signals in C1. Top: Global HRR and pressure fluctuations p'_{pl} and p'_{ch}. Medium: Mass flow rate fluctuations $\dot{m}_{tot}$ and $\dot{m}_{fuel}$ (scaled by a factor of 10). Bottom: Axial velocity w'_{ISL} fluctuations at Probe ISL.

Fig. 5.17 shows the signals of the pressure fluctuations of p'_{pl} and p'_{ch}, the HRR, the mass flow rates $\dot{m}_{tot}$ and $\dot{m}_{fuel}$, and the axial velocity at P2 of C1 (the probe positions can be found in the non-reacting case analysis in Section 5.4.3. A period of 4 ms contains about 10 oscillation cycles. It can be found that a period of 4 ms contains about 10 oscillation cycles during which all the signals oscillate with nearly constant amplitudes. The amplitudes of all the signals are nearly constant, indicating the state of zero growth rate of the acoustic energy: the acoustic energy source from the unsteady heat release and the acoustic energy losses are balanced (Poinsot & Veynante 2005). This is commonly referred to as limit-cycle oscillation and is controlled by a variety of complex, highly non-linear physical mechanisms are introduced in Chapter 1. Limit-cycle oscillations are also found in the C2 and C3 case, suggesting all three reacting cases in the LES are subject to thermo-acoustic instabilities. In contrast to the measurements where C3 is found to be stable, it appears that in LES this is still a very

strong positive coupling between the unsteady heat release and the acoustic fluctuations in C3.

Self-excited instabilities

Figure 5.18 compares the measured and computed PSD of the chamber pressure and HRR in all three cases. The duration and resolution of the signals are kept the same as those for the iso-thermal case. It is worth noting that in the experiments, the acoustic mode peaks are significantly damped and broadened by various effects including acoustic damping due to loosely mounted and not completely air-tight optical windows (Chterev & Boxx 2021). Hence, the flame is labeled as thermo-acoustically unstable if there is a distinct peak in the heat release spectrum. During self-excited thermo-acoustic instabilities, one or more acoustic modes can be excited and the heat release may couple to one or more of these modes.

In C1 for the experiment p'_{ch} and HRR spectra, the highest PSD is found at a frequency of around 224 Hz, which represents the dominant thermo-acoustic oscillations. The second peak at about the first harmonic frequency of 449 Hz is detected, which is also found in the HRR PSD, indicating its thermo-acoustic nature. In LES, these two thermo-acoustic modes are also found at around 240 Hz and 480 Hz respectively, with additional harmonics at multiples of the dominant mode frequency. The peak amplitudes measured to be 132 dB and 116 dB, respectively, are denoted by the blue star marks. As discussed in Section 5.1 in a recent study by (Lourier et al. 2017), the loosely mounted quartz windows used in the experiment as the chamber side walls have been found to cause acoustic damping on the chamber pressure PSD by about 10 dB with the frequencies unaltered. With this estimation, the two dominant mode peaks are marked by red stars and good agreements are achieved in the predicted and measured peak amplitudes (within 3 dB difference).

In the PSD of the experiment p'_{ch} in C2 there are also two dominant modes, with the frequencies of 303 Hz and 607 Hz respectively; in the PSD of the experiment HRR, only the first mode is detected, indicating the thermo-acoustic nature of this dominant mode. In the LES, the frequencies of these two modes are predicted to be 305 Hz and 610 Hz, which are in excellent agreement with the measured ones. As for the PSD of HRR, a dominant peak at the first mode frequency is found, with harmonics

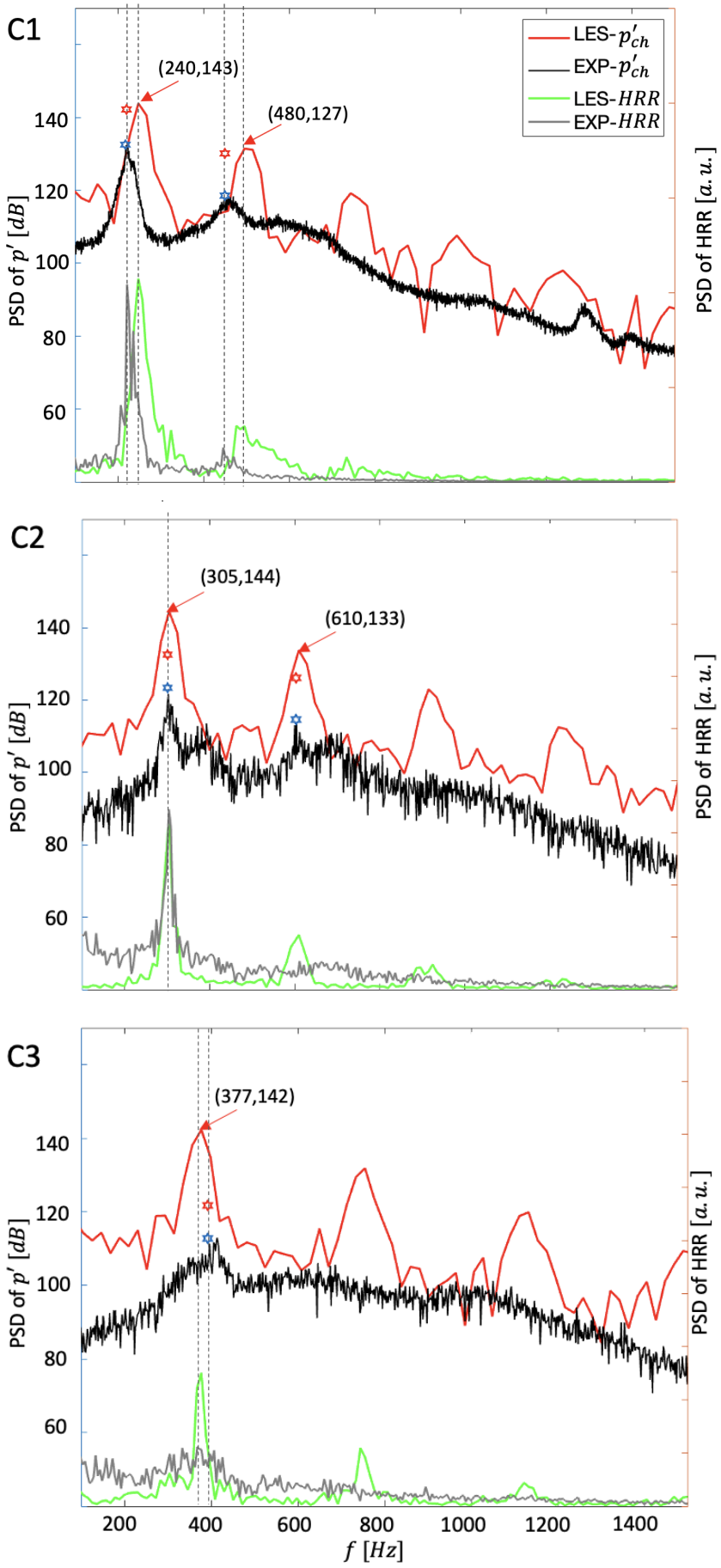

Figure 5.18: PSD comparison of the chamber pressure and integrated HRR in C1, C2 and C3.

existing at its multiples (610 Hz and 915 Hz etc). Over predictions are found for the amplitudes by about 10 dB for the first and second peaks in p'_{ch} PSD with the estimated damping effect taken into account. The discrepancies become more pronounced in C3 case, where the dominant peak is found to be an acoustic mode in the experiment but a thermo-acoustic mode in the LES. That is, in C3 the HRR fluctuations are coupled with the acoustic fluctuations in the LES, which is not found in the experiment. Besides, an under-estimation of about 22 Hz of the acoustic frequency is found in the LES.

These thermo-acoustic instabilities are highly impacted by thermal boundary and initial conditions. In general, the thermo-acoustic frequency is determined by the natural frequency of the active acoustic mode of the system, which is related to the geometry and speed of sound(Chterev & Boxx 2021). The geometry is kept unchanged in the current study leaving the speed of sound the key parameter, which is closely related to the temperature field. As discussed in Section 5.3, the wall temperature and the inlet air temperature are fixed according to the available measurements, which are the same for all three cases. However, these temperatures should definitely change across cases with different heat release distributions in the burner with different flame topology. Figure 5.19(a) compares the time-averaged temperature field of C1 and C3, and (b) the corresponding radial profiles along the bottom of the burner at $z = 0.5$ mm and two upstream positions in the nozzle at $z = -4$ mm and $z = -15$ mm. Due to the axial symmetry, only half of the profiles are presented. It can be found that the temperature field presents significant difference in the two cases: in C1 when the flame is lifted, the temperature in the region near the bluff body is around 800 K, which reduces gradually towards upstream and reaches about 320 K at $z = -15$ mm; while for the attached V-flame in C3, a temperature ~ 2000 K is reached near the centre cone tip on the internal side. This is not unexpected, as high value of OH mass fraction is found in the region just downstream of the center body tip in C2 and C3 as shown in Fig. 5.13. The region in the upstream nozzle is also greatly heated in C3 which is related to the flame flashbacks. Hence it can be expected, the different flame structures lead to differences in the solid wall temperatures especially for the centre body , which make the same prescribed wall temperatures in all cases not accurate.

The slight miss-match of the measured and predicted acoustic frequencies are closely related to these

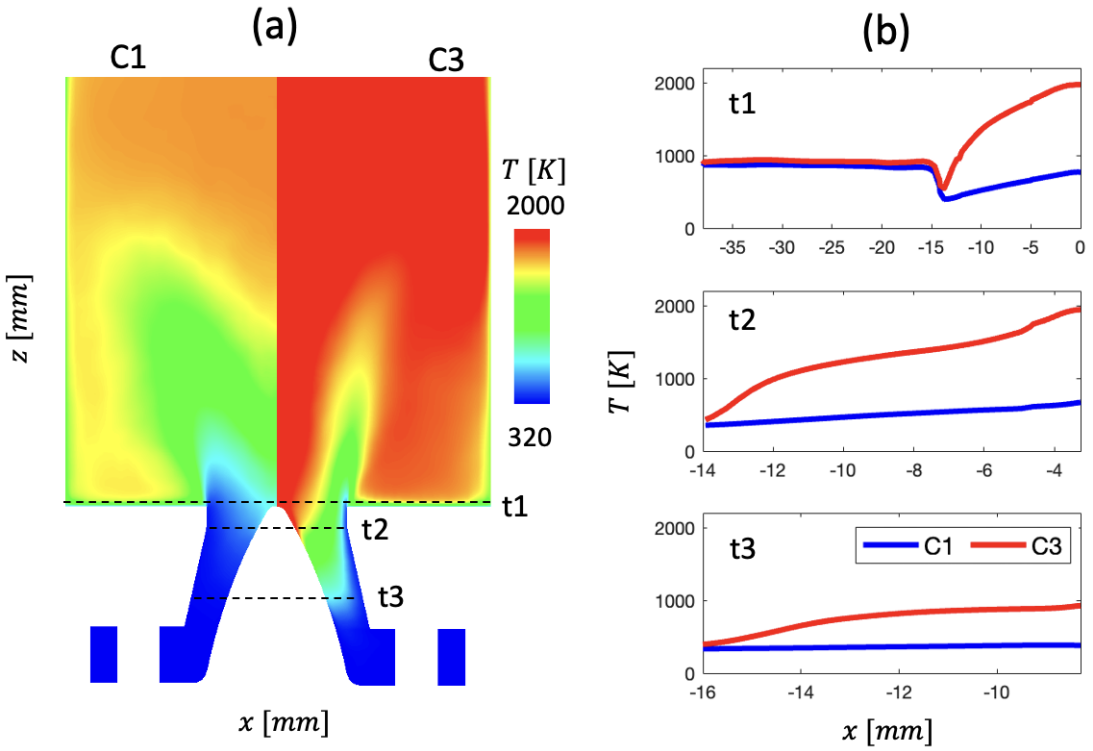

Figure 5.19: (a) Mid-plane contour of the predicted time-averaged temperature field in C1 and C3. (b) Comparison of the temperature profiles.

imposed thermal boundaries. This various near wall temperature fields shown above would definitely lead to different wall temperatures, which in turn, control the heat transfer between the flow and the solid walls and as a result, affect the preheated temperature of the inlet gas (instead of being fixed at 320K in all cases). These changes in the temperature field modify the local speed of sound (Poinsot 2017), which affects the acoustic frequency directly. The preheated gas temperature also affects the laminar flame speed, thereby influences the flame topology and anchoring position, which is also directly related to the wall-heat transfer, adding to the complexity of the problem.

The over-estimation of the fluctuation amplitudes and the thermo-acoustic instabilities found in LES for C3 involves more complex reasons. One possible reason is acoustic damping, and as discussed by Lourier et al. (2017), the main contributor to damping is the losses of acoustic energy at the boundaries of the system. The previous estimation of the damping effect of the quartz windows is achieved for the oscillating flame by (Meier et al. 2007) which features an M shape and resembles the C1 flame. However, C2 and C3 exhibit different flame configurations and dynamic features, and the effect of

the acoustic damping caused by the quartz windows remains unclear. In LES, the outlet boundary conditions are treated with the NSCBC formulation as discussed in Section2.4 with a prescribed fix pressure relaxation factor α based on the optimal value found in previous work. This coefficient control the 'stiffness' of the boundary which are unknown and may explain LES/EXP discrepancies. Hence to better represent the acoustic impedance at the exit of the combustion chamber, in a separate study the atmosphere is included in the computational domain with a large extended domain, which is shown in Fig. 5.20. However, despite a slight reduce in the pressure amplitude, this does not suppress the observed thermo-acoustic mode. Hence an underestimation of the acoustic damping may not be the reason for the thermo-acoustic oscillations observed in the LES.

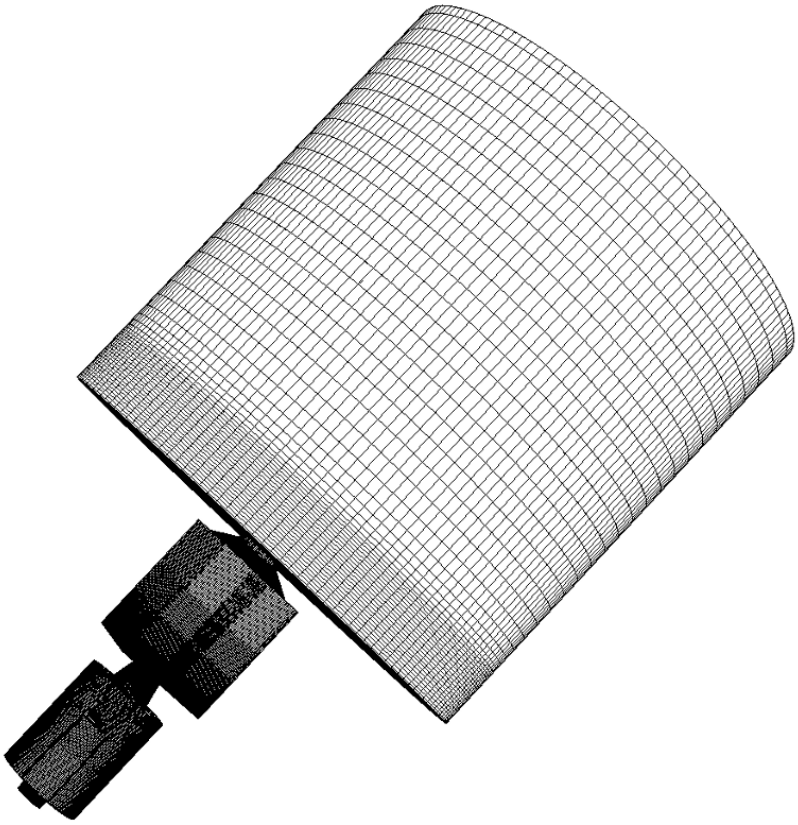

Figure 5.20: Computational mesh including the atmosphere with extended downstream domain.

The second and more important reason is again related to the fixed wall temperature as the thermal boundary conditions. In a recent LES study on the impact of wall heat transfer on flame dynamic in the PRECCINSTA burner by Agostinelli et al. (2021), the simulation using isothermal boundary

condition with fixed wall temperatures was found to predict thermo-acoustic oscillations which are not observed experimentally. The numerically predicted instabilities were found to be supported by equivalence ratio fluctuations caused by fuel pockets periodically pushed into the chamber, and could not be suppressed by changing the acoustic impedance of the inlet boundary conditions. Instead they found, with the conjugate heat transfer (CHT) approach where the wall temperature was solved and coupled to the flow computation, the flame response to the disturbances were slightly but sufficiently modified and the flame was found to be stable as in the experiments. Improvement in the prediction of combustion instabilities with the CHT method have also been claimed by Kraus et al. (2018) recently in an LES study of a swirling flame, where the frequency and amplitude of the oscillations were better predicted due to the better computed preheating temperature of the gases in the plenum.

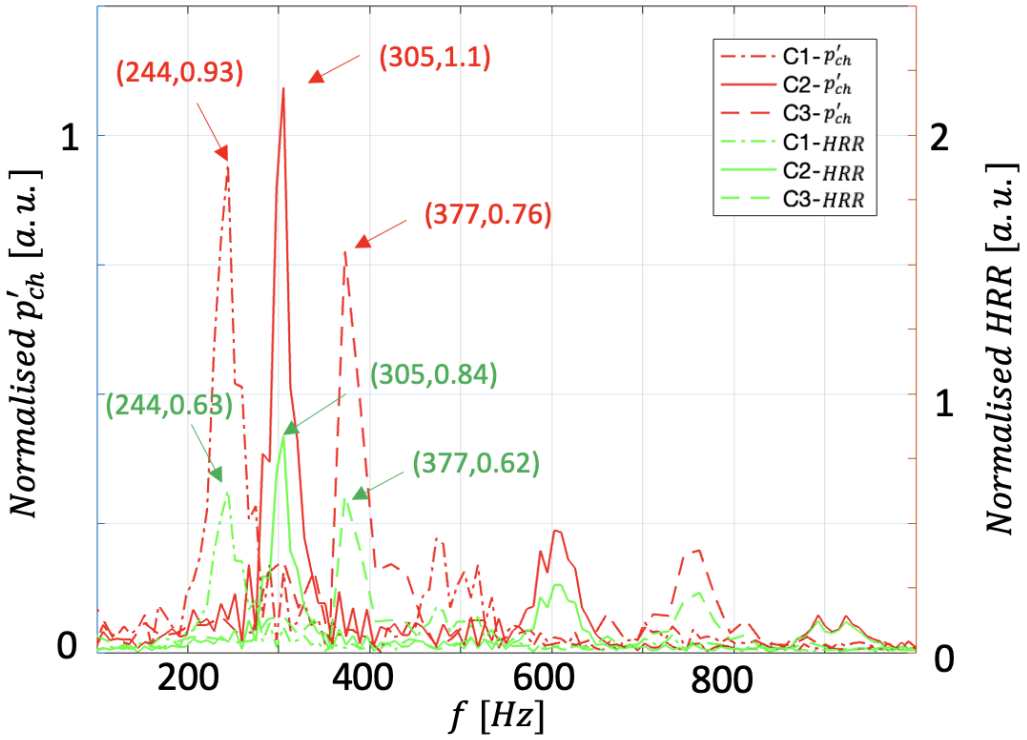

Figure 5.21: Power spectra of the predicted chamber pressure and heat release rate in C1, C2 and C3. Amplitudes are shown in normalised values.

Figure 5.21 further compares the predicted thermo-acoustic modes in C1, C2 and C3, in order to show the effect of increasing equivalence ratio and hydrogen addition. When comparing C1 and C2, where ϕ increases from 0.65 to 0.85 with a slight shift of the thermal power, the dominant frequency increases in the LES. C2 predicts higher peak amplitude than C1, which contrasts the experiment

results as shown in Fig. 5.18. This is due to different flame shape (hence HRR distribution) and HRR level, resulting in significant differences in heat transfer distributions to the combustion hardware (centre body, combustor liner, dump plane) (Chterev et al. 2014). In V-shape flames with the flame root attached to the center body tip, the regions where the flame tips reach the wall are very hot as shown in Fig. 5.19; while in reality and in the CHT study by Agostinelli et al. (2021), the temperature field and hence the sound speed in that region are more homogeneous due to the heat conduction in the solid, and a globally lower sound speed is found. This non-homogeneous heat transfer with fixed wall-temperature was found to have be closely related to the numerically predicted thermo-acoustic instabilities (Agostinelli et al. 2021), which is less significant in the M-shape C1 flame where the flame is lifted and the temperature field in the region near the centre body is already more homogeneous.

The effect of H_2 addition under the condition $\phi = 0.85$ and $p_{th} = 22.8$ kW is shown when comparing C2 and C3. As shown before the $c = \sqrt{\gamma RT}$, H_2 enrichment increases the flow temperature, leading to a higher speed of sound and a higher thermo-acoustic frequency in C3 compared to C2. Moreover, with more H_2 in the fuel, the there will be more H_2O in the hot product in which acoustic wave propagates faster compared in CO_2 due to a smaller molar mass. Besides, as shown in Fig. 5.21, H_2 addition decreases the acoustic and the HRR peak amplitude by about 30%. This trend is in good agreement with the experiment findings that the H_2 addition damps the acoustic fluctuations under these conditions. This is closely related to the driving mechanism of the thermo-acoustic instabilies in the present work (details shown in next subsection). As introduced in the beginning of this subsection, the convective delay between the this equivalence ratio disturbance being created and reaching the flame determines the phase difference between the acoustic oscillations and HRR oscillations, which according to the Rayleigh criterion, determines the coupling between the acoustic and HRR oscillation, e.g. phases difference must be within 90° for a thermo-acoustically unstable system, and a smaller value leads to a stronger coupling. This time delay is a function of parameters such as flame stand-off location, flame length and speed of sound (Chterev et al. 2014). As discussed in the recent experimental work by (Chterev & Boxx 2021), H_2 enrichment was found to increase the phase delay between the pressure and heat release at the flame location. This is caused by decreasing the pressure wave travel times in the plenum and swirler sections of the burner and by decreasing the flame length while simultaneously increasing the pressure wave speed within the burner, and the balance

between the thermo-acoustic period and the total travel time to the flame leads to a longer phase delay). Hence, according to the Rayleigh criterion, thermo-acoustic amplitude is decreased in C3 when the initial phase delay is positive in C2.

Thermo-acoustic feedback loop

The driving mechanism and feedback loop of the thermo-acoustic instabilities are discussed in this subsection, together with the temporal evolution of the flow and reaction field. Figure 5.22 compares the phase-resolved p'_{pl}, p'_{ch} and the integrated HRR in a full period of oscillation in C1, C2 and C3. The pressure drop between p'_{pl} and p'_{ch} is computed as $p_{diff} = p'_{pl} - p'_{ch}$ and plotted in Fig. 5.22(b) together with $\dot{m}_{tot}$ and $\dot{m}_{fuel}$ simultaneously. These mass flow rates are evaluated in the dump plane at $z = 0$ mm. The equivalence ratio of the unburned gas ϕ_{ch} is computed according to $\dot{m}_{tot}$ and $\dot{m}_{fuel}$ and present for the interval when $\dot{m}_{tot}$ is positive in Fig. 5.22(c). It is worth noting when the flame flashbacks with the thermo-acoustic oscillations as shown in Fig. 5.23, the equivalence ratio of the reactant mixture can not be evaluated at the $z = 0$ mm plane. Hence instead, ϕ_{ch} is computed as the plane $z = -15mm$ to monitor the fuel accumulation effect in all cases.

$\theta = 0^\circ$ is defined at the maximum of the HRR, which is used throughout the rest of the analysis for the reacting cases. The corresponding flows evoluations are shown in Fig. 5.24 with the instantaneous axial velocity, mixture fraction and HRR at different phases angle from $\theta = 0^\circ$ to $\theta = 360^\circ$. Several observations can be made when comparing these signals. First, as shown in Fig. 5.22(a),the phase difference between the p'_{ch} and p'_{pl} peaks in the three cases are roughly 56°, 59° and 63° respectively, corresponding to a propagation time delay of 0.65 s, 0.55 s and 0.51 s. With the fixed positions of the acoustic probes, this decline in the convective time delay is mainly due to the increasing propagation speed of the acoustic wave from C1 to C3. As a consequence of the acoustic wave propagation, pressure drop p_{diff} fluctuates periodically, leading to fluctuating mass flow rates as shown in Fig. 5.22(b). A phase lag between the peak of $\dot{m}_{tot}$ and $\dot{m}_{fuel}$ can be found, which reduces from 31° in C1 to 14° in C3. This phase lag is mainly caused by the different acoustic impedances of the fuel and air supply lines, which lead to the fuel accumulation in the swirler unit. The resulting ϕ_{ch} fluctuates periodically in all three cases, as shown in Fig. 5.22(c). It can be found, in C1 $\dot{m}_{fuel}$ as well as ϕ_{ch} exhibits a

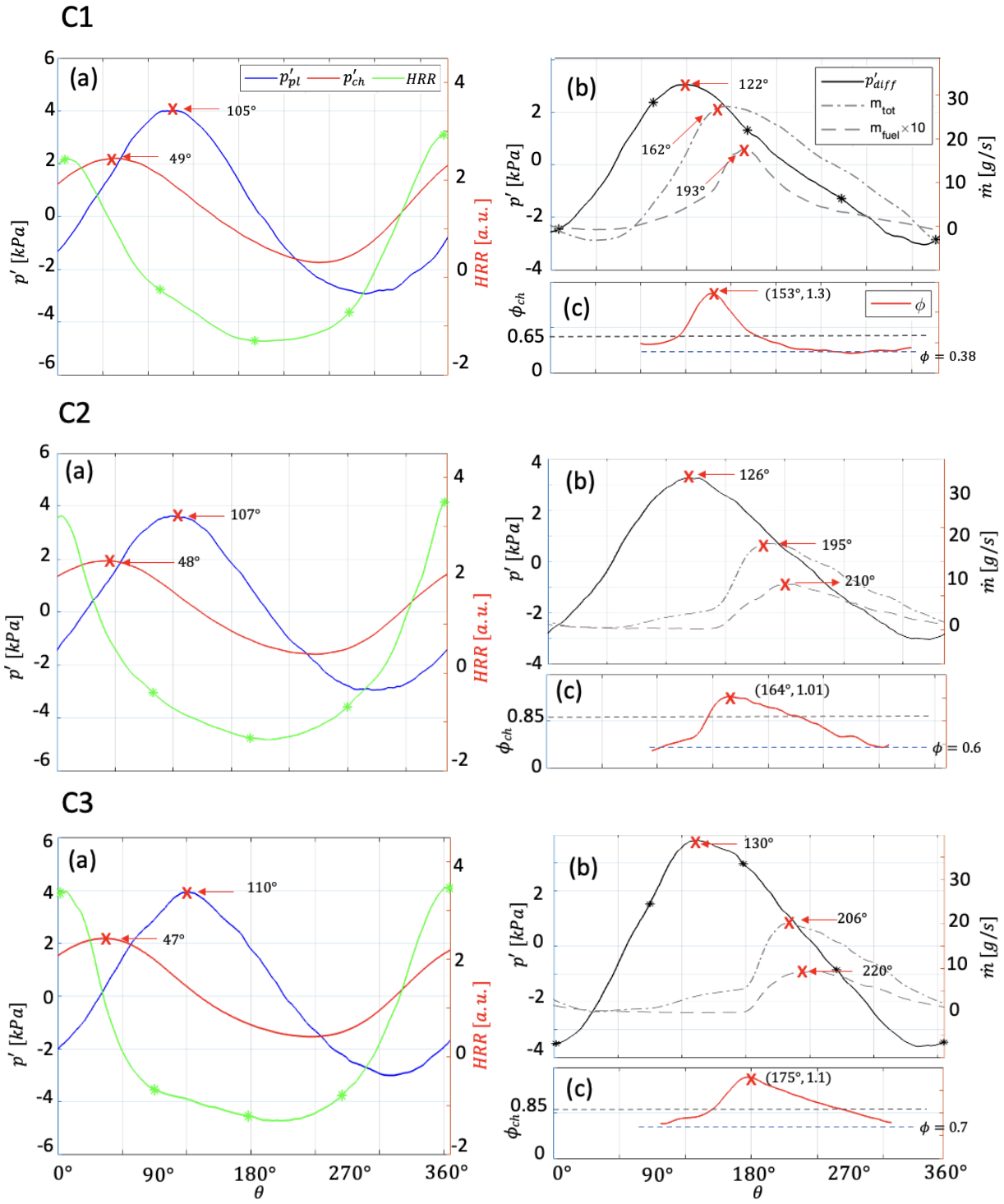

Figure 5.22: Temporal signal evolution in a full acoustic cycle for C1, C2 and C3: (a) Air plenum pressure p'_{pl}, chamber pressure p'_{ch} and integrated HRR. (b) Pressure difference p_{diff} between p'_{pl} and p'_{ch} and mass flow rates $\dot{m}_{tot}$ and $\dot{m}_{fuel}$ in the same cycle. (c) Equivalence ratio of the unburned gas entering the chamber.

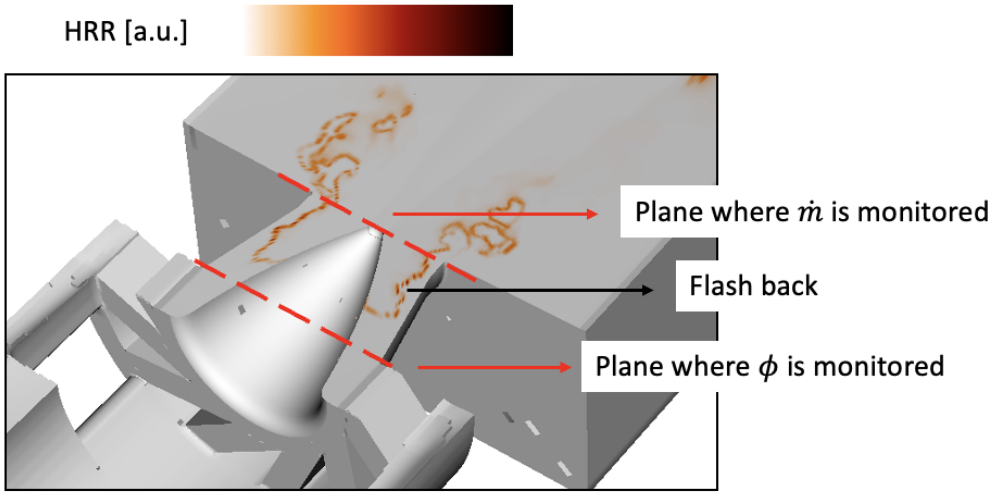

Figure 5.23: Flame flashback and planes on which mass flow rate and equivalence ratio are monitored.

rapid growth and decline, while in C2 and C3 $\dot{m}_{fuel}$ and ϕ_{ch} drop mildly in a similar way as the total mass flow rate $\dot{m}_{tot}$. ϕ_{ch} in C1 fluctuates between a wide range from 0.38 to 1.3 (over $\Delta\phi_{ch} = 0.92$), while this range difference reduces to $\Delta\phi_{ch} = 0.4$ in in C2 and C3. This indicates that in C1 fuel accumulation has a distinct and more pronounced effect, while in C2 and C3 the system is affected more by velocity fluctuations. Besides, the mass flow rates in C2 and C3 exhibits a nearly constant level, before a sudden increase at around 180°. This is caused by the violent flash back of the flame in C2 and C3 as can be seen in Fig. 5.24 at $90° - 135°$ for C2 and C3. As a consequence, the reactant mixture is consumed before reaching the $z = 0$ mm plane.

Fig. 5.24 shows the instantaneous axial velocity and mixture fraction at different phases from 0° to 360°. Iso-contours of a constant-value HRR are overlapped on top to show the flame region in the chamber. In the swirler inlet region, the slices are taken along the passage in order to show the flow locally as illustrated in Fig. 5.24 on the top. In C1 at 0° when the HRR reaches its maximum, the local high HRR generates pressure disturbances (acting like an acoustic source). Due to the propagation delay, p'_{ch} increases ahead of p'_{pl}, and hence p_{diff} has a negative value, leading to the drop of w in the nozzle and thereby less supply of fresh reactants into the flame region. Hence the HRR drops afterwards (0° to 180°). With the increase of p'_{pl}, p_{diff} grows and turns positive at around $\theta = 60°$, after which the axial velocity in the nozzle begins to increase (135° to 180°). The velocity within

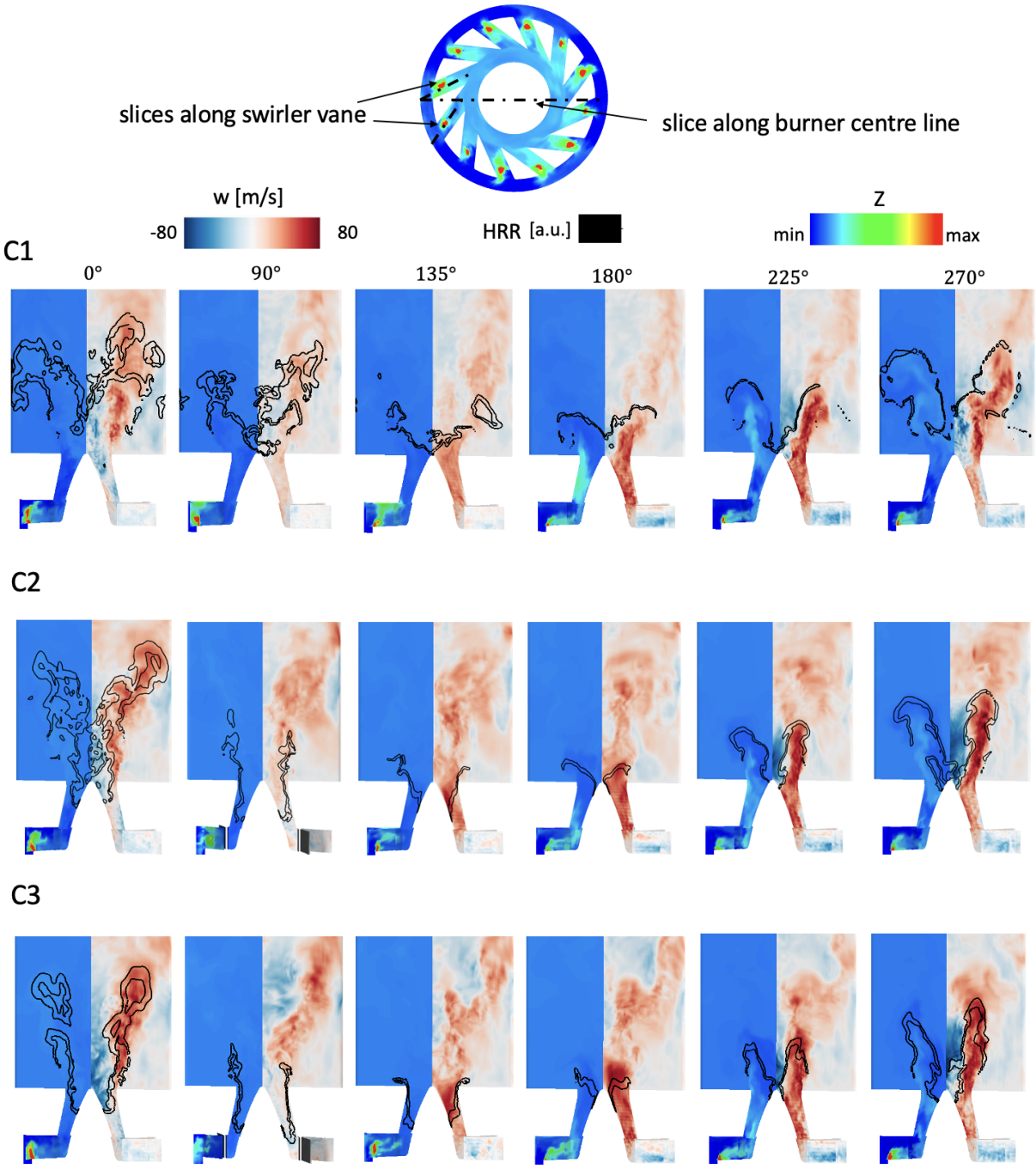

Figure 5.24: Periodic evolution of the flow in C1, C2 and C3 at six phases from $\theta = 0°$ to $\theta = 360°$: Left: Mixture fraction; Right: Instantaneous axial velocity. Iso-contours of instantaneous HRR are overlapped on top to show the flame topology.

the fuel channels where fuel is injected into the swirler, by contrast, remains relatively constant due to the high impedance at the fuel inlet. A significant amount of fuel accumulates within the swirler (90° to 135°) when the nozzle velocity is declining. When the axial velocity grows, the fuel-rich pockets of gas are convected downstream and reach the chamber inlet at around 180°. With these large quantities of reactants transferred into the reaction region, combustion is greatly enhanced as shown by the climbing HRR at 270°, which continues to increase until the next maximum is reached when the feedback loop is closed.

A similar oscillation behaviour is found in C2 and C3, with some notable differences. When the flame flashes back (90°), in C1 the flame reaches the tip of the nozzle, while in C2 it extends into the centrebody half way and in C3 is even further upstream. This is mainly caused by the increasing flame speed from C1 to C3. Besides, the flame in C2 and C3 remains attached to the centre body throughout the cycle, while the flame is lifted off in a fairly long range in the C1 cycle. The flame lift-off is closely related to the dynamic hydro-dynamic structure in the flow and will be discussed in detail in the following section.

In summary, a combination of mass flow rate fluctuations and equivalence ratio fluctuations is identified as the dominant feedback mechanism for the thermo-acoustic fluctuations in all three cases. The flame experiences violent, periodic oscillations in the axial direction, correlated with the thermo-acoustic fluctuations. A similar oscillating behaviour of the flame was reported in the experimental work by Temme et al. (2014) where a swirl-stabilised, liquid fuel gas turbine combustor featured strong self-excited combustion instabilities driven by a comparable equivalence ratio oscillation mechanism. Tachibana et al. (2015) also identified periodical flame flashback into the pre-mixing annulus passage in a liquid-fuel aero-engine combustor both experimentally and numerically, as a result of different responses of the fuel and air flow rates to the pressure fluctuations. In the recent LES study by Fredrich et al. (2021*a*) of the F2 flame periodic flame lift-off and flashback were reported together with fuel supply oscillations in the system.

5.5.3 Hydrodynamic instabilities

In this subsection, the hydrodynamic instabilities resulting from flame-vortex interaction are investigated. The formation and evolution of the vortical structures, and their potential impact on the flame are also discussed.

Swirl number fluctuation

Periodic excitation and suppression of large-scale vortical structures have been detected in all three cases. This is linked to the transient interaction between the swirler and the strong acoustic fluctuations.

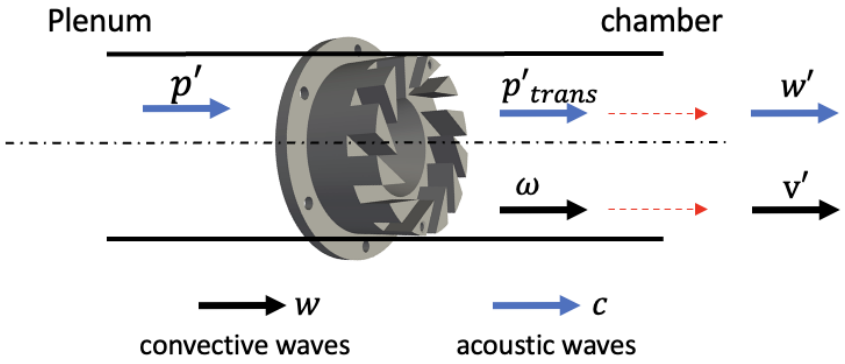

Figure 5.25: The interaction between the swirler and incident acoustic perturbations. The blues arrows represent the acoustic waves propagating at the speed of sound c, and the black arrows denote the jet flow rate at which the vorticity waves travel downstream.

The mechanism describing the interaction between the swirler and incident acoustic perturbations was characterised analytically by Palies et al. (2010). As illustrated in Fig.5.25 when a swirler unit is impinged by acoustic waves under low Mach number conditions, axial (w') and azimuthal (v') velocity perturbations are induced. v' is found to have the same order of magnitude as the incoming acoustic disturbance (Palies et al. 2010), and is caused by vorticity waves (ω) generated at the trailing edge of the swirler blades which is subject to a mode conversion process (Cumpsty et al. 1977, Komarek & Polifke 2010). The vorticity wave has a convective nature and propagates downstream at the bulk

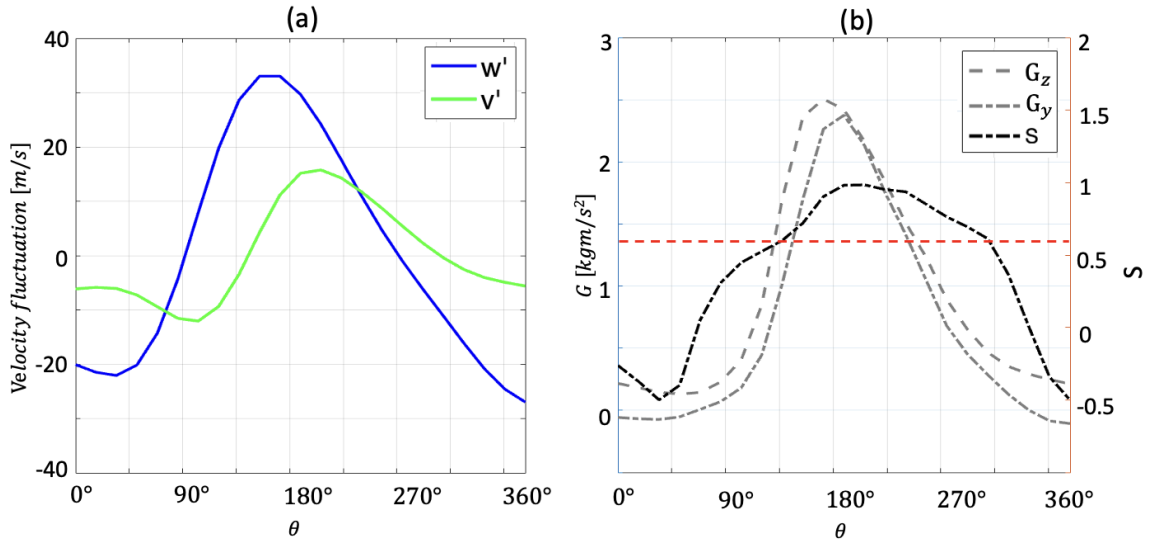

Figure 5.26: Spatially integrated variables at the dump plane in C1. (a) axial (w') and azimuthal velocity fluctuation (v'). (b) axial and azimuthal momentum flow rate (G_z and G_y) and the corresponding swirl number (S) oscillations.

flow velocity. These velocities waves impact the sysytem mainly in two ways: the axial velocity fluctuations solely can generate toroidal vortices at the dump plane, rolling up the flame surface and therehby modulating the overall HRR in the burner; the combined effect of the axial and azimuthal velocities fluctuations gives rise to the fluctuations of the swirl number. The swirl number controls the motion and strength of the IRZ, modifies the flame spreading angle and the distance between the nozzle and the flame front, and controls the formation, geometry and frequency of the PVC , hence having a significant impact on the flame dynamics. Periodic PVC deformation was reported experimentally by Caux-Brisebois et al. (2014) in a PP PRECCINSTA flame, and was identified to be induced by swirl number fluctuations at the thermo-acoustic frequency. Fredrich et al. (2021*a*) first identified a periodic excitation and suppression of a PVC and flame angle oscillations induced by the swirl number fluctuations in the F2 flame, which were found to be directly linked to the dominant thermo-acoustic mode.

Temporal evolution of vortical structures

A PVC structure is observed with both M- and V-shape flames in C1 to C3. The PVC existence was found to be strongly dependent on the density gradient in the maker region (the separating ISL from

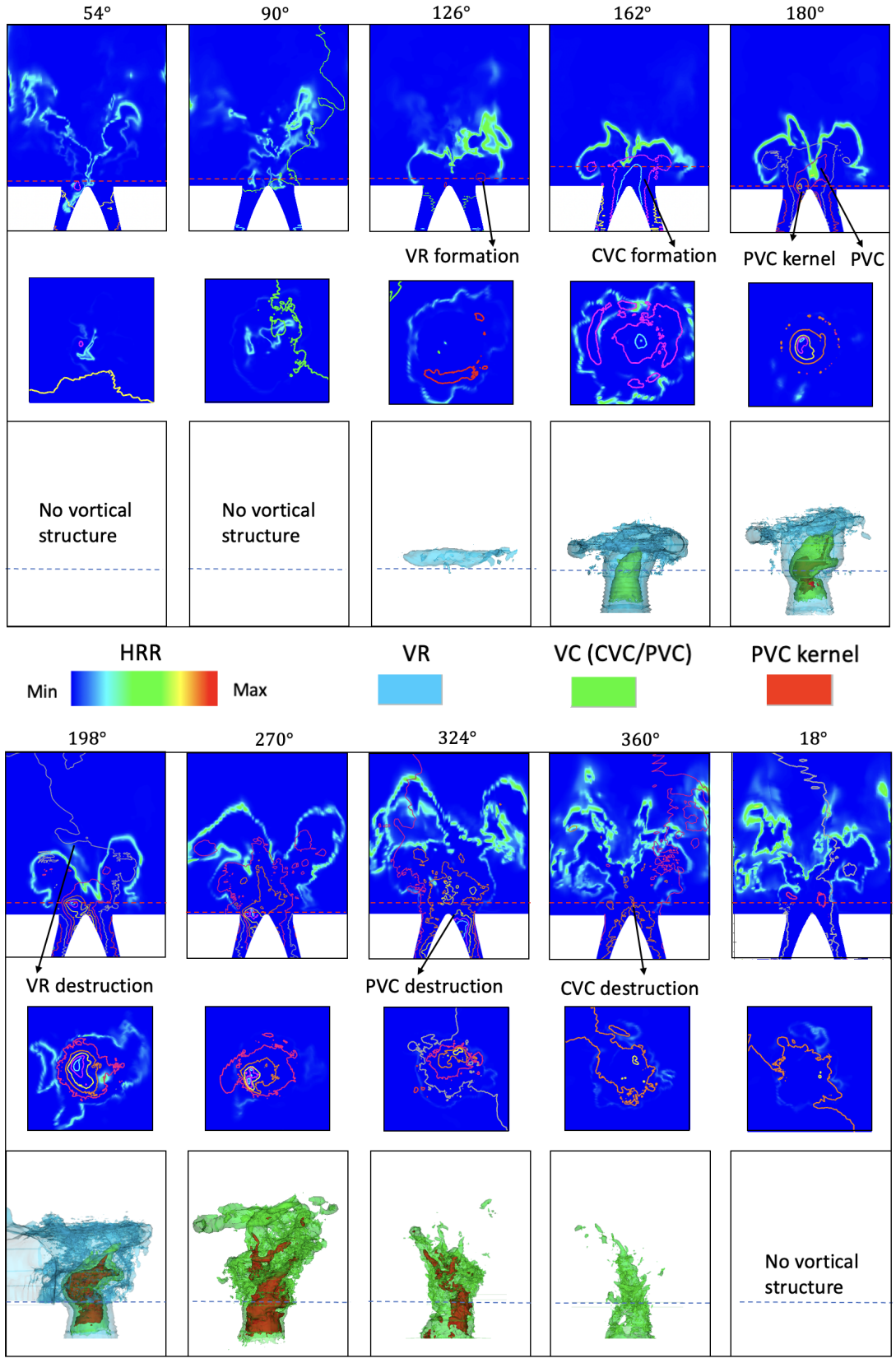

Figure 5.27: Temporal evolution of vortical structures and their impact on the flame in C1. Planar HRR field overlapped with pressure contours on a longitudinal plane (top) and a transverse plane (middle). Bottom: Contours of iso-surfaces of low pressure values indicating different large scale structures.

the center cone) (Oberleithner et al. 2015), which is hence closely related to the heat transfer at the centre body surface and the preheated air temperature. In previous studies with the PRECCINSTA burner, the PVC was found only in the M-flame (Steinberg et al. 2011, Oberleithner et al. 2015). In the recent experiments by Chterev & Boxx (2021) with elevated pressure and preheated air from 613K to 663K, PVC structure existed in all reacting cases with M- and V-flames.

Figure 5.26(a) shows the axial (w') and azimuthal (v') velocity fluctuation in one acoustic cycle in C1. The amplitude of the v' wave is about half of the w' wave, with a phase lag of $\sim 33^\circ$ corresponding to 0.4 ms. This phase lag together with the different wave amplitude leads to fluctuating momentum flow rates G_z and G_y, and hence a fluctuating swirl number S as computed by Eq. 5.1, which are shown in Fig. 5.26(b). The resulting flow field evolution is shown in Fig. 5.27. Longitudinal and transverse planes of HRR field are visualised which are overlapped with pressure contours to show the interaction of the flame and the vortical structures. The red dashed lines in the longitudinal planes mark the position of the transverse planes. On the bottom, the 3D vortical structures are shown by different levels of low-value pressure iso-surfaces: blue contours are for the vortex ring (VR); green contours describes the vortex cores (VC) and the edge of the PVC; red contours represents the kernel (core) of the PVC with a lower pressure.

From 0° to 108°, G_z and G_y are both low due to a low mass flow rate $\dot{m}_{tot}$, and no distinct hydrodynamic structures exist in the field. At 126°, a vortex ring forms at the outer rim of the nozzle at the chamber inlet as a results of the increased G_z, which is convected downstream along the OSL before breaking down from 162° and vanishing afterwards. As the swirl number S grows, a central vortex core (CVC) is excited at around 162° as a result of the rapidly increasing azimuthal and axial velocities. A PVC with a single helix is then excited along the ISL with a high instantaneous S at 180°, leading to a characteristic deformation of the IRZ and the jet. The PVC rotates anti-clockwise from the top view while precessing clockwise and continuously growing in size from 180° to 270°. The resulting flow field and flame topology show great asymmetry, and the flame is lifted off when the PVC is excited (198° to 360°), which will be discussed further in the following section. It is difficult to identify the specific event that triggers the formation of the PVC since the flow is at the border of instability and thus even minor turbulent fluctuations of velocity or density may initiate the

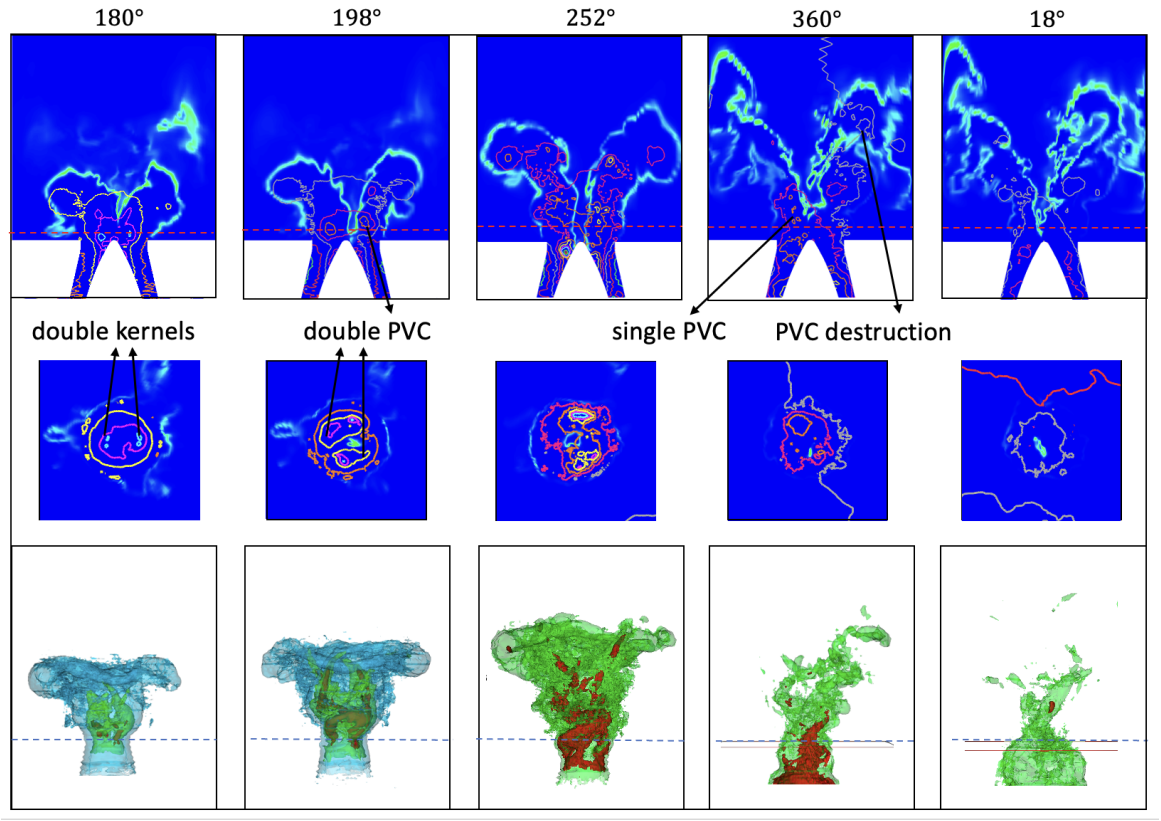

Figure 5.28: A double PVC cycle in C1.

formation. The single helix starts to break down when S drops and finally disappears at the end of the cycle. The existence of the PVC is determined by the instantaneous swirl number and is found to exist when the S is higher than a critical value as $S > 0.6$ (Chigier & Chervinsky 1967). This critical value for S for the current work is not examined for the PVC evolution in the current work, however it can be readily found from Fig. 5.26(b) and the temporal field evolution that the CVC is excited at around 162° where S is very close to the value 0.6 as mark by a red dashed line in Fig. 5.26(b) This periodic evolution of the vorticies is observed in every thermo-acoustic cycle, strongly coupled with the dominant thermo-acoustic mode.

The single helix PVC discussed above is observed to be the most common structure in C1, and is most often present in each cycle. However, a secondary PVC with double helices is also detected in some of the cycles, which is shown in Fig. 5.28. The corresponding swirl number S fluctuations do not show a distinct difference to the one during a single helix evolution, and the excitation of this double helical structure occurs in a random manner. Unlike the single helical structure where a zig-zag vortex pattern

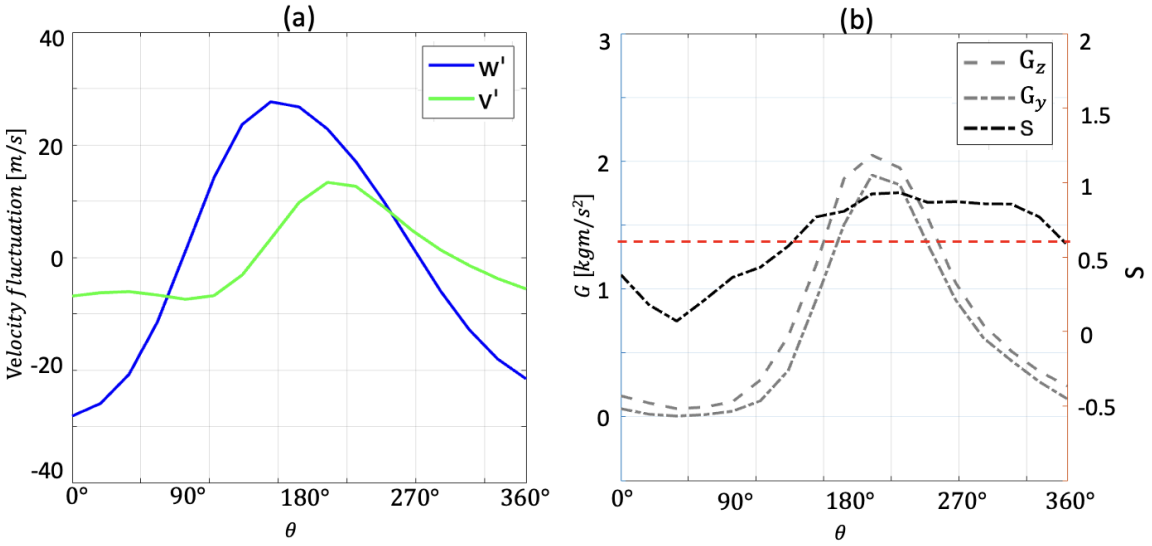

Figure 5.29: Spatially integrated variables at the dump plane in C2.

is presented as shown in Fig. 5.27, this double PVC leads to a nearly axisymmetric distribution of the local flow field and the flame topology on a 2D vertical plane. Another notable difference is instead of being lifted off, the flame is attached when the double PVC is excited (198° and 252°). A central vortex core forms at 180° with two distinct branches, which both co-rotate around the centreline in the clockwise direction and grow into two helices (198° and 252°). This double helical structure grows along the ISL and gains in size, before collapsing into a merged vortex core (360°), when the flame is slightly lifted with this single helix structure, similar to the flame detachment shown in 5.27. Finally, the PVC breaks into small eddies and vanishes (18°) as a result of the declining momentum fluxes and S.

In C2 and C3, a periodic evolution of the vortical structures linked to velocity fluctuations is also detected with a representative cycle is shown in Fig. 5.29. The phase difference between the v' wave and the w' wave increases to $\sim 44°$, and the peak amplitudes of G_z and G_y both reduce due to a lower mass flow rate. The resulting swirl number S fluctuates between 0.1 to 0.9 and remains above 0.6 during about 2/3 of the cycle, suggesting a less oscillating hydrodynamic field and longer existing time of the PVC compared to C1. In C2 and C3, instead of being bi-stable, a double helical structure is found to be excited and suppressed in every thermo-acoustic cycle, with the structure similar to the one displayed in Fig. 5.28 for C1. The evolution of vortical structures in the cycle shown in Fig. 5.29

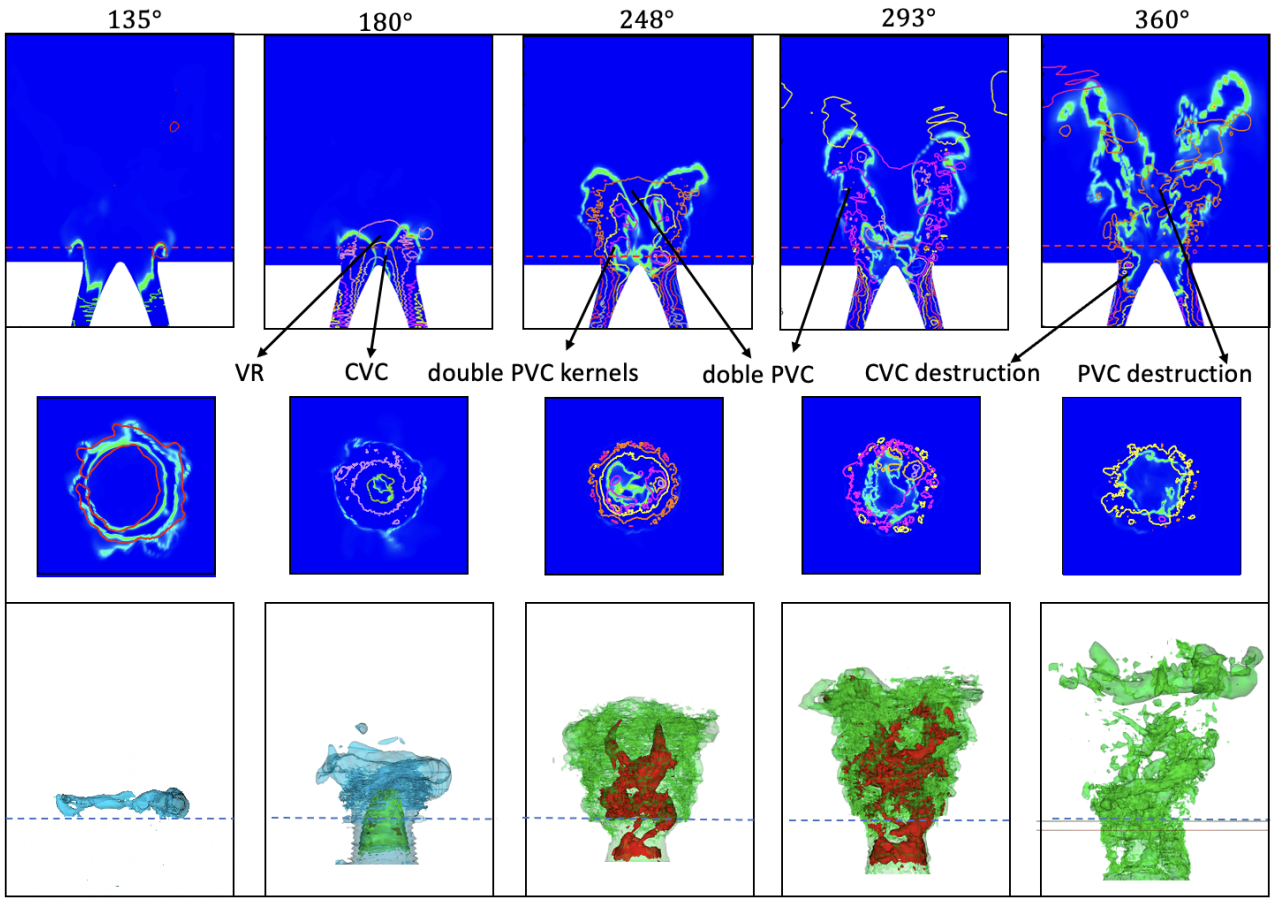

Figure 5.30: Temporal evolution of vortices structures and their impact on the flame in C2.

is presented in Fig. 5.30. A central vortex core forms at 180°, which grows into two branches both co-rotating around the centreline of the burner, with the flame remains attached throughout the cycle. The double helical structure rotates along the ISL before breaking down as shown at 360°. Compared to the double helices detected in C1, this double PVC in C2 expands less in the radial direction, which is likely due to the lower swirl number magnitude when the PVC is excited as shown in Fig. 5.29.

As discussed in section 5.4.3, PVC is identified as a global instability mode with a global frequency in linear stability analysis (Gallaire et al. 2006), where an azimuthal wave number m is associated to the PVC, which reflects the angular periodicity of it. The most common mode is a single helix structure corresponding to m = 1, as found in many experimental studies of swirling flames (Syred 2006, Wang et al. 2005, Stöhr et al. 2011, Moeck et al. 2012, Terhaar et al. 2015). Very rarely, in some instances, a double helix structure associated with m = 2 is observed in the experiments of swirling flames (Syred

2006, Vigueras-Zuñiga et al. 2012, Vignat et al. 2021), as this type of breakdown is highly sensitive to disturbances. The recent experimental study by Vanierschot et al. (2020) identified the m = 2 mode as an independent global mode instead of a second harmonic of the first mode (m = 1) in a swirling iso-thermal flow. (Vignat et al. 2021) investigated the transient PVC dynamics in a swirled spray flame under stable and unstable conditions. In the stable flame, the PVC took the form of a single helix with brief intermittent switching to a double, followed by a triple helical (m = 3) geometry, and these modes corresponded to flashback events that occur in a random way. In the unstable flame, the double helix PVC was found to be the dominant PVC mode, which was modulated at the thermo-acoustic frequency due to the oscillating mass flow rate at the injector. Only very few numerical works have reported the double helix structure. Zhang & Vanierschot (2021) used incompressible LES to predict single and double PVC in the iso-thermal flow investigated by Vanierschot et al. (2020). Mansouri et al. (2016) studied a double helical PVC and its interaction with a premixed propane flame in a swirl-stabilised burner using Detached Eddy Simulation. The vortex core was found to be characterised by solid-body rotation, which contains only fresh gases with no flame detected in the core region.

In a recent experimental work of a perfectly premixed PP PRECCINSTA flame, Yin & Stöhr (2020) used multi-resolution POD (MRPOD) to study the PVC and thermo-acoustic instabilities in a bi-stable flame, where the flame alternates irregularly between a M-shape and an V-shape. The PVC-related dynamics was found to have spatial and temporal bi-modal behaviours: the dominant PVC was observed to only prevail during M-shaple flame, while its harmonics, 2PVC and 3PVC, exist in a bi-modal trend: they could possess either a single or double helical structure and they could be active during either V or M flame periods with the same characteristic frequencies. Although under different operating conditions, these experimentally observed bi-modal PVCs can be compared to the one predicted here in C1 with the flame shape and position periodically oscillating. In addition, in the present work, the mode of the PVC is found to be related to the flame shape and fuel composition. In C2 and C3, an V-shape flame exist with a higher equivalence ratio $\phi = 0.85$ and hydrogen addition in C3, the single PVC mode is never observed and the flame is always attached to the centre body. This can be attributed to the fact that the higher equivalence ratio and hydrogen addition increases the extinction stretch rate of the lean premixed flame (Taamallah, Vogiatzaki, Alzahrani, Mokheimer, Habib & Ghoniem 2015), which determines the localised flame extinction in the turbulent combustion

(Sarli & Benedetto 2007). Stochastic extinction near the flame base reduce the radial density gradient, which was found to be a favourable condition for the formation of single PVC (Oberleithner et al. 2015). The C3 flame is thereby less likely to blow off at the flame base, leading to an unfavourable condition for the single PVC. However, instead of being suppressed, the helical structure presents a double-helix mode. Since the PVC formation was found to be strongly dependent on the density gradient region near the center cone, it is, again, closely related to the temperature distribution there and hence is subject to the complex interaction of the thermo-acoustic and wall heat transfer interaction. The determinant for the formation of the double-PVC remains unclear and a rigorous analysis of it is beyond the scope of the present work.

PVC and flame stabilisation

As shown above in Fig. 5.27,Fig. 5.28 and Fig. 5.30, flame attachment and detachment are closely correlated to the PVC structure in the flow, and will be discussed in detail in this section.

The dynamics of the single PVC formation and its interaction with the flame is shown in Fig. 5.31. The regions where the vortices interact with the flame are highlighted with dashed boxes and the enlarged views are shown on the right. First, as described in subsection 5.5.3, the azimuthal momentum flux increases followed by the formation of a single helix structure as shown at 198° with a typical zig-zag vortex pattern. The flame moves upstream as a result of the high speed reverse flow, deflected by the vortices, before colliding with the incoming flow on the *rhs*. A stagnation point (SP) and a stagnation line occur in the flow, as marked by the black dots and balck dashed lines, where the stagnation line represents the zone where the incoming flow and the recirculating flow from the IRZ collide. The SP blocks the reverse flow of hot burned gas toward the nozzle and thus stabilises the flame base near this point. When the PVC grows and rotates around the central axis, the vortices move downstream in the 2D plane, and another vortex appears on the right-hand side as shown at 216°. The SP also moves downstream due to its correlation with the vortex motion, resulting in the reaction zone being lifted. In a recent experimental study on a bi-stable flame by Stöhr et al. (2012), Oberleithner et al. (2015), Stöhr et al. (2018), a single PVC was also found to cause the flame detachment by creating an unsteady lower stagnation point whose dynamics coupled to the vortex motions. As described in

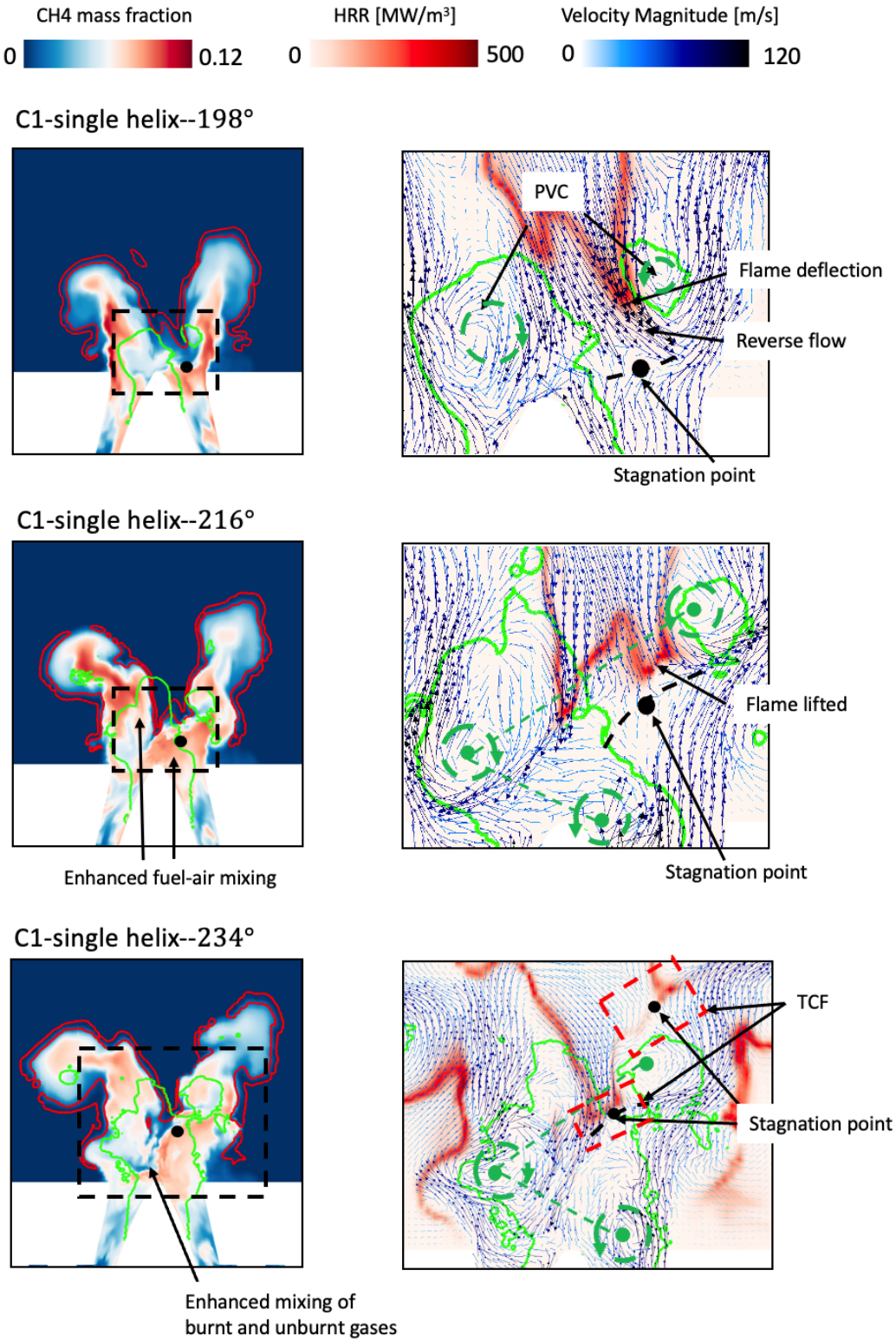

Figure 5.31: Instantaneous interaction of a single PVC with the flame. Left: CH_4 mass fraction overlapped with HRR iso-contours in red with a value of $80 \mathrm{MW/m^3}$ which is about 5% of the maximum value. Right: in-plane velocity vectors coloured by velocity magnitude overlapped on the HRR colour plot. The green iso-contours represent the vortical structures.

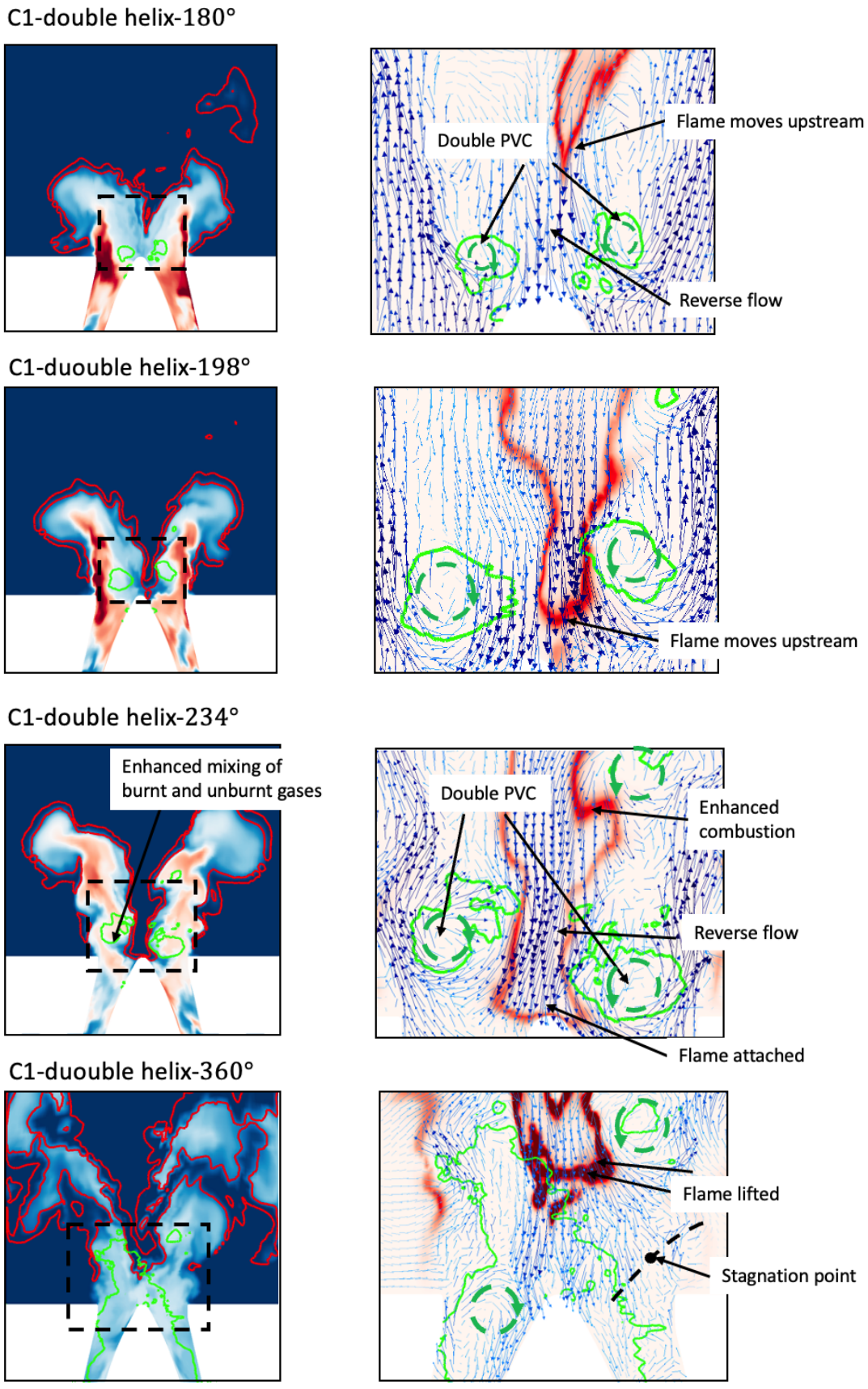

Figure 5.32: Instantaneous interaction of a double PVC with the flame.

Stöhr et al. (2012), the unsteady SP is an important feature of the PVC as it determines the position of the flame root. At 234° when the PVC further grows, the flow field becomes more complex due to the vortex motions, and an additional stagnation point is found at the top rhs of the enlarged view. The local collision of the opposed flows of burned and unburned gas with the thin flame brush between them forms a configuration of a turbulent counter-flow flame (TCF) near the two SPs, which is the target benchmark discussed in Chapter 3. Along these stagnation lines, the burned gas supplies heat and radicals to the fresh gas and which are favourable for local re-ignitions.

Figure 5.32 shows the temporal evolution of a double PVC and the resulting flame and flow field. At 180°, a pair of symmetric vortices form above the dump plane. Stöhr et al. (2018) detected a symmetric vortex pair above the inlet in a transient flame in 2D PIV data and identified that they were caused by the pumping motion of the TA instability. However, as shown in the 3D visualisation of the vortical structure in Fig. 5.28 and Fig. 5.30, these symmetric vortices correspond to a double helix structure in the present work. The double helices grow along with the formation of a continuous reverse flow in the IRZ, causing the flame to move upstream (198°). Instead of being deflected towards one side by the single PVC, the flame propagates axisymmetrically along the centreline due to the symmetry of the flow field. As a consequence, a local stagnation point is absent above the dump plane and the flame is further convected upstream and touches the centre-cone at 234°. As one of the helices breaks (360°), the flame is lifted as a result of the remained single helix as a results of the SP begins to form at the lower right corner. In C2 and C3 where a double PVC is repeatedly excited in every thermo-acoustic cycle, the flame attachment is enhanced by the back-flow in the IRZ and the vortex motions coupled to the double-helix structure.

5.5.4 Combined effects

In addition to the helical structure effect on the flame stabilisation, other interaction of PVC and the flame can also be detected. V-shape flames stabilise along the ISL, and PVC structure interacts with and distorts the ISL significantly (as discussed by the velocity fluctuations together with PVC evolution shown in Fig. 5.11), hence PVC contributes to the observed narrower flame as shown in Fig. 5.13 and Fig. 5.14. In addition, by changing the flame topology and position as described above

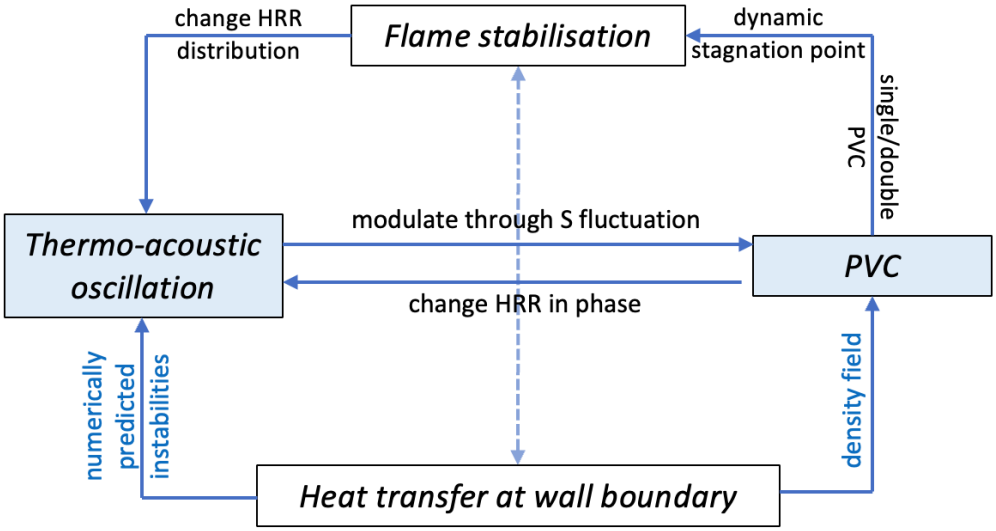

Figure 5.33: The interplay of the thermo-acoustic oscillations, PVC structure and the flame stabilisation, with the wall-heat tranfer effect on them potentially.

with single or double PVC, the flame length and anchoring position changes accordingly, which, as discussed in Subsection 5.5.2, impacts the phase difference between the acoustic oscillations and HRR oscillations that determines the thermo-acoustic intensity.

The PVC structure also changes the unsteady heat release locally. As shown in Fig. 5.31 and Fig. 5.32, the flame front is locally rolled up and elongated by the large-scale vortices, thereby the PVC directly modulates the overall flame 'surface area' and generates unsteady heat release (Fredrich et al. 2021*a*). The PVC further affects the combustion by enhancing the local mixing of the fuel and oxidiser and by enhanced mixing of burned and unburned gas as shown in Fig. 5.31 and Fig. 5.32, as reported in numerous studies (Stöhr et al. 2011, Froud et al. 1995, Stöhr et al. 2015). Stöhr et al. (2012) reported PVC could affected the location of the regions of high compressive strain rates which highly coincided with the reaction zone. It has also been found that the combustion is enhanced along the helix edge at some instances as shown in Fig. 5.31 and Fig. 5.32, and explains why the integrated HRR shown in Fig. 5.14 has a high value in the region along ISL close to the centre body, where PVC affects most.

It is now clear that both single and double PVC are coupled with the local HRR via the mechanism discussed above. Prior studies on consistently active PVC have suggested that PVC precession around the burner did not contribute to fluctuations of the global HRR: the associated fluctuations in local

heat release have previously been shown to cancel out in space over the oscillation period Moeck et al. (2012). However, when the PVC is periodically modulated due to the swirl number fluctuation, a phase-specific influence on the global HRR was observed (Caux-Brisebois et al. 2014, Fredrich et al. 2021*a*). The flow–flame interactions associated with deformation or excitation of the PVC at the thermo-acoustic frequency couples the HRR fluctuations with the acoustic oscillations. The change in total HRR over the thermo-acoustic cycle is not due to the PVC's precession around the burner, which occurred at a different frequency, but rather at the thermo-acoustic frequency. The hydrodynamic evolutions amplify the global instability by increasing HRR in phase with the dominant thermo-acoustic fluctuations, thereby feeding acoustic energy into the system. Hence, the feedback loop of the self-sustained strong thermo-acoustic fluctuations in all the cases investigated in the present work is a combined effect of the equivalence ratio fluctuations and the hydrodynamic instabilities.

Fig. 5.33 briefly summerises that the interplay of the thermo-acoustic oscillations, PVC structure and the flame stabilisation process, with the pre-mentioned wall transfer effect on them. Thermo-acoustic instabilities interact with the swirl unit, periodically exciting or suppressing the PVC structure, which, in turn, increasing HRR in phase with the thermo-acoustic oscillations, hence amplifies the thermo-acoustic fluctuations. Single or double PVC determines the flame stabilisation, leading to different flame topology and therby changing the phase difference between the acoustic oscillations and HRR oscillations that impacts the intensity of thermo-acoustic instabilities. Wall heat transfer directly impacts the temperature field in the near wall region, which impacts the flame stabilisation; it affects the density field close to the center body, which plays an important role in the PVC dynamics. Finally, fixing the wall temperature was found closely related to the numerically predicted thermo-acoustic instabilities with high non-homogeneous heat transfer near the centre body.

5.6 Conclusions

The self-excited combustion dynamics in swirling flames under different operating conditions is investigated using LES. The targeted technically premixed PRECCINSTA flames have previously been shown to exhibit combustion-driven instabilities under various operating conditions. In the iso-

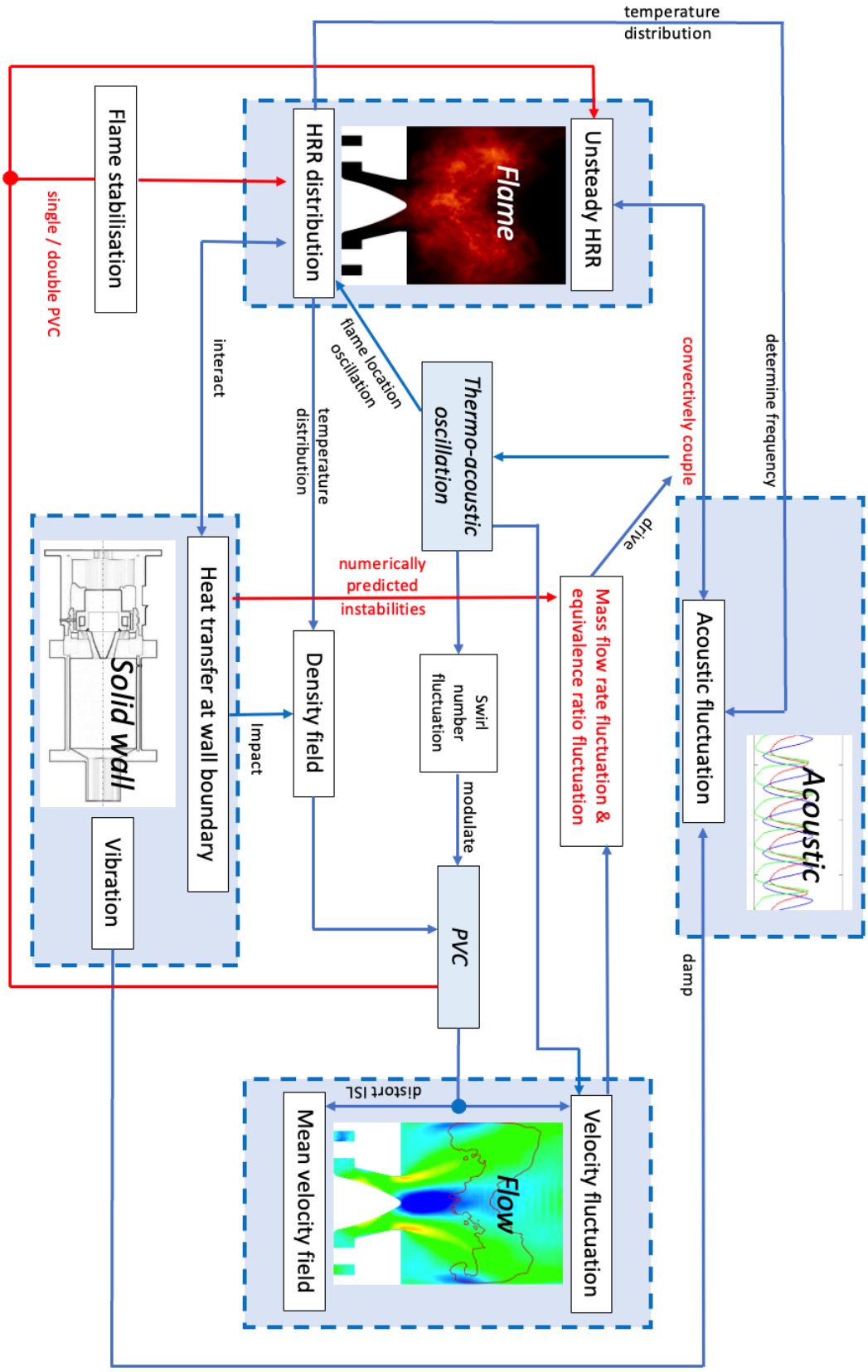

Figure 5.34: Schematic overview of the interplay of the unsteady flame, flow field, acoustic field and solid boundary. The figure is rotated by 90° to fit the page size.

thermal flows, the simulated and measured velocities are overall in good agreement. A continuously active single PVC is observed in all the iso-thermal flows, and the predicted PVC frequencies are in good agreement with the value observed experimentally. In the reacting cases, a lifted M shape flame is detected in C1 while an attached V shape flame is found in C2 and C3, which are consistent with the experimental observations. Self-sustained, limit cycle oscillations are observed in all three cases, which are identified as thermo-acoustic fluctuations. The predicted dominant acoustic frequencies are in overall good agreement with the measured ones, while the fluctuation amplitudes are over-estimated and strong coupling between the heat release rate fluctuations and the acoustic fluctuations are found in cases that are experimentally observed stable. These numerically predicted thermo-acoustic oscillations are closely related to the predicted wall heat transfer using fixed the wall temperatures. The hydrogen addition is found to affect the thermo-acoustic instabilities by affecting the flame shape and the heat release level, leading to a higher dominant frequency and lower peak amplitude.

The driving mechanism of the observed thermo-acoustic fluctuations is identified as a combination of equivalence ratio fluctuations and mass flow rate fluctuations in all reacting cases (C1-C3). The acoustic waves interact with the burner unit, generating swirl number fluctuations which leads to a periodic excitation and suppression of the helical structure. The PVC in C1 exhibit a bi-modal behaviour: these instabilities attain either a single or double helical structure in a random manner, while in C2 and C3 a double PVC is always excited. The single PVC is found to be related to the flame detachment by creating a dynamic stagnation point due to the resulting asymmetric flow field, which is absent when the double PVC is excited and flame remains attached as a consequence. The PVC modulates the flame surface area and local heat release, amplifying the thermo-acoustic fluctuations, which completes the feedback mechanism of the predicted self-sustained instabilities.

Finally, a comprehensive diagram is created to display the interactions between the unsteady flame, flow field, acoustic field and solid boundary in the LES study of the PRECCINSTA TP flames, as shown in Fig.5.34. This aims at summarising the results and findings of the LES study, showing the intrinsic connections of the observed phenomena and great complexity of the problem, and thereby concluding the work in this chapter.

Chapter 6

Conclusions and Outlooks

Combustion instabilities remain a central issue in the designing and constructing lean combustion systems, which requires a thorough understanding of the relevant physical processes and their interactions. The research project described in this work explores the capabilities of the Eulerian stochastic field method, BOFFIN-LES, in study of combustion dynamics. This LES provides a burning regime independent description of turbulent flames and can be readily complemented with different chemical mechanisms. Three test cases with different levels of complexities focusing on different aspects of the problem have been performed.

6.1 Summary of Thesis Achievements

The first full-scale test case of this work was a series of fully-premixed turbulent counter-flow flames (TCF), which are highly stretched flames with unsteadiness generated by turbulent eddies. The flame undergoes large scale transient motions and small scale local-extinction and re-ignition. The centre-line profiles of the mean and *rms* velocities were well reproduced with the inflow boundary condition method proposed. Sensitivity analysis regarding the number of stochastic fields showed that a relatively small number of stochastic fields (8) are sufficient to model the sgs chemistry effects for the case considered. The predicted probability of localised extinction was in good agreement with the

measurements, and the influence of the flame composition was also successfully reproduced. Local-extinctions were found to be correlated to the turbulent-chemistry interactions, so were the re-ignition processes. Overall, the results served to demonstrate the capability of the LES method in the study of flame dynamics in the unsteady stretched flames in high Re flows.

The second investigated case was the noise generation in an Entropy Wave Generator (EWG) comprising a resonator with a non-isentropic nozzle. The disturbances were created by cross-flow pulse injections of a secondary gas with a different composition. The pressure signal extracted from the LES reproduced the direct and indirect noise generating process and matched the measurements to a good level of accuracy for different injection gases. The ratio of indirect to direct noise is quantified under different conditions and the effect of increasing the main flow mass flow rate on noise generation was also investigated. The predicted indirect noise amplitudes were found to be related to the losses in the system, which were over-predicted in the simulation when the Mach number in the nozzle approaching unity and shocks may exist. Under this condition, the accuracy of the numerical method was uncertain. Overall, the results indicate the capability of the LES method and the successful application of the acoustic boundary conditions with appropriate assumptions and interpolations in the study of noise generation problems.

The last stage of the present work included the numerical study of a series of technically premixed, swirl-stabilised flames in the PRECCINSTA model combustor. Different operating conditions were included in the LES study with various equivalence ratios and hydrogen addition in the fuel. The targeted PRECCINSTA flames have previously been shown to exhibit combustion-driven instabilities under various operating conditions. In the iso-thermal flows, the simulated and measured axial velocities were overall in good agreement; a continuously active single PVC was observed, with the precessing frequency well predicted by the LES. In the reacting cases, a lifted M-shape flame was found in C1 while an attached V-shape flame was observed in C2 and C3, which was consistent with the experimental observations. Strong thermo-acoustic instabilities and hydrodynamics instabilities are observed in all the cases. The dominant frequencies of the thermo-acoustic oscillations are well predicted in the LES, while the fluctuation amplitudes were over-estimated in the LES for the V flames. The over-prediction of the acoustic intensity is likely associated with to the acoustic damping

caused by the quartz windows in the experiments and an numerically predicted instability source in the LES caused by fixing the wall temperatures. The hydrogen addition under the present operating conditions is found to modify the thermo-acoustic instabilities by changing the flame position and flame temperature, leading to a higher dominant frequency and lower peak amplitude. The dominant driving mechanism of the observed thermo-acoustic fluctuations was identified as a combined effect of equivalence ratio and velocity fluctuations in all the cases investigated. The acoustic waves interact with the swirler unit, generating swirl number fluctuations which leads to periodic excitations and suppressions of PVC structures. The helix structure was generated in a bi-stable trend in the M-shape flame: a single PVC is most often observed with a double PVC excited in some cycles randomly; while a double PVC is always found in the V-shape flames. The single PVC was found to be related to flame detachment by creating an unsteady stagnation point due to its asymmetry, which was absent when the double PVC was excited and hence the flame was attached. The PVC was found to modulate the flame surface area and local heat released, amplifying the thermo-acoustic fluctuations, which completes the feedback mechanism of the predicted self-sustained fluctuations.

In summary, the results of this work have shown that the proposed LES-*pdf* methodology can be a very promising tool to study a wide variety of unsteady flame physics in complicated geometries without any adjustment of model parameters, which suggests its wide-ranging applicability.

6.2 Future Work

For future work, several investigations of combustion instability mechanisms based on the PRECCINSTA test case have been planned. One potential scope is to include the damping effect of the quartz windows in the experiments and the dynamic heat conducted to the solid boundaries by appropriate modelling methods. This might require further collaborations with the experimentalists for more measurements with better-defined acoustic and thermal boundary conditions. Besides, the observed instability modes can be better identified and investigated with help of proper orthogonal decomposition (POD) or dynamic mode decomposition (DMD), which may provide valuable knowledge about the nature of the dominant thermo-acoustic mode and the two helical modes including their spatial

and temporal features.

Challenging tasks to further develop the method would be the simulation of realistic combustion chamber geometries as utilised by gas turbine manufacturers with complex geometries. BOFFIN-LES currently features multi-blocked, structured Cartesian grids. It proves to be quite difficult to create appropriate computational meshes when the geometry becomes very complex. A logical extension of the present numerical method includes using unstructured grids, which gives unlimited geometric flexibility and allows more efficient use of computing resources for complex flows. Furthermore, the extension to a conjugate heat transfer approach where the heat conduction in the walls of the chamber is resolved and the resulting wall temperatures are coupled to the LES dynamically. Despite the complexity, this approach has gained growing attention due to the fact that transient wall heat transfer effects have been confirmed to play an important role in the flame stabilisation and flame dynamics.

Bibliography

Agostinelli, P. W., Laera, D., Boxx, I., Gicquel, L. & Poinsot, T. (2021), 'Impact of wall heat transfer in Large Eddy Simulation of flame dynamics in a swirled combustion chamber', *Combustion and Flame* **234**, 111728.

An, Q. & Steinberg, A. M. (2019), 'The role of strain rate, local extinction, and hydrodynamic instability on transition between attached and lifted swirl flames', *Combustion and Flame* **199**, 267–278.

Anderson, J. (1995), *Computational Fluid Dynamics: The Basics with Applications*, McGraw-Hill.

Bake, F., Richter, C., Mühlbauer, B., Kings, N., Röhle, I., Thiele, F. & Noll, B. (2009), 'The Entropy Wave Generator (EWG): A reference case on entropy noise', *Journal of Sound and Vibration* **326**(3), 574–598.

Balaras, E., Benocci, C. & Piomelli, U. (1996), 'Two-layer approximate boundary conditions for large-eddy simulations', *AIAA Journal* **34**, 1111–1119.

Benard, P., Lartigue, G., Moureau, V. & Mercier, R. (2019), 'Large-Eddy Simulation of the lean-premixed PRECCINSTA burner with wall heat loss', *Proceedings of the Combustion Institute* **37**, 5233–5243.

Benim, A., Nahavandi, A. & Syed, K. (2005), 'Urans and les analysis of turbulent swirling flows', *Progress in Computational Fluid Dynamics, an International Journal* **5**(8), 444–454.

Bini, M. & Jones, W. P. (2008), 'Large-eddy simulation of particle-laden turbulent flows', *Journal of Fluid Mechanics* **614**, 207–252.

Bird, R. B., Stewart, W. E. & Lightfoot, E. N. (2006), *Transport Phenomena*, Wiley.

Bloxsidge, G. J., Dowling, A. P. & Langhorne, P. J. (1988), 'Reheat buzz: an acoustically coupled combustion instability. Part 2. Theory', *Journal of Fluid Mechanics* **193**, 445.

Böhm, B., Stein, O., Kempf, A. & Dreizler, A. (2010), 'In-Nozzle Measurements of a Turbulent Opposed Jet Using PIV', *Flow Turbulence Combust* **85**(1), 73–93.

Boxx, I., Arndt, C. M., Carter, C. D. & Meier, W. (2012), 'High-speed laser diagnostics for the study of flame dynamics in a lean premixed gas turbine model combustor', *Experiments in Fluids* **52**, 555–567.

Brauner, T., Jones, W. P. & Marquis, A. J. (2016), 'LES of the Cambridge Stratified Swirl Burner using a Sub-grid pdf Approach', *Flow Turbulence Combust* **96**(4), 965–985.

Bulat, G., Jones, W. & Marquis, A. (2014), 'No and co formation in an industrial gas-turbine combustion chamber using les with the eulerian sub-grid pdf method', *Combustion and Flame* **161**, 1804–1825.

Candel, S., Durox, D., Schuller, T., Bourgouin, J. F. & Moeck, J. P. (2014), 'Dynamics of swirling flames', *Annual Review of Fluid Mechanics* **46**, 147–173.

Candel, S., Durox, D., Schuller, T., Palies, P., Bourgouin, J.-F. & Moeck, J. P. (2012), 'Progress and challenges in swirling flame dynamics', *Comptes Rendus Mecanique* **340**(11-12), 758–768.

Cant, R. S. & Mastorakos, E. (2007), *An Introduction to Turbulent Reacting Flows*, Imperial College Press.

Caux-Brisebois, V., Steinberg, A. M., Arndt, C. M. & Meier, W. (2014), 'Thermo-acoustic velocity coupling in a swirl stabilized gas turbine model combustor', *Combustion and Flame* **161**, 3166–3180.

Celik, I., Klein, M., Freitag, M. & Janicka, J. (2006), 'Assessment measures for urans/des/les: an overview with applications', *Journal of Turbulence* (7), N48.

Chaumeix, N., Pichon, S., Lafosse, F. & Paillard, C. (2007), 'Role of chemical kinetics on the detonation properties of hydrogen /natural gas/air mixtures', *International Journal of Hydrogen Energy* **32**, 2216–2226.

Chen, Z. X., Langella, I., Swaminathan, N., Stöhr, M., Meier, W. & Kolla, H. (2019), 'Large Eddy Simulation of a dual swirl gas turbine combustor: Flame/flow structures and stabilisation under thermoacoustically stable and unstable conditions', *Combustion and Flame* **203**, 279–300.

Chigier, N. A. & Beér, J. M. (1964), 'The flow region near the nozzle in double concentric jets', *Journal of Fluids Engineering, Transactions of the ASME* **86**.

Chigier, N. A. & Chervinsky, A. (1967), 'Experimental Investigation of Swirling Vortex Motion in Jets', *Journal of Applied Mechanics* **34**, 443–451.

Christodoulou, L., Karimi, N., Cammarano, A., Paul, M. & Navarro-Martinez, S. (2020), 'State prediction of an entropy wave advecting through a turbulent channel flow', *Journal of Fluid Mechanics* **882**, 121–30.

Chterev, I. (2020), personal communication.

Chterev, I. & Boxx, I. (2019), Flame Topology and Combustion Instability Limits of Lean Premixed Hydrogen Enriched Flames, *in* '26th International Colloquium on the Dynamics of Explosions and Reactive Systems ICDERS', Combustion Institute.

Chterev, I. & Boxx, I. (2021), 'Effect of hydrogen enrichment on the dynamics of a lean technically premixed elevated pressure flame', *Combustion and Flame* **225**, 149–159.

Chterev, I., Foley, C. W., Foti, D., Kostka, S., Caswell, A. W., Jiang, N., Lynch, A., Noble, D. R., Menon, S., Seitzman, J. M. & Lieuwen, T. C. (2014), 'Flame and flow topologies in an annular swirling flow', *Combustion Science and Technology* **186**, 1041–1074.

Chu, B.-T. & Kovásznay, L. S. G. (1958), 'Non-linear interactions in a viscous heat-conducting compressible gas', *Journal of Fluid Mechanics* **3**(5), 494–514.

Colucci, P. J., Jaberi, F. A., Givi, P. & Pope, S. B. (1998), 'Filtered density function for large eddy simulation of turbulent reacting flows', *Physics of Fluids* **10**.

Coppola, G. & Gomez, A. (2009), 'Experimental investigation on a turbulence generation system with high-blockage plates', *Experimental Thermal and Fluid Science* **33**(7), 1037–1048.

Coppola, G.and Gomez, A. (2010), 'Experimental study of highly turbulent isothermal opposed-jet flows', *Physics of Fluids* **22**, 105101.

Coriton, B., Frank, J. H. & Gomez, A. (2013), 'Effects of strain rate, turbulence, reactant stoichiometry and heat losses on the interaction of turbulent premixed flames with stoichiometric counterflowing combustion products', *Combustion and Flame* **160**(11), 2442–2456.

Coriton, B., Frank, J. H., Hsu, A. G., Smooke, M. D. & Gomez, A. (2011), 'Effect of quenching of the oxidation layer in highly turbulent counterflow premixed flames', *Proceedings of the Combustion Institute* **33**(1), 1647–1654.

Correa, S. M. (1998), 'Power generation and aeropropulsion gas turbines: From combustion science to combustion technology', *Symposium (International) on Combustion* **27**, 1793–1807.

Cumpsty, N. A., & Marble, F. E. (1977), 'The interaction of entropy fluctuations with turbine blade rows; a mechanism of turbojet engine noise', *Proceedings of the Royal Society of London. A. Mathematical and Physical Sciences* **357**, 323–344.

Delafosse, A., Line, A., Morchain, J. & Guiraud, P. (2008), 'Les and urans simulations of hydrodynamics in mixing tank: Comparison to piv experiments', *Chemical Engineering Research and Design* **86**(12), 1322–1330.

Dhamankar, N. S., Blaisdell, G. A. & Lyrintzis, A. S. (2018), 'Overview of turbulent inflow boundary conditions for large-eddy simulations', *AIAA Journal* **56**, 1317–1334.

di Domenico, F., Rolland, E. O. & Hochgreb, S. (2017), 'Detection of direct and indirect noise generated by synthetic hot spots in a duct', *Journal of Sound and Vibration* **394**, 220–236.

di Domenico, F., Rolland, E. O., Rodrigues, J., Magri, L. & Hochgreb, S. (2021), 'Compositional and entropy indirect noise generated in subsonic non-isentropic nozzles', *Journal of Fluid Mechanics* **910**, 031003–31.

di Mare, L., Klein, M., Jones, W. P. & Janicka, J. (2006), 'Synthetic turbulence inflow conditions for large-eddy simulation', *Physics of Fluids* **18**(2), 025107.

Domenico, F. D., Rolland, E. O. & Hochgreb, S. (2019), 'A generalised model for acoustic and entropic transfer function of nozzles with losses', *Journal of Sound and Vibration* **440**, 212–230.

Dopazo, C. (1975), 'Probability density function approach for a turbulent axisymmetric heated jet. Centerline evolution', *Physics of Fluids* **18**, 397.

Dowling, A. P. (1999), 'A kinematic model of a ducted flame', *Journal of Fluid Mechanics* **394**, 51–72.

Dowling, A. P. & Mahmoudi, Y. (2015), 'Combustion noise', *Proceedings of the Combustion Institute* **35**(1), 65–100.

Draad, A. A., Kuiken, G. D. C. & Nieuwstadt, F. T. M. (1998), 'Laminar–turbulent transition in pipe flow for newtonian and non-newtonian fluids', *Journal of Fluid Mechanics* **377**, 267–312.

Duran, I., Moreau, S. & Poinsot, T. (2013), 'Analytical and Numerical Study of Combustion Noise Through a Subsonic Nozzle', *AIAA Journal* **51**(1), 42–52.

Durox, D., Moeck, J. P., Bourgouin, J. F., Morenton, P., Viallon, M., Schuller, T. & Candel, S. (2013), 'Flame dynamics of a variable swirl number system and instability control', *Combustion and Flame* **160**, 1729–1742.

D.W. Perry, R.H., G. (2008), *Perry's Chemical Engineers' Handbook (8th ed.)*, McGraw-Hill.

Edwards, P. P., Kuznetsov, V. L., David, W. I. F. & Brandon, N. P. (2008), 'Hydrogen and fuel cells: Towards a sustainable energy future', *Energy Policy* **36**(12), 4356–4362.

Engquist, B. & Majda, A. (1977), 'Absorbing boundary conditions for numerical simulation of waves', *Proceedings of the National Academy of Sciences of the United States of America* **74**, 1765–6.

Erlebacher, G., Hussaini, M. Y., Speziale, C. G. & Zang, T. A. (1992), 'Toward the large-eddy simulation of compressible turbulent flows', *Journal of Fluid Mechanics* **238**, 155–185.

Ferziger, J. H. & Perić, M. (2002), *Computational Methods for Fluid Dynamics*, Springer Berlin Heidelberg.

Fleifil, M., Annaswamy, A. M., Ghoneim, Z. A. & Ghoniem, A. F. (1996), 'Response of a laminar premixed flame to flow oscillations: A kinematic model and thermoacoustic instability results', *Combustion and Flame* **106**, 487–510.

Foley, C., Chterev, I., Noble, B., Seitzman, J. & Lieuwen, T. (2017), 'Shear layer flame stabilization sensitivities in a swirling flow', *International Journal of Spray and Combustion Dynamics* **9**, 3–18.

Franzelli, B., Riber, E., Gicquel, L. Y. & Poinsot, T. (2012), 'Large Eddy Simulation of combustion instabilities in a lean partially premixed swirled flame', *Combustion and Flame* **159**, 621–637.

Fredrich, D. (2019), A Numerical Method for the Prediction of Combustion Instabilities, PhD thesis, Imperial College London.

Fredrich, D., Jones, W. P. & Marquis, A. J. (2019), 'The stochastic fields method applied to a partially premixed swirl flame with wall heat transfer', *Combustion and Flame* **205**, 446–456.

Fredrich, D., Jones, W. P. & Marquis, A. J. (2021*a*), 'A combined oscillation cycle involving self-excited thermo-acoustic and hydrodynamic instability mechanisms', *Physics of Fluids* **33**.

Fredrich, D., Jones, W. P. & Marquis, A. J. (2021*b*), 'Thermo-acoustic Instabilities in the PRECCINSTA Combustor Investigated Using a Compressible LES-pdf Approach', *Flow, Turbulence and Combustion* **106**, 1399–1415.

Froud, D., O'Doherty, T. & Syred, N. (1995), 'Phase averaging of the precessing vortex core in a swirl burner under piloted and premixed combustion conditions', *Combustion and Flame* **100**, 407–412.

Gallaire, F., Ruith, M., Meiburg, E., Chomaz, J. & Huerre, P. (2006), 'Spiral vortex breakdown as a global mode', *Journal of Fluid Mechanics* **549**, 71.

Gallot-Lavallée, S., Jones, W. P. & Marquis, A. J. (2017), 'Large Eddy Simulation of an ethanol spray flame under MILD combustion with the stochastic fields method', *Proceedings of the Combustion Institute* **36**(2), 2577–2584.

Gao, F. & O'Brien, E. E. (1998), 'A large-eddy simulation scheme for turbulent reacting flows', *Physics of Fluids A: Fluid Dynamics* **5**(6), 1282–1284.

Gardiner, C. (1985), *Handbook of stochastic methods*, Springer.

Garmory, A., Richardson, E. & Mastorakos, E. (2006), 'Micromixing effects in a reacting plume by the stochastic fields method', *Atmospheric Environment* **40**, 1078–1091.

Geyer, D., Kempf, A., Dreizler, A. & Janicka, J. (2005*a*), 'Scalar dissipation rates in isothermal and reactive turbulent opposed-jets: 1-D-Raman/Rayleigh experiments supported by LES', *Proceedings of the Combustion Institute* **30**(1), 681–689.

Geyer, D., Kempf, A., Dreizler, A. & Janicka, J. (2005*b*), 'Turbulent opposed-jet flames: A critical benchmark experiment for combustion LES', *Combustion and Flame* **143**(4), 524–548.

Giauque, A., Selle, L., Gicquel, L., Poinsot, T., Buechner, H., Kaufmann, P. & Krebs, W. (2005), 'System identification of a large-scale swirled partially premixed combustor using LES and measurements', *Journal of Turbulence* **6**, N21.

Giusti, A., Magri, L. & Zedda, M. (2018), 'Flow Inhomogeneities in a Realistic Aeronautical Gas-Turbine Combustor: Formation, Evolution, and Indirect Noise', *J. Eng. Gas Turbines Power* **141**(1).

Giusti, A., Worth, N. A., Mastorakos, E. & Dowling, A. P. (2017), 'Experimental and Numerical Investigation into the Propagation of Entropy Waves', *AIAA Journal* pp. 1–13.

Glassman, I., Yetter, R. A. & Glumac, N. G. (2014), *Combustion*, Academic press.

Goh, C. S. & Morgans, A. S. (2011), 'Phase prediction of the response of choked nozzles to entropy and acoustic disturbances', *Journal of Sound and Vibration* **330**(21), 5184–5198.

Gomez, A. (2011), 'Highly Turbulent Counterflow Flames: A Laboratory-Scale Benchmark for Turbulent Combustion Studies', *Fall Technical Meeting of the Eastern States Section of the Combustion Institute* .

Guiberti, T. F., Durox, D., Scouflaire, P. & Schuller, T. (2015), 'Impact of heat loss and hydrogen enrichment on the shape of confined swirling flames', *Proceedings of the Combustion Institute* **35**, 1385–1392.

Halter, F., Chauveau, C., Djebaïli-Chaumeix, N. & Gökalp, I. (2005), 'Characterization of the effects of pressure and hydrogen concentration on laminar burning velocities of methane–hydrogen–air mixtures', *Proceedings of the Combustion Institute* **30**, 201–208.

Han, X. & Morgans, A. S. (2015), 'Simulation of the flame describing function of a turbulent premixed flame using an open-source LES solver', *Combustion and Flame* **162**, 1778–1792.

Hauke, G. & Valiño, L. (2004), 'Computing reactive flows with a field Monte Carlo formulation and multi-scale methods', *Computer Methods in Applied Mechanics and Engineering* **193**, 1455–1470.

Hawkes, E. R. & Chen, J. H. (2004), 'Direct numerical simulation of hydrogen-enriched lean premixed methane–air flames', *Combustion and Flame* **138**(3), 242 – 258.

Hermeth, S., Staffelbach, G., Gicquel, L. Y. & Poinsot, T. (2013), 'LES evaluation of the effects of equivalence ratio fluctuations on the dynamic flame response in a real gas turbine combustion chamber', *Proceedings of the Combustion Institute* **34**, 3165–3173.

Hoffmann, G. & Benocci, C. (1995), Approximate wall boundary conditions for large eddy simulations, *in* 'Advances in Turbulence V', Springer, p. 222–228.

Hong, S., Shanbhogue, S. J., Kedia, K. S. & Ghoniem, A. F. (2013), 'Impact of the Flame-Holder Heat-Transfer Characteristics on the Onset of Combustion Instability', *Combustion Science and Technology* **185**, 1541–1567.

Howe, M. S. (2010), 'Indirect combustion noise', *Journal of Fluid Mechanics* **659**, 267–288.

Hu, E., Huang, Z., He, J., Jin, C. & Zheng, J. (2009), 'Experimental and numerical study on laminar burning characteristics of premixed methane–hydrogen–air flames', *International Journal of Hydrogen Energy* **34**, 4876–4888.

Huang, Y. & Yang, V. (2009), 'Dynamics and stability of lean-premixed swirl-stabilized combustion', *Progress in Energy and Combustion Science* **35**, 293–364.

Hult, J., Meier, U., Meier, W., Harvey, A. & Kaminski, C. F. (2005), 'Experimental analysis of local flame extinction in a turbulent jet diffusion flame by high repetition 2-D laser techniques and multiscalar measurements', *Proceedings of the Combustion Institute* **30**, 701–709.

Ihme, M. (2017), 'Combustion and Engine-Core Noise', *Annual Review of Fluid Mechanics* **49**(1), 277–310.

Iudiciani, P. & Duwig, C. (2011), 'Large Eddy Simulation of the Sensitivity of Vortex Breakdown and Flame Stabilisation to Axial Forcing', *Flow, Turbulence and Combustion* **86**, 639–666.

J Eckstein, J. Y. C., Chou, C. P. & Janicka, J. (2000), 'Modeling of turbulent mixing in opposed jet configuration: One-dimensional Monte Carlo probability density function simulation', *Proceedings of the Combustion Institute* **28**, 141–148.

Jackson, G. S., Sai, R., Plaia, J. M., Boggs, C. M. & Kiger, K. T. (2003), 'Influence of h2 on the response of lean premixed ch4 flames to high strained flows', *Combustion and Flame* **132**, 503–511.

Jeong, J. & Hussain, F. (1995), 'On the identification of a vortex', *Journal of Fluid Mechanics* **285**, 69–94.

Jones, W. & Navarro-Martinez, S. (2007), 'Large eddy simulation of autoignition with a subgrid probability density function method', *Combustion and Flame* **150**.

Jones, W. & Navarro-Martinez, S. (2008), 'Study of hydrogen auto-ignition in a turbulent air co-flow using a Large Eddy Simulation approach', *Computers and Fluids* **37**.

Jones, W., Navarro-Martinez, S. & Röhl, O. (n.d.), 'large eddy simulation of hydrogen auto-ignition with a probability density function method', *Proceedings of the Combustion Institute* pp. 1765–1771.

Jones, W. P., di Mare, F. & Marquis, A. J. (2002), *LES-BOFFIN: Users Guide*.

Jones, W. P., Jurisch, M. & Marquis, A. J. (2015), 'Examination of an Oscillating Flame in the Turbulent Flow Around a Bluff Body with Large Eddy Simulation Based on the Probability Density Function Method', *Flow, Turbulence and Combustion* **95**, 519–538.

Jones, W. P., Marquis, A. J. & Prasad, V. N. (2012), 'LES of a turbulent premixed swirl burner using the Eulerian stochastic field method', *Combustion and Flame* **159**, 3079–3095.

Jones, W. P. & Prasetyo, Y. (1996), 'Probability density function modeling of premixed turbulent opposed jet flames', *Symposium (International) on Combustion* **26**(1), 275–282.

Jones, W. & Prasad, V. (2010), 'Large Eddy Simulation of the Sandia Flame Series (D–F) using the Eulerian stochastic field method', *Combustion and Flame* **157**.

Karlis, E., Liu, Y., Hardalupas, Y. & Taylor, A. M. K. P. (2019), 'H2 enrichment of CH4 blends in lean premixed gas turbine combustion: An experimental study on effects on flame shape and thermoacoustic oscillation dynamics', *Fuel* **254**, 115524.

Keating, A., Piomelli, U., Balaras, E. & Kaltenbach, H.-J. (2004), 'A prioriand a posterioritests of inflow conditions for large-eddy simulation', *Physics of Fluids* **16**(12), 4696–4712.

Kedia, K. S., Altay, H. M. & Ghoniem, A. F. (2011), 'Impact of flame-wall interaction on premixed flame dynamics and transfer function characteristics', *Proceedings of the Combustion Institute* **33**, 1113–1120.

Kempf, A., Forkel, H., Chen, J. Y., Sadiki, A. & Janicka, J. (2000), 'Large-eddy simulation of a counterflow configuration with and without combustion', *Proceedings of the Combustion Institute* **28**(1), 35–40.

Kempf, A. M. (2007), 'LES Validation from Experiments', *Flow Turbulence Combust* **80**(3), 351–373.

Kim, K. T., Lee, J. G., Quay, B. D. & Santavicca, D. A. (2010), 'Response of partially premixed flames to acoustic velocity and equivalence ratio perturbations', *Combustion and Flame* **157**, 1731–1744.

Klein, M., Sadiki, A. & Janicka, J. (2003), 'A digital filter based generation of inflow data for spatially developing direct numerical or large eddy simulations', *Journal of Computational Physics* **186**(2), 652–665.

Kloeden, P. E. & Platen, E. (1992), *Numerical Solution of Stochastic Differential Equations*, Springer Berlin Heidelberg.

Komarek, T. & Polifke, W. (2010), 'Impact of Swirl Fluctuations on the Flame Response of a Perfectly Premixed Swirl Burner', *Journal of Engineering for Gas Turbines and Power* **132**.

Korusoy, E. & Whitelaw, J. H. (2001), 'Opposed jets with small separations and their implications for the extinction of opposed flames', *Experiments in Fluids* **31**(1), 111–117.

Korusoy, E. & Whitelaw, J. H. (2002), 'Extinction and relight in opposed flames', *Experiments in Fluids* **33**(1), 75–89.

Kostiuk, L. W., Bray, K. N. C. & Cheng, R. K. (1993*a*), 'Experimental study of premixed turbulent combustion in opposed streams. Part II?Reacting flow field and extinction', *Combustion and Flame* **92**(4), 396–409.

Kostiuk, L. W., Bray, K. N. C. & Cheng, R. K. (1993*b*), 'Experimental study of premixed turbulent combustion in opposed streams. Part I—Nonreacting flow field', *Combustion and Flame* **92**(4), 377–395.

Kostiuk, L. W., Bray, K. N. C. & Chew, T. C. (1989), 'Premixed Turbulent Combustion In Counterflowing Streams', *Combustion Science and Technology* **64**(4-6), 233–241.

Kraus, C., Selle, L. & Poinsot, T. (2018), 'Coupling heat transfer and large eddy simulation for combustion instability prediction in a swirl burner', *Combustion and Flame* **191**, 239–251.

Kuo, K. K. (2005), *Principles of Combustion*, Wiley.

Kushwaha, A., Kasthuri, P., Pawar, S. A., Sujith, R. I., Chterev, I. & Boxx, I. (2021), 'Dynamical characterization of thermoacoustic oscillations in a hydrogen-enriched partially premixed swirl-stabilized methane/air combustor', *Journal of Engineering for Gas Turbines and Power* **143**.

Larsson, J. & Kawai, D. S. (2010), 'Wall-modeling in large eddy simulation: length scales, grid resolution and accuracy'.

Leyko, M., Moreau, S., Nicoud, F. & Poinsot, T. (2011), 'Numerical and analytical modelling of entropy noise in a supersonic nozzle with a shock', *Journal of Sound and Vibration* **330**(16), 3944–3958.

Liang, H. & Maxworthy, T. (2005), 'An experimental investigation of swirling jets', *Journal of Fluid Mechanics* **525**, 115–159.

Libby, P. A. & Williams, F. A. (1994), *Turbulent Reacting Flows*, Academic Press.

Lieuwen, T. C. & Yang, V. (2006), *Combustion Instabilities In Gas Turbine Engines*, American Institute of Aeronautics and Astronautics.

Lieuwen, T., McDonell, V., Petersen, E. & Santavicca, D. (2008), 'Fuel Flexibility Influences on Premixed Combustor Blowout, Flashback, Autoignition, and Stability', *J. Eng. Gas Turbines Power* **130**(1), 141–10.

Lieuwen, T. & Zinn, B. T. (1998), 'The role of equivalence ratio oscillations in driving combustion instabilities in low nox gas turbines', *Symposium (International) on Combustion* **27**, 1809–1816.

Lindstedt, R., Luff, D. & Whitelaw, J. (2005), 'Velocity and Strain-Rate Characteristics of Opposed Isothermal Flows', *Flow Turbulence Combust* **74**, 169–194.

Lodato, G., Domingo, P. & Vervisch, L. (2008), 'Three-dimensional boundary conditions for direct and large-eddy simulation of compressible viscous flows', *Journal of Computational Physics* **227**(10), 5105–5143.

Lourier, J. M., Stöhr, M., Noll, B., Werner, S. & Fiolitakis, A. (2017), 'Scale Adaptive Simulation of a thermoacoustic instability in a partially premixed lean swirl combustor', *Combustion and Flame* **183**, 343–357.

Lu, T. & Law, C. K. (2008), 'A criterion based on computational singular perturbation for the identification of quasi steady state species: A reduced mechanism for methane oxidation with NO chemistry', *Combustion and Flame* **154**, 761–774.

Lucca-Negro, O. & O'Doherty, T. (2001), 'Vortex breakdown: A review', *Progress in Energy and Combustion Science* **27**.

Lund, T. S., Wu, X. & Squires, K. D. (1998), 'Generation of turbulent inflow data for spatially-developing boundary layer simulations', *Journal of Computational Physics* **140**, 233–258.

Magri, L. (2017), 'On indirect noise in multicomponent nozzle flows', *Journal of Fluid Mechanics* **828**, R2.

Magri, L., O'Brien, J. & Ihme, M. (2016), 'Compositional inhomogeneities as a source of indirect combustion noise', *Journal of Fluid Mechanics* **799**, R4.

Mansouri, Z., Aouissi, M. & Boushaki, T. (2016), 'Detached eddy simulation of high turbulent swirling reacting flow in a premixed model burner', *Combustion Science and Technology* **188**, 1777–1798.

Marble, F. & Candel, S. (1977), 'Acoustic disturbance from gas non-uniformities convected through a nozzle', *Journal of Sound and Vibration* **55**(2), 225–243.

Mastorakos, E., Taylor, A. M. K. P. & Whitelaw, J. H. (1992*a*), 'Extinction and temperature characteristics of turbulent counterflow diffusion flames with partial premixing', *Combustion and Flame* **91**(1), 40–54.

Mastorakos, E., Taylor, A. M. K. P. & Whitelaw, J. H. (1992*b*), 'Scalar dissipation rate at the extinction of turbulent counterflow nonpremixed flames', *Combustion and Flame* **91**(1), 55–64.

Meier, W., Weigand, P., Duan, X. & Giezendannerthoben, R. (2007), 'Detailed characterization of the dynamics of thermoacoustic pulsations in a lean premixed swirl flame', *Combustion and Flame* **150**, 2–26.

Moeck, J. P., Bourgouin, J.-F., Durox, D., Schuller, T. & Candel, S. (2012), 'Nonlinear interaction between a precessing vortex core and acoustic oscillations in a turbulent swirling flame', *Combustion and Flame* **159**, 2650–2668.

Moreau, S., Becerril, C. & Gicquel, L. (2017), 'Large-Eddy-simulation prediction of indirect combustion noise in the entropy wave generator experiment', *International Journal of Spray and Combustion Dynamics* **10**(2), 154–168.

Morgans, A. S. & Duran, I. (2016), 'Entropy noise: A review of theory, progress and challenges', *International Journal of Spray and Combustion Dynamics* **8**(4), 285–298.

Morgans, A. S., Goh, C. S. & Dahan, J. A. (2013), 'The dissipation and shear dispersion of entropy waves in combustor thermoacoustics', *Journal of Fluid Mechanics* **733**, R2.

Mustata, R., Valiño, L., Jiménez, C., Jones, W. P. & Bondi, S. (2006), 'A probability density function eulerian monte carlo field method for large eddy simulations: Application to a turbulent piloted methane/air diffusion flame (sandia d)', *Combustion and Flame* **145**, 88–104.

Navarro-Martinez, S. & Kronenburg, A. (2011), 'Flame stabilization mechanisms in lifted flames', *Flow, Turbulence and Combustion* **87**, 377–406.

Noh, D., Gallot-Lavallee, S., Jones, W. & Navarro-Martinez, S. (2018), 'Comparison of droplet evaporation models for a turbulent, non-swirling jet flame with a polydisperse droplet distribution', *Combustion and Flame* **194**, 135–151.

Noh, D., Karlis, E., Navarro-Martinez, S., Hardalupas, Y., Taylor, A. M. K. P., Fredrich, D. & Jones, W. P. (2019), 'Azimuthally-driven subharmonic thermoacoustic instabilities in a swirl-stabilised combustor', *Proceedings of the Combustion Institute* **37**(4), 5333–5341.

Noiray, N., Durox, D., Schuller, T. & Candel, S. (2008), 'A unified framework for nonlinear combustion instability analysis based on the flame describing function', *Journal of Fluid Mechanics* **615**, 139–167.

Oberleithner, K., Sieber, M., Nayeri, C. N., Paschereit, C. O., Petz, C., Hege, H.-C., Noack, B. R. & Wygnanski, I. (2011), 'Three-dimensional coherent structures in a swirling jet undergoing vortex breakdown: stability analysis and empirical mode construction', *Journal of Fluid Mechanics* **679**, 383–414.

Oberleithner, K., Stöhr, M., Im, S. H., Arndt, C. M. & Steinberg, A. M. (2015), 'Formation and flame-induced suppression of the precessing vortex core in a swirl combustor: Experiments and linear stability analysis', *Combustion and Flame* **162**, 3100–3114.

Palies, P., Durox, D., Schuller, T. & Candel, S. (2010), 'The combined dynamics of swirler and turbulent premixed swirling flames', *Combustion and Flame* **157**, 1698–1717.

Palies, P., Schuller, T., Durox, D., Gicquel, L. Y. M. & Candel, S. (2011), 'Acoustically perturbed turbulent premixed swirling flames', *Physics of Fluids* **23**, 037101.

Pettit, M. W. A., Coriton, B., Gomez, A. & Kempf, A. M. (2011), 'Large-Eddy Simulation and experiments on non-premixed highly turbulent opposed jet flows', *Proceedings of the Combustion Institute* **33**(1), 1391–1399.

Piomelli, U. & Liu, J. (1995*a*), 'Large-eddy simulation of rotating channel flows using a localized dynamic model', *Physics of Fluids* **7**, 839–848.

Piomelli, U. & Liu, J. (1995*b*), 'Large-eddy simulation of rotating channel flows using a localized dynamic model', *Physics of Fluids* **7**, 839–848.

Pitsch, H. (2006), 'Large-eddy Simulation of Turbulent Combustion', *Annual Review of Fluid Mechanics* **38**.

Poinsot, T. (2017), 'Prediction and control of combustion instabilities in real engines', *Proceedings of the Combustion Institute* **36**(1), 1–28.

Poinsot, T., Candel, S. & Trouvé, A. (1995), 'Applications of direct numerical simulation to premixed turbulent combustion', *Progress in Energy and Combustion Science* **21**, 531–576.

Poinsot, T. & Lele, S. (1992), 'Boundary conditions for direct simulations of compressible viscous flows', *Journal of Computational Physics* **101**.

Poinsot, T. & Veynante, D. (2005), 'Theoretical and Numerical Combustion', *Prog. Energy Combust. Sci.* **28**.

Pope, S. B. (1981), 'A Monte Carlo Method for the PDF Equations of Turbulent Reactive Flow', *Combustion Science and Technology* **25**.

Pope, S. B. (2000), *Turbulent Flows*, Cambridge University Press.

Raman, V., Pitsch, H. & Fox, R. (2005), 'Hybrid large-eddy simulation/Lagrangian filtered-density-function approach for simulating turbulent combustion', *Combustion and Flame* **143**.

Rayleigh (1878), 'The explanation of certain acoustical phenomena 1', *Nature* **18**, 319–321.

Ren, J. Y., Egolfopoulos, F. N. & Tsotsis, T. T. (2002), 'No x emission control of lean methane-air combustion with addition of methane reforming products', *Combustion Science and Technology* **174**, 181–205.

Ren, J.-Y., Qin, W., Egolfopoulos, F. & Tsotsis, T. (2001), 'Strain-rate effects on hydrogen-enhanced lean premixed combustion', *Combustion and Flame* **124**, 717–720.

Rhie, C. M. & Chow, W. L. (1983), 'Numerical study of the turbulent flow past an airfoil with trailing edge separation', *AIAA Journal* **21**, 1525–1532.

Rodrigues, J., Busseti, A. & Hochgreb, S. (2020), 'Numerical investigation on the generation, mixing and convection of entropic and compositional waves in a flow duct', *Journal of Sound and Vibration* **472**, 115155.

Rolland, E. O., de Domenico, F. & Hochgreb, S. (2017), 'Theory and application of reverberated direct and indirect noise', *Journal of Fluid Mechanics* **819**, 435–464.

Rolland, E. O., De Domenico, F. & Hochgreb, S. (2018), 'Direct and Indirect Noise Generated by Entropic and Compositional Inhomogeneities', *J. Eng. Gas Turbines Power* **140**(8).

Roux, S., Lartigue, G., Poinsot, T., Meier, U. & Bérat, C. (2005), 'Studies of mean and unsteady flow in a swirled combustor using experiments, acoustic analysis, and large eddy simulations', *Combustion and Flame* **141**, 40–54.

Rudy, D. H. & Strikwerda, J. C. (1980), 'A nonreflecting outflow boundary condition for subsonic navier-stokes calculations', *Journal of Computational Physics* **36**, 55–70.

Sabel'nikov, V. & Soulard, O. (2005), 'Rapidly decorrelating velocity-field model as a tool for solving one-point Fokker-Planck equations for probability density functions of turbulent reactive scalars', *Physical Review E* **72**, 016301.

Safta, C. & Madnia, C. (2006), 'Autoignition and structure of nonpremixed ch4/h2 flames: Detailed and reduced kinetic models', *Combustion and Flame* **144**, 64–73.

Sagaut, P. (2001), 'Large Eddy Simulation for Incompressible Flows. An Introduction', *Measurement Science and Technology* **12**, 1745–1746.

Sardi, K., Taylor, A. M. K. P. & Whitelaw, J. H. (1999), 'Extinction of Turbulent Counterflow Flames under Periodic Strain', *Combustion and Flame* **120**, 265–284.

Sarli, V. D. & Benedetto, A. D. (2007), 'Laminar burning velocity of hydrogen–methane/air premixed flames', *International Journal of Hydrogen Energy* **32**, 637–646.

Schmidt, H. & Schumann, U. (1989), 'Coherent structure of the convective boundary layer derived from large-eddy simulations', *Journal of Fluid Mechanics* **200**.

Schuermans, B., Guethe, F., Pennell, D., Guyot, D. & Paschereit, C. O. (2010), 'Thermoacoustic Modeling of a Gas Turbine Using Transfer Functions Measured Under Full Engine Pressure', *Journal of Engineering for Gas Turbines and Power* **132**.

Schumann, U. (1975), 'Subgrid scale model for finite difference simulations of turbulent flows in plane channels and annuli', *Journal of Computational Physics* **18**, 376–404.

Shanbhogue, S. J., Sanusi, Y. S., Taamallah, S., Habib, M. A., Mokheimer, E. M. A. & Ghoniem, A. F. (2016), 'Flame macrostructures, combustion instability and extinction strain scaling in swirl-stabilized premixed CH4/H2 combustion', *Combustion and Flame* **163**(C), 494–507.

Smagorinsky, J. (1963), 'General circulation experiments with the primitive equations', *Monthly Weather Review* **91**.

Sripakagorn, P., Mitarai, S., Kosály, G. & Pitsch, H. (2004), 'Extinction and reignition in a diffusion flame: a direct numerical simulation study', *Journal of Fluid Mechanics* **518**, 231–259.

Steinberg, A., Boxx, I., Arndt, C., Frank, J. & Meier, W. (2011), 'Experimental study of flame-hole reignition mechanisms in a turbulent non-premixed jet flame using sustained multi-khz piv and crossed-plane oh plif', *Proceedings of the Combustion Institute* **33**, 1663–1672.

Stöhr, M., Arndt, C. M. & Meier, W. (2015), 'Transient effects of fuel–air mixing in a partially-premixed turbulent swirl flame', *Proceedings of the Combustion Institute* **35**, 3327–3335.

Stöhr, M., Boxx, I., Carter, C. D. & Meier, W. (2012), 'Experimental study of vortex-flame interaction in a gas turbine model combustor', *Combustion and Flame* **159**, 2636–2649.

Stöhr, M., Oberleithner, K., Sieber, M., Yin, Z. & Meier, W. (2018), 'Experimental Study of Transient Mechanisms of Bistable Flame Shape Transitions in a Swirl Combustor', *Journal of Engineering for Gas Turbines and Power* **140**.

Stöhr, M., Sadanandan, R. & Meier, W. (2011), 'Phase-resolved characterization of vortex–flame interaction in a turbulent swirl flame', *Experiments in Fluids* **51**, 1153–1167.

Stöhr, M., Yin, Z. & Meier, W. (2017), 'Interaction between velocity fluctuations and equivalence ratio fluctuations during thermoacoustic oscillations in a partially premixed swirl combustor', *Proceedings of the Combustion Institute* **36**, 3907–3915.

Sung, C. J., Law, C. K. & Chen, J. Y. (2001), 'Augmented reduced mechanisms for NO emission in methane oxidation', *Combustion and Flame* **125**(1-2), 906–919.

Swaminathan, N. & Bray, K. N. C. (2011), *Turbulent Premixed Flames*, Cambridge University Press.

Syred, N. (2006), 'A review of oscillation mechanisms and the role of the precessing vortex core (PVC) in swirl combustion systems', *Progress in Energy and Combustion Science* **32**, 93–161.

Taamallah, S., LaBry, Z. A., Shanbhogue, S. J. & Ghoniem, A. F. (2015), 'Thermo-acoustic instabilities in lean premixed swirl-stabilized combustion and their link to acoustically coupled and decoupled flame macrostructures', *Proceedings of the Combustion Institute* **35**(3), 3273–3282.

Taamallah, S., Vogiatzaki, K., Alzahrani, F., Mokheimer, E., Habib, M. & Ghoniem, A. (2015), 'Fuel flexibility, stability and emissions in premixed hydrogen-rich gas turbine combustion: Technology, fundamentals, and numerical simulations', *Applied Energy* **154**, 1020–1047.

Tabor, G. R. & Baba-Ahmadi, M. H. (2010), 'Inlet conditions for large eddy simulation: A review', *Computers and Fluids* **39**, 553–567.

Tachibana, S., Saito, K., Yamamoto, T., Makida, M., Kitano, T. & Kurose, R. (2015), 'Experimental and numerical investigation of thermo-acoustic instability in a liquid-fuel aero-engine combustor at elevated pressure: Validity of large-eddy simulation of spray combustion', *Combustion and Flame* **162**, 2621–2637.

Temme, J. E., Allison, P. M. & Driscoll, J. F. (2014), 'Combustion instability of a lean premixed prevaporized gas turbine combustor studied using phase-averaged PIV', *Combustion and Flame* **161**, 958–970.

Terhaar, S., Oberleithner, K. & Paschereit, C. O. (2015), 'Key parameters governing the precessing vortex core in reacting flows: An experimental and analytical study', *Proceedings of the Combustion Institute* **35**, 3347–3354.

Thompson, K. W. (1987), 'Time dependent boundary conditions for hyperbolic systems', *Journal of Computational Physics* **68**, 1–24.

Tirunagari, R. & Pope, S. (2017), 'Characterization of extinction/reignition events in turbulent premixed counterflow flames using strain-rate analysis', *Proceedings of the Combustion Institute* **36**, 1919–1927.

Tirunagari, R. R., Pettit, M. W. A., Kempf, A. M. & Pope, S. B. (2016), 'A Simple Approach for Specifying Velocity Inflow Boundary Conditions in Simulations of Turbulent Opposed-Jet Flows', *Flow Turbulence Combust* **98**(1), 131–153.

Tirunagari, R. R. & Pope, S. B. (2016), 'An investigation of turbulent premixed counterflow flames using large-eddy simulations and probability density function methods', *Combustion and Flame* **166**, 229–242.

Valiño, L. (1998), 'A Field Monte Carlo formulation for calculating the probability density function of a single scalar in a turbulent flow.', *Flow, Turbulence and Combustion* **60**, 157–172.

Vanierschot, M., Müller, J. S., Sieber, M., Percin, M., van Oudheusden, B. W. & Oberleithner, K. (2020), 'Single- and double-helix vortex breakdown as two dominant global modes in turbulent swirling jet flow', *Journal of Fluid Mechanics* **883**, A31.

Vasilyev, O. V. & Lund, T. S. (1997), A general theory of discrete filtering for LES in complex geometries, Technical report, Annual Research Briefs of Centre for Turbulence Research, Stanford.

Versteeg, H. & Malalasekera, W. (2007), *An Introduction to Computational Fluid Dynamics: The Finite Volume Method*, Pearson Education Limited.

Veynante, D. & Vervisch, L. (2002), 'Turbulent combustion modeling', *Progress in Energy and Combustion Science* **28**, 193–266.

Vignat, G., Durox, D., Renaud, A., Lancien, T., Vicquelin, R. & Candel, S. (2021), 'Investigation of transient pvc dynamics in a strongly swirled spray flame using high speed planar laser imaging of sno2 microparticles', *Combustion and Flame* **225**, 305–319.

Vigueras-Zuñiga, M., Valera-Medina, A. & Syred, N. (2012), 'Studies of the Precessing Vortex Core in Swirling Flows', *Journal of Applied Research and Technology* **10**.

Wang, S., Bell, J. R., Burton, D., Herbst, A. H., Sheridan, J. & Thompson, M. C. (2017), 'The performance of different turbulence models (urans, sas and des) for predicting high-speed train slipstream', *Journal of Wind Engineering and Industrial Aerodynamics* **165**, 46–57.

Wang, S., Hsieh, S.-Y. & Yang, V. (2005), 'Unsteady flow evolution in swirl injector with radial entry. I. Stationary conditions', *Physics of Fluids* **17**, 045106.

Xia, Y., Laera, D., Jones, W. P. & Morgans, A. S. (2019), 'Numerical prediction of the Flame Describing Function and thermoacoustic limit cycle for a pressurised gas turbine combustor', *Combustion Science and Technology* **191**, 979–1002.

Yin, Z., Nau, P. & Meier, W. (2017), 'Responses of combustor surface temperature to flame shape transitions in a turbulent bi-stable swirl flame', *Experimental Thermal and Fluid Science* **82**, 50–57.

Yin, Z. & Stöhr, M. (2020), 'Time–frequency localisation of intermittent dynamics in a bistable turbulent swirl flame', *Journal of Fluid Mechanics* **882**, A30.

Yoo, C. S. & Im, H. G. (2007), 'Characteristic boundary conditions for simulations of compressible reacting flows with multi-dimensional, viscous and reaction effects', *Combustion Theory and Modelling* **11**, 259–286.

Yoo, C. S., Wang, Y., Trouvé, A. & Im, H. G. (2005), 'Characteristic boundary conditions for direct simulations of turbulent counterflow flames', *Combustion Theory and Modelling* **9**(4), 617–646.

Zhang, Y. & Vanierschot, M. (2021), 'Determination of single and double helical structures in a swirling jet by spectral proper orthogonal decomposition', *Physics of Fluids* **33**, 015115.